Theoretical Investigation of Luminescent Defects in Diamond

Moloud Kaviani Baghbadorani

Department of Physics

University of Bremen

February 2015

Theoretical Investigation of Luminescent Defects in Diamond

Moloud Kaviani Baghbadorani

Department of Physics

University of Bremen

February 2015

1. Reviewer: Prof. Dr. Thomas Frauenheim

2. Reviewer: Prof. Dr. Lucio Colombi Ciacchi

Day of the defense: 03.02.2015

Signature from head of PhD committee:

Abstract

The nitrogen-vacancy (NV) color center in diamond has attracted a lot of attention during the past few years. The magnetic state of a single defect can be manipulated optically which provides a possibility to use it as a quantum bit (qubit) in an optically coupled quantum register for scalable quantum information processing. It can also be used as a sensor in magnetometry on the nanoscale. Its strong room temperature luminescence can be utilized in single photon emitters for quantum cryptography, and for optical labeling in biomedical imaging. All applications critically rely on thermodynamically and optically stable defects, introduced in sufficient concentration and suitable charge state. To clarify the conditions for that, I have performed theoretical calculations in this thesis, for bulk crystals, slabs and nanoclusters of diamond.

Nanodiamonds (NDs) are particularly interesting for biomedical applications,therefore, they must be produced as small as possible to be comparable with the biomolecules. The question arises, how small NDs can be to preserve the ideal diamond environment for NV centers. To answer this question, I have performed quantum molecular dynamics (MD) simulation of the annealing of NDs, with sizes up to 450 atoms (d$\sim$1.3 nm) and with different shapes, in vacuum and in the presence of oxygen. For that purpose I have employed the efficient DFTB method. I have found that in clusters of over $\sim$250 atoms with cubic or cuboctahedral shape (i.e. with predominantly 100 faces), the ideal diamond structure of the core remains preserved even after long term annealing. The primary role of oxygen is the saturation of surface carbon atoms and the etching of the graphitic part. My results [1] show that if 100-faceted nanodiamonds as small as 1 nm in diameter are formed during synthesis, they will be kinetically stable up to high temperatures, although the thermodynamic stability

limit was estimated to be 1.9 nm. These results strengthen the position of ultra small nanodiamonds in biological and medical applications.

For practical applications the concentration of NV centers in the negative charge state should be increased but experimental attempts so far have produced only limited success. Therefore, I have investigated the formation mechanism of the NV(-) center theoretically. For that purpose I have calculated the formation energies of all defects (NV, NVH, N_2, N_2V, and V_2) which are expected to play a role in the formation of NV(-) in bulk diamond. For that purpose, I have used a highly accurate screened hybrid functional (HSE06). The results have allowed to reproduce experimentally observed internal excitation and known charge transition levels, and the prediction of missing ones. I have also calculated successfully the activation energy for V and NV diffusion. Based on the calculated properties of these defects, I have investigated different scenarios for the formation of the negatively charged NV center. My results indicate that NV defects are predominantly created directly by irradiation of moderately N-doped diamond, while vacancies will form divacancies (V_2) pairs during post-irradiation annealing. Divacancies, however, pin the Fermi level, making the NV defects neutral. I predicted [2] therefore, that the concentration of NV(-) centers can be enhanced by increasing the irradiation flux and by using higher annealing temperatures, to annihilate divacancies. This prediction has been very quickly confirmed experimentally by one of the leading groups in the field (PRB 90, 081117, 2014).

Most applications require NV(-) centers very close to the surface, which can affect the luminescence of the center, leading to undesired blinking effects of even bleaching. This also happens in nanodiamonds, where band-bending effects cannot be invoked for explanation. Therefore, I have investigated the interaction of surface states in variously terminated diamond slabs with the NV(-) center. I have determined equilibrium structures by standard DFT methods and calculated the electronic structure with the HSE06 hybrid functional. I have shown that typical H- and OH-terminated diamond surfaces possess image states in the band gap due to their negative elec-

tron affinity. These deep, empty states compromise the photostability of the NV(-) centers placed within a few nm of the surface, because they to mix with NV-related empty gap states and leading to the emission of the excited electron (bleaching). I have also shown that strongly oxidized surfaces with positive electron affinity can also have acceptor type surface states near the conduction band. In case of high intensity (multi-photon) excitation), these states can shelve the excited electrons, leading to blinking of the luminescence. Based on my results, I have identified a combination of surface terminators with no effect on the luminescence of NV(-) [3]. Such a termination can be realized by mild oxidation of hydrogenated surfaces or by oxidation with acids.

Luminescent nitrogen-vacancy (NV) centers in nanodiamonds (ND) have great potential for biolabeling. Theoretical estimates for the likelihood of producing such centers in very small NDs rely on the diffusion activation energy (DAE) of the neutral vacancy, in comparing the rate of vacancy-capture by a substitutional N with out-diffusion. The DAE is influenced by two effects in nano-sized systems: quantum confinement increases it, while the increasing relaxation freedom, due to the closeness of the surface, decreases it. Therefore, we have investigated the effect of size on the DAE of vacancy motion in diamond by ab initio DFT calculations, and found that, on the whole, it decreases with size. This reinforces earlier theoretical predictions that NDs below 5 nm in diameter are not likely to contain NV centers at all. The fact that this prediction contradicts experiments, lends support to our earlier finding [PRB 89, 075203 (2014)] that vacancy diffusion does not play a significant role in the formation of NV centers, which must be created instead directly (by removing a carbon atom next to an N substitutional) during irradiation of N-doped diamond [4].

Acknowledgements

First of all, I would like to thank Professor Thomas Frauenheim for providing an excellent opportunity for me to study at the BCCMS as a Ph.D. student. I am also grateful for his support during the past three years.

I also would like to express all my gratitudes to my supervisor Professor Peter Deák, head of the Electronic Materials Group at the BCCMS. I would like to thank him for all his efforts on teaching me all this time. Without his encouragement and guidance this thesis would not have been materialized.

I would also like to thank Christine Frauenheim for her support, Sandra Smit, Michaela Wessalowski and Meike Pfennig for their moral support and their friendships.

Finally, I want to express my gratitude to my dear parents, sister and brother for their support during these years.

There are several people who helped me during the time of my stay here that I will not mention everyone of them by name, but I would like to say that I am extremely grateful for all their energy and friendship. Your contribution is bigger than you think.

Contents

List of Figures

LIST OF FIGURES

List of Tables

Chapter 1

Introduction

Crystals are like people; it is only the defects that make them interesting.

Sir F. C. Frank

1.1 Motivation

Defects in crystals can strongly affect the properties of materials. This is especially important in semiconductors where even a small amount of impurities can cause a significant change in the electrical and optical properties of the material. Shallow dopants influence the electrical conductivity of the material turning an insulator into a n-type or p-type semiconductor [5, 6]. The conductivity can further be controlled by the presence of compensating centers in the form of native or impurity defects. These centers introduce deep levels in the gap which give rise to optical absorption and luminescence. In addition, the mechanical properties and the long-term stability of materials can largely be controlled by point and line defects [7, 8]. Understanding the physics and the chemistry of impurities has always been essential for further developments in micro- and opto-electronics.

For decades people have tried to achieve the best way for studying point defects in solid materials. Therefore, the existence of a huge amount of theoretical calculations on the point defects and their properties is not a surprise [10]. Among all methods, the first-principle calculations are such powerful approaches that can often complement experiments while they are reliable

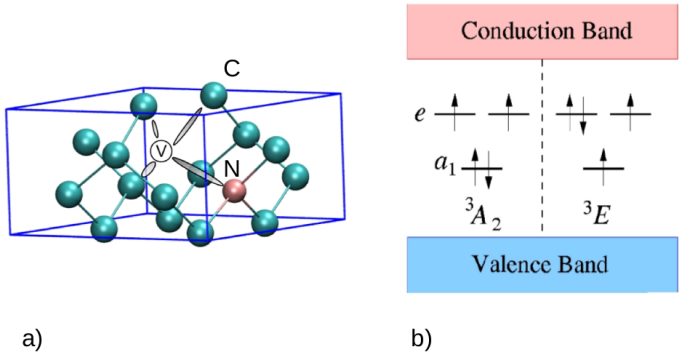

Figure 1.1: (a) Nitrogen-vacancy (NV) defect in diamond. (b) schematic diagram of the defect levels for the negatively charged NV defect; left panel: ground state, right panel: excited state [9]

enough to serve as a predictive tool for characterizing and identifying the defects. Among various *ab initio* techniques, density functional theory (DFT) has become widespread over the last two decades. In the present study, DFT has been used as the computational tool for studying various aspects of defects such as optical and electronic properties.

In the next two sections, the material and the defects for which some of their properties are going the be studied, are introduced. Their fabrication methods and their applications will be named.

1.2 Nitrogen-Vacancy center in diamond

Diamond is known for its excessive hardness and high thermal conductivity. Diamond is an electronic insulator with a wide bandgap of 5.48 eV [11] and is optically transparent in the visible regime. It can host a lot of different point defect centers, called color centers, that emit light. A particular defect which has acquired great importance lately is the NV (nitrogen-vacancy) center in diamond. In the NV-center a nitrogen atom substitutes a carbon atom next to a vacancy (see Fig. 1.1a) oriented along the (111) crystalline direction. The NV-centre can be found as an "in grown" product of the chemical vapour deposition (CVD) in diamond synthesis process [12] or as a product of radiation damage with energetic neutrons, electrons, or ions [13, 14] and annealing [15] or ion implantation and annealing [16] in bulk and nanocrystalline diamond [17].

NV-centers have been observed in two charge states, the neutral (NV(0)) [18] and the negatively charged (NV(-)) [19] states. These charge states are known from spectroscopic studies using optical absorption [20, 21], electron paramagnetic resonance (EPR)[18, 22], photoluminescence (PL) [23] and optically detected magnetic resonance (ODMR) [24]. These charge states can be identified by their optical zero phonon lines (ZPLs) at 1.945 eV (637 nm) for the negatively charged state [25] and 2.156 eV (575 nm) for the neutral charged state [26], respectively, and associated vibronic bands that extend from their ZPLs to higher or lower energy in absorption or emission spectra (see Fig. 1.2).

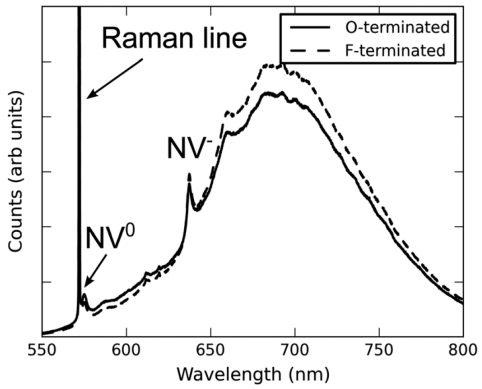

Figure 1.2: Photoluminescence of the NV center at room temperature. NV(0) and NV(-) zero-phonon lines (ZPL) are at 575 and 637 nm, correspondingly [27].

This defect has attracted a lot of attention during past few years. NV-center in bulk diamond is capable of realizing quantum bits at room temperature [24, 28–34] and detect magnetic [35–38] and electric fields [38], temperature [39–41] or chemical changes on the surface [42] at the nanoscale. The NV-center has been exhibited to possess the highly desirable properties of single-photon generation [28, 43] and long-lived coherence [44]. It has been demonstrated that the NV center can be produced in small diamond nanoparticles (nanodiamonds) [15, 45–53]. This opens up the way to use fluorescent nanodiamonds for biolabeling and other biomedical applications [54–59].

All of these applications require the synthesis of thermodynamically and optically stable defects in suitable concentration in the appropriate charge state [2]. In fact, most of the applications rely on the negatively charged of the NV-center.

The electronic structure of this defect in its negatively charged state is illustrated in Fig. 1.1b. The spin state of this defect can be manipulated using excitation from the $^3A_2$ ground state to the ^3E excited state by optical absorption (see Fig. 1.1b) [9]. According to the theoretical calculations [60–63], the $^3A_2$ ground state with C_{3v} symmetry can be built from the single-particle band gap states, a fully occupied a_1 and a doubly degenerate e state occupied by two electrons of parallel spin. The excitation of this defect can be described by promoting one electron from the a_1 level to the e level, while in the luminescence process the excited electron from the e level goes back to the lower a_1 level (see Fig. 1.1b) [9].

Due to the potential applications of NV-centers in biolabeling, nano-sensing and quantum information technologies, this defect must be placed as close as possible to the surface. Therefore, in the next section we will introduce the nanodiamonds along with the state-of-the-art progresses of NV-centers in them.

1.3 Nanodiamonds

Nanodiamonds contain a crystalline core of a few nanometers in diameter, covered by graphitic layers. They were first produced by detonation in the USSR in the 1960s [64, 65]. According to the theoretical calculations the morphology of nanodiamonds plays an important role in their stability by influencing surface reconstruction and the formation of sp^2 carbon [66, 67]. Due to a large number of carbon atoms with dangling bonds on the surface and a large surface to volume ratio, nanodiamonds exhibit a very high surface reactivity. The crystals with the cube shape, with dominant (001) surfaces, exhibit structures similar to the bulk diamond, while surfaces of octahedral, cuboctahedral (contains of (111) surfaces) and spherical clusters show a transition from sp^3 to sp^2 in the surface of the crystal. According to the theoretical calculations [68] the graphitization energies for the (111) and (110) diamond surfaces are 0.003 and 0.24 eV/surface atom, respectively. The big difference between the graphitization energies demonstrate that graphitization of a (111) surface is preferred over that of the (110) and (100) surfaces [67, 68].

As mentioned before, the optical and magnetic properties of the NV center make it very attractive for biomarker applications because the host material, diamond, is considered bioinert. For using nanodiamonds in the biomarker applications one has to fabricate them as small as

possible, in order to be compatible with the size of typical biological molecules. This has been recently realized either by a milling process [15] or by a detonation method [69, 70]. It is important to note that detonation NDs were cleaned using strong oxidizing acids [51, 53, 71, 72] which remove the graphitic shells and produce more "active" fluorescent NV centers [53, 73]. Furthermore, according to an *ab initio* study, for nanodiamonds larger than 3 nm in diameter (d), surface reconstructed nanodiamonds are favorable over hydrogenated nanocrystallites even in the presence of hydrogen [74, 75].

Surface reconstruction will minimize the surface energy and reduce the number of dangling bonds of the carbon atoms on the surface. The carbon atoms on the unreconstructed surface have two dangling bonds. This surface can go through a 2×1 reconstruction after relaxation (see Fig. 1.3a) where neighboring atoms on the surface form π-bonded dimers. In the case of hydrogenated surface, π-bond between the dimers is replaced by a covalent bond to the hydrogen (see Fig. 1.3b) [76]. The hydroxyl groups also relax to a (100):2×1 reconstruction (see Fig. 1.3c) [77–79]. With terminating the surface, all of the surface carbon atoms get sp^3-bonded structure but sometimes some of these sp^3 bonds break under annealing and graphitization may occur. Studies have shown that the surface is stable around 1800°C in vacuum and around 800°C in presence of oxygen [80]. Above these temperatures surface goes through graphitization.

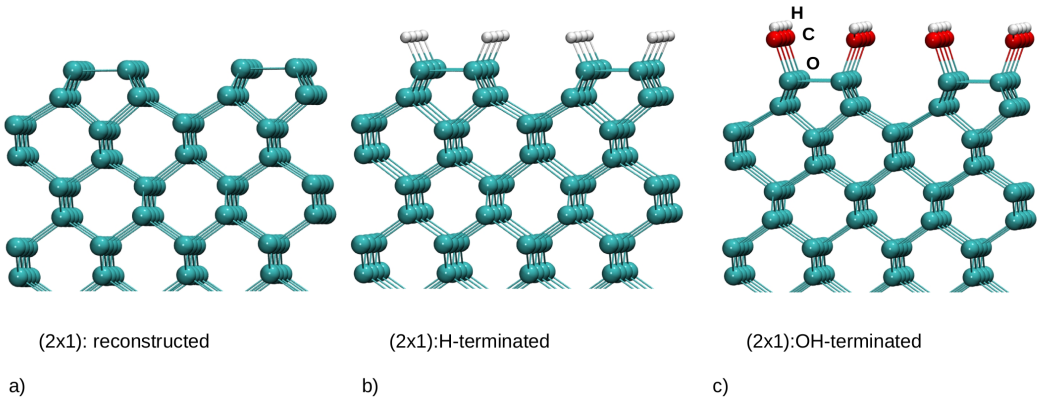

Figure 1.3: Optimized atomic geometries for the a) clean, b) hydrogenated, c) hydroxylated (001):2×1 reconstructed diamond surfaces.

Very recently it has been reported [53] that by careful chemical treatment of aggregated detonation nanodiamonds, one can realize isolated nanodiamonds with d<5 nm in colloid solution,

and the graphitic content of the samples are in dramatically reduced in this way. About 1% of such isolated nanodiamonds contained fluorescent NV centers [53]. It was also shown that the removal of the graphitic shell is paramount to reduce the surface state density, which acts as trap for donor electrons [81]. Even though the number of active NV(-) defects decreases with the size of the nanodiamonds, reports of even smaller (d$<$ 5 nm) active nanodiamonds keep appearing.

1.4 Structure of the thesis

The aim of this thesis is to investigate various structural and electronic properties of nanodiamonds and NV-centers. The formation mechanism of the NV-centers in the bulk diamond have been investigated. Further on, the interaction of this defect with different surface terminations in the slab diamonds is studied. The formation of the nanodiamonds and their thermal stability are also investigated. In addition, the effect of the size on the diffusion activation energy of different defects in the NDs is explored.

The objectives comprise investigations on:

1. How small nanodiamonds can be to survive heat treatment?
2. How can the concentration of negatively charged NV center be increased?
3. How does surface termination influence the photoluminescence of NV center?
4. How do nano-size defects affect the diffusion?

This thesis is formed in seven chapters. In chapter two, I present a brief overview of the computational methods used in this work. The main work has been done by applying the density functional theory (DFT) with GGA-PBE and HSE06 functionals for the exchange and correlation energies. These DFT related concepts are shortly discussed and at the end of this chapter a brief introduction on the density functional theory based tight-binding method (DFTB) is given.

The main results are presented in four subsequent chapters. In chapter three the task is to find an answer for the question : *How small nanodiamonds can be to survive heat treatment?* In

these calculations, it has been tried to make stable NDs as small as possible corresponding to realistic surfaces. The surface structures of the diamond-core carbon nanoparticles with different shapes and in different environments are investigated with the help of molecular dynamics (MD) simulations.

The size of the clusters and the time scale needed to perform MD calculations were beyond the reach of DFT, however, first-principle quality calculations to correctly model bond breaking and bond formation was needed. Therefore, we used the density functional theory based on tight binding (DFTB) method which provides accurate enough results in a very computationally efficient way. Our results strengthen the position of NDs for biological applications. These results have been published in Ref. [1].

In chapter four, the question of: *How can the concentration of negatively charged NV center be increased?* is answered. Advanced DFT calculations have been applied to determine the formation energies, the charge transition levels and the diffusion activation energies for N- and V-related defects in diamond. In this study we found that the concentration of NV in as-grown diamond is always smaller than that of substitutional nitrogen (N_s) due to the low equilibrium concentration of vacancies. The calculated reaction energies between N_s and vacancies indicate that the concentration of NV will not be higher even if a nonequilibrium excess of vacancies is provided. This is due to the preference for divacancies (V_2) over NV formation. However, formation of the NV can be expected to dominate over the formation of V during irradiation. We have also investigated the conditions for having negatively charged NV-centers which is important for practical applications. Some of these results have been published in Ref. [2].

In chapter five, different terminations for the two dimensional slab diamonds are considered. We tried to answer the question: *How does surface termination influence the photoluminescence of NV center?* Blinking or bleaching of NV-center photoluminescence have been observed in connection with various surface terminations. Our calculations can explain these blinking and bleaching phenomena in the terms of interactions between surface and defect states. These results have been published in Ref. [3].

In chapter six, the effect of size on the diffusion activation energy of neutral vacancy in the nanodiamonds is investigated. The calculations have been done by using *ab initio* DFT calculations. Activation energy can be influenced by two effects: First, the quantum confinement

effect and, second, the relaxation freedom due to the closeness of the surface. The quantum confinement will increase the barrier energy while the relaxation decreases it. Based on our calculations for the diffusion of vacancy we found that the vacancy diffusion does not play a significant role in the formation of NV-centers. This confirms the results we obtained in Ref. [2] which indicate the effect of irradiation on the formation of NV-centers.

Finally, in chapter seven, I summarize the results and outline few directions for future works in this field.

Chapter 2

Theoretical Background

2.1 The Hamiltonian of Solids

In material science all forms of matters are systems consisting of interacting electrons and nuclei. These systems are fully describable by wavefunctions which can be obtained by solving the Schrödinger equation

$$i\hbar\frac{d\Phi(\mathbf{r}_i;\mathbf{R}_n;t)}{dt} = \hat{H}\Phi(\mathbf{r}_i;\mathbf{R}_n;t), \tag{2.1}$$

where $\hat{H}$ is the Hamiltonian operator. The many-body wavefunctions depend on the coordinates of the electrons $\mathbf{r}_i$ and the nuclei $\mathbf{R}_n$ in the system. The Hamiltonian for such a system is:

$$\begin{aligned}\hat{H} = &-\hbar^2\sum_{i=1}^{I}\frac{\nabla_i^2}{2m_i} - \hbar^2\sum_{n=1}^{N}\frac{\nabla_n^2}{2M_n} - \sum_{i=1}^{I}\sum_{n=1}^{N}\frac{eZ_n}{|\mathbf{r}_i-\mathbf{R}_n|} \\ &+\sum_{i=1}^{I}\sum_{j>i}^{I}\frac{e^2}{|\mathbf{r}_i-\mathbf{r}_j|} + \sum_{n=1}^{N}\sum_{l>n}^{N}\frac{Z_nZ_l}{|\mathbf{R}_n-\mathbf{R}_l|}.\end{aligned} \tag{2.2}$$

In this equation, m_i and M_n are the masses of the i-th electron and n-th nucleus, respectively. Z_n is the charge of the nuclei. $\mathbf{r}$ and $\mathbf{R}$ are spatial coordinates of each electron and nucleus. The first two terms in the Hamiltonian are the kinetic energy of the electrons and nuclei. The last three terms are the Coulomb interactions between electron/nuclei, electron/electron and nuclei/nuclei.

Solving the Schrödinger equation even for small systems with few numbers of particles is computationally very demanding. One of the approximations which simplifies the problem is the *Born-Oppenheimer* approximation [82]. It is assumed that since the nuclei are much heavier than the electrons, their movement is much slower than the electrons, therefore, electrons adjust their equilibrium state instantly after nuclei spatial changes. This allows the Hamiltonian to be separated into parts for electrons and nuclei. Since in this approximation it is assumed that the nuclei are fixed then the kinetic energy part in the Hamiltonian can be removed and the potential term (the last part of equation 2.2) will be replaced by a constant.

The time-independent wavefunction can be written as:

$$\Psi(r_i; R_n) = \psi(r_i; R_n)\chi(R_n). \tag{2.3}$$

The total energy is:

$$\begin{aligned} E = &-\langle\chi\psi|\sum_{i=1}^{I}\frac{1}{2m_i}\nabla_i^2|\psi\chi\rangle - \langle\chi\psi|\sum_{i=1}^{I}\sum_{n=1}^{N}\frac{eZ_n}{|\mathbf{r}_i-\mathbf{R}_n|}|\psi\chi\rangle \\ &+\langle\chi\psi|\sum_{i=1}^{I}\sum_{j>i}^{I}\frac{e^2}{\mathbf{r}_i-\mathbf{r}_j}|\psi\chi\rangle + \langle\chi\psi|\sum_{n=1}^{N}\sum_{l>n}^{N}\frac{Z_nZ_l}{|\mathbf{R}_n-\mathbf{R}_l|}|\psi\chi\rangle. \end{aligned} \tag{2.4}$$

The two most common techniques to reduce the many-many electron problem are:

1. Hartree-Fock theory
2. Density functional theory (DFT)

In the Hartree-Fock method, the total energy is considered as a functional of the many-body wavefunction, constructed from independent single particle states as a Slater determinant. Single particle states comply with the Pauli principle but on the other hand they are not correlated. In the DFT method, instead of working with this wavefunction, the total energy is considered as a functional of electron density. This change of primary working quantity simplifies the computational problem to a great degree. The main reason is that while the many-body wavefunction is a functional of 3N variables (3 coordinates for N particles) the electron density just depends on the spatial coordinates. In the last two decades the density functional theory has been used

widely because of its high efficiency. In the following, I will briefly review Hartree-Fock and DFT methods.

2.2 Hartree-Fock (HF) Method

The fundamental quantity for the wavefunction based methods is the many-body wavefunction ψ. The first step in the determination of ψ is often a simple guess and then reliance on the variational principle. The variational priciple is a theorem used to systematically determine the ground state wavefunction and its energy. The expectation value of the electronic Hamiltonian for any trial wavefunction is always greater than or equal to the energy of the ground state ($E\psi \geq E_0\psi$). Starting from a guess wavefunction one can approach in to the ground state energy $E_0\psi_0$ by variationally improving the quality of the wavefunction. In the HF method, the exact many-body wavefunction of the system is approximated by a single Slater determinant of the single particle functions. The Slater determinant is a determinant of one particle orbitals which satisfy the antisymmetric property of the Pauli principle. For simplicity the spin of the electrons is omitted from the notation. Neglecting the spin of the electrons in the calculation does not imply any serious limitation on the end results. In fact, at the Hartree-Fock level it is a simple matter to include explicitly the spin degree of freedom by considering the electrons with spin up and down at the position $\mathbf{r}$

$$\psi = \frac{1}{N!}\begin{pmatrix} \psi_1(r_1) & \psi_1(r_2) & \cdots & \psi_1(r_N) \\ \psi_2(r_1) & \psi_2(r_2) & \cdots & \psi_2(r_N) \\ \vdots & \vdots & \ddots & \vdots \\ \psi_N(r_1) & \psi_N(r_2) & \cdots & \psi_N(r_N). \end{pmatrix} \tag{2.5}$$

where N is the total number of electrons.

The total energy is:

$$\begin{aligned} E^{HF} &= \langle \Psi^{HF} | H | \Psi^{HF} \rangle \\ &= \sum_i \langle \psi_i | \frac{-\hbar^2 \nabla_i^2}{2m_i} + V_{ion}(\mathbf{r}) | \psi_i \rangle \\ &+ \frac{e^2}{2} \sum_{ij(i \neq j)} \langle \psi_i \psi_j | \frac{1}{|\mathbf{r} - \mathbf{r}'|} | \psi_i \psi_j \rangle \\ &- \frac{e^2}{2} \sum_{ij(i \neq j)} \langle \psi_i \psi_j | \frac{1}{|\mathbf{r} - \mathbf{r}'|} | \psi_j \psi_i \rangle \end{aligned} \tag{2.6}$$

The single-particle Hartree-Fock equation:

$$[\frac{-\hbar^2 \nabla_i^2}{2m_i} + V_{ion}(\mathbf{r}) + V_i^C(\mathbf{r})]\psi_i(\mathbf{r}) - e^2 \sum_{i \neq j} \langle \psi_j | \frac{1}{|\mathbf{r} - \mathbf{r}'|} | \phi_i \rangle \psi_j(\mathbf{r}) = \epsilon_i \psi_i(\mathbf{r}) \tag{2.7}$$

The last term here is called "exchange" term which describes the effects of exchange between electrons (in the following X denotes the exchange part). Furthermore,

$$V_{ion} = -\sum_i \frac{Z_i e^2}{|R_i - r|} \tag{2.8}$$

is the total external potential experienced by an electron due to the presence of the ions and

$$V_i^C(\mathbf{r}) = e^2 \sum_{j \neq i} \langle \phi_j | \frac{1}{|\mathbf{r} - \mathbf{r}'|} | \phi_i \rangle \tag{2.9}$$

is the Coulomb part which describes the potential on one electron in the average charge distribution cased by the other electrons. Since this part only depends on the value of the wavefunction at the position of the i-th electron, it is said to be local.

The single particle Hartree-Fock equation is:

$$[\frac{-\hbar^2 \nabla_r^2}{2m_e} + V_{ion}(\mathbf{r}) + V_i^H(\mathbf{r}) + V_i^X(\mathbf{r})]\phi_i(\mathbf{r}) = \epsilon_i \phi_i(\mathbf{r}) \tag{2.10}$$

when

$$V_i^X(\mathbf{r}) = -e^2 \int \frac{n_i^X(\mathbf{r}, \mathbf{r}')}{|\mathbf{r} - \mathbf{r}'|} d\mathbf{r}'. \tag{2.11}$$

In this point it should be mentioned that in the Hartree-Fock approximation it is assumed that the electrons can move in an average field of the other electrons. This means that the

electrons can get too close to each other. Since this part inversely depends on the distances between the electrons, the electron/electron interaction will be overestimated. The outcome is a large ground state energy. Plus, using Hartree-Fock method in its exact exchange costs in the order of $\sim N^4$ (N is the number of particles) even without considering correlation corrections. Therefore, these calculations are highly time consuming.

Another commonly used scheme for handling the many electron problem is density functional theory (DFT).

2.3 Density Functional Theory (DFT)

The basic ideas of DFT are contained in the two original papers of Hohenberg, Kohn and Sham which are referred to as the Hohenberg-Kohn-Sham theorem [83, 84]. In this theory, instead of working with many-body Schrödinger equation which involves the many-body wavefunction $\Psi(r_i)$, one can deal with the total density of electrons n(r) instead. The electron density is defined as:

$$N(\mathbf{r}) = N \int \cdots \int \mid \Psi(x_1, x_2, \ldots, x_N) \mid^2 dx_1 dx_2 \ldots dx_N \tag{2.12}$$

where $\mathbf{x}_i$ represents both spacial and spin coordinates. In the above equation n(r) determines the probability of finding an electron within the volume $\mathbf{r}$. Here, the spin is arbitrary. The total number of electrons can be calculated by:

$$N = \int N(r) dr. \tag{2.13}$$

The formulation of DFT is based on the Hohenberg-Kohn theorems as described in the next section.

2.3.1 Hohenberg-Kohn Theorems

In 1964, Hohenberg and Kohn [83] first derived the fundamentals of DFT which allows to express electronic Hamiltonian as a functional of n(r). This formally relies on two key theorems:

- **Theorem 1:** *The external potential V_{ext} of a many-electron system can be uniquely determined except for a constant shift of the energy by the ground state particle electronic density $n_0(r)$. Thus, the ground state particle electronic density uniquely determines the whole properties of the system*[1].

- **Theorem 2:** *A universal functional for the energy $E[n]$ can be defined in the terms of density which minimizes the total energy. This density is the exact ground-state density.*

Therefore, the energy for the ground state density is lower than the energy for any other density. From now on the problem changes to obtain the total energy functional of the system; however, all the Hohenberg-Kohn formalism is based on unknown functionals. Defining these unknown functionals for the many interacting particle systems is very complicated. In 1975, Kohn and Sham reformulated the DFT problem and make a new approach which is called Kohn-Sham approach which is based on two assumptions:

1. The exact ground state density of an interacting system can be written as a ground state density of an auxiliary independent-particle system. Here, it is assumed that the two systems have exactly the same ground state density. In this theory the original interacting system with a real potential can be replaced by a non-interacting system in which electrons move within an effective Kohn-Sham single-particle potential V_{KS}.

2. The Hamiltonian for the auxiliary system have usual kinetic operator and an effective local potential called V_{KS} which acts individually on each electron in the system.

$$H_{KS} = \frac{1}{2}\nabla^2 + V_{KS} \tag{2.14}$$

in atomic unit $\hbar = m_e = e = \frac{4\pi}{\varepsilon_0} = 1$.

$$V_{KS} = V_{ext}[n(r)] + V_H[n(r)] + V_{XC}[n(r)] \tag{2.15}$$

[1]This theorem can be extended to formulate the time-dependent density functional theory (TD-DFT) [85, 86], which can describe the excited states.

where V_{ext} is the interaction between electrons and nucleus , V_{XC} is called the "Exchange-Correlation functional". V_H is the *Hartree* energy.

$$V_H = \frac{1}{2} \int \frac{n(r')}{|r - r'|} dr'. \tag{2.16}$$

The functional V_H gives the interaction energy of ρ with its own electrostatic field. This mean-field approximation makes the computational method easier but also causes a spurious self-interaction energy. The Hartree functional gives a non-vanishing repulsion energy even for a system with only one electron. In the Hartree-Fock theory this effect will be canceled automatically by the exchange integrals but this is not happening in the Kohn-Sham theory. In the Kohn-Sham method any correction must be unified with the XC functional. The exact form of the XC functional is still unknown.

2.4 Exchange-Correlation Functional

Since exchange-correlation energy which is a crucial ingredient in the DFT theory, is not available in an exact form, the practical calculations generally rely on approximations of this functional [87]. It is still an open and active research topic to improve existing functionals or find new ones to obtain better approximations. There are plenty of different approximations for E_{XC}. An interesting way for categorizing these methods has been introduced by Perdew, borrowing the term "Jacob's ladder"[88, 89]. Different rungs of this ladder represent different functional categories helping one climbing from *Hartree world* to the *chemical accuracy heaven*. Here, I will briefly discuss those of them which have been used in this thesis (see Fig. 2.1).

2.4.1 The Local Density Approximation (LDA)

The LDA functional is a very well known and used approximation for systems with delocalized electrons [90]. In this approach the E_{xc} is assumed to be the same as E_{xc} of a homogeneous electron gas with the same density. For systems where the particle density varies slowly, the system is divided by very small volumes and each of them has a constant electron density. In this case the exchange-correlation energy for each of these sub-systems is assumed to be

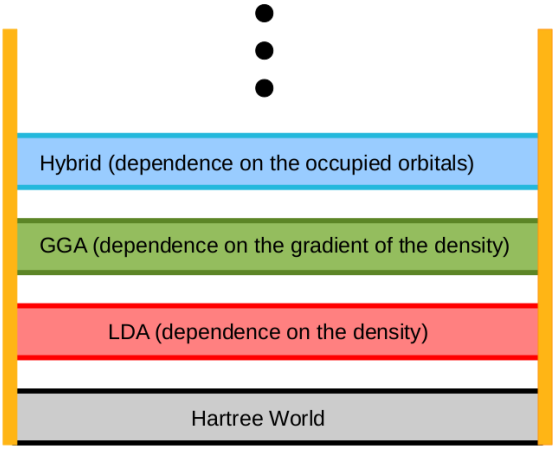

Figure 2.1: Jacob's ladder.

the exchange-correlation energy obtained from the uniform electron gas (UEG) for each of the densities. The total exchange-correlation energy of a spin-unpolarized system is:

$$E_{XC}^{LDA}[n] = \int n(r)\varepsilon_{XC}^{unif}(n(r))dr. \tag{2.17}$$

where ε_{XC}^{unif} is the exchange-correlation energy per particle of the interacting uniform electron gas with density n(r). For calculating the exchange-correlation energy the exchange and the correlation parts are calculated separately.

$$\varepsilon_{XC}^{unif} = \varepsilon_{X}^{unif} + \varepsilon_{C}^{unif} \tag{2.18}$$

The exchange energy for systems with inhomogeneous density is obtained by applying the UEG results pointwise

$$E_{X}^{LDA}[n] = -\frac{3}{4}(3\pi)^{1/3}\int n^{\frac{4}{3}}(r)dr. \tag{2.19}$$

The correlation part is complicated. It is generally obtained by fitting to the many-body results, as in the works of Gell-Mann and Brueckner and Ceperly and Alder [91, 92]. The LDA functionals which are used recently are getting much more simple. The difference between these functionals are only in how their correlation contributions have been fitted to the many-body free

electron gas data. The most common functionals are Perdew-Zunger (PZ) [93], Perdew-Wang (PW) [94] and Vosko-Wilk-Nusair (VWN) [95].

LDA functionals provide reasonable results for solids in many cases, however for atoms and molecules (inhomogeneous systems) the errors are often large. This has been the motivation for the development of the next generation of functionals which are described in the next section.

2.4.2 Generalized Gradient Approximation (GGA) Semi-local Functionals

In practice, most systems are spatially inhomogeneous. This means that the electron density, n(r), is varying spatially and considering this information in the functional would be very useful. The first try was inclusion of the gradient of the density to the LDA:

$$|\nabla n(r)|, |\nabla n(r)|^2, |\nabla^2 n(r)|, etc. \tag{2.20}$$

This class of approximation is called gradient-expansion approximation (GEA) [96]. This correction for the low-order gradient almost never improves the LDA and at some point even worsens it. Higher-orders such as $|\nabla(r)|^\alpha$ or ∇^βn(r) with $\alpha, \beta > 2$ are very difficult to calculate and little is known about them. Later, it was found that instead of power-series-like gradient expansions one could applies a more general functions of n(r) and $\nabla n(r)$.

$$E_{XC}^{GGA}[n] = \int n(r)\varepsilon_{XC}(n(r), \nabla n(r))d^3r \tag{2.21}$$

These functionals are the second generation functionals and are known as generalized-gradient approximation (GGAs) [97]. GGAs are often called "semi-local" functionals because of their dependence on $\nabla n(r)$. Compared to the LDA, GGAs obtain better results, *e.g.* more accurate ground state energies of molecules and solids. Specially for covalent systems the GGAs are getting much better results than LDA. Different GGA functionals differ in the choice of the f(n,∇n) function. Note that because of flexibility in the choice of the f(n,∇n) function, a wide variety of GGA functionals have been developed and depending on the system under study different results can be obtained. Nowadays, the most popular GGA functional is PBE [97] (proposed by Perdew, Burke and Ernzerhof in 1996) in physics and BLYP (combination of

Becke's 1988 exchange functional with the correlation functional of Lee, Yang and and Parr in 1988 [98]) in chemistry [99]. The GGAs generally give acceptable results for all main types of bonds such as covalent, ionic and metallic. For systems with van der Waals (vdW) interactions several more specialized approaches have been developed within DFT [100–103]).

2.4.3 Hybrid Functionals

DFT in the standard implementations (GGA and LDA) has some serious limitations. The most important one of them is probably incorrect calculations of the electronic structures of strongly correlated systems[104] and underestimation of the bandgaps (sometimes no gap).

In the case of defects, this deficiency has been considered a minor problem hampering only the comparison of the calculated spectra with the experimental data. But in fact it has serious implications for the formation energy [105] and for the relative stability of different defect configurations [11, 106, 107].

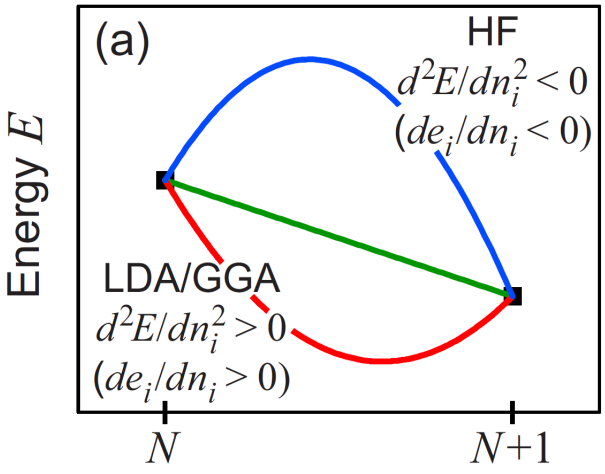

Figure 2.2: In HF theory (blue) the energy is a concave function of the continuous occupation number n_i, but a convex one in LDA or GGA (red). The correct behavior, $d^2E/dn^2 = 0$, (green) is linear [108].

Lany and Zunger [108] describe the failure of the band gap by explaining the incorrect behavior of the total energy as a function of the occupation number E(n). The exact functional must be linear while GGA and LDA exchange gives convex approximation to the E(n) due to the delocalization error. One of the best ways of dealing with the gap problem is using

hybrid functionals. This method is based on the mixing of Hartree-Fock exchange potential into LDA/GGA functional. The Hartree-Fock gives a concave approximation to the E(n) - opposite to the LDA/GGA case- (see Fig. 2.2). Therefore, a suitable balance between the HF and the LDA/GGA in the hybrid exchange-correlation functional can lead to a useful cancellation of errors.

$$E_{xc}^{hyb} = E_{xc}^{GGA} + \alpha(E_x^{HF} - E_x^{GGA}) \tag{2.22}$$

where α denotes the empirical mixing factor. $\alpha = 0.25$ is to be expected for the atomization energies of most molecules, while larger values may be more appropriate for total energies of atoms and molecules, and smaller values for atomization energies of molecules with nearly degenerate ground states of the unperturbed problem [109].

As mentioned before correct assessment of band gaps is necessary when solids are studied. There are various cases in which the band gaps are improved by using hybrid functionals. For diamond which is the main material studied in this thesis, GGA calculates the indirect band gap of 4.17 eV, while the hybrid functional (HSE06) computes the gap equal to 5.34 eV which has a very good accuracy compared to the experimental value of 5.48 eV [2].

The downside of the hybrid functional method is that these functionals are more expensive than local and semi-local functionals. In plane-wave DFT implementations, the hybrid functional calculations take at least one order of magnitude more processing time compared to the LDA calculations for systems with the same number of electrons. The reason is that the Hartree-Fock potential involves four center integrals in the plane-wave methods which are time-consuming but still in comparison to the GW and the Quantum Monte Carlo methods these functionals are much more affordable.

2.5 Super-cell Approach

Theoretical descriptions of defects and impurities in semiconductors are mostly based on DFT theory with LDA/GGA functionals employed to super-cell models. [110]. However, these calculations are affected by considerable uncertainties associated with:

1. Band gap problem

2. Super-cell finite size effects

As mentioned earlier, LDA and GGA generally exhibit a considerable underestimation of the band gap of semiconductors. This can affect the calculated defect formation energy [111, 112]. Therefore, defect calculations performed by these functionals generally require *ex post facto* corrections which are applied to the total energy after the self-consistent calculations [113].

Methods such as hybrid DFT [114–116] , GW [117], exact exchange or optimized effective potentials (OEPs) can be used for (almost) correct evaluation of the band gap [118–121] . Modeling the defect systems is done by construction of super-cells with periodic boundary conditions (PBC). Using DFT with PBC is ideal for description of pristine crystals where a small unit-cell can describe the bulk system [122]. When defects are introduced in the cell, the cell size has to be large enough to neglect the interactions between the periodic images of defects. However, even quite large super-cells at the limit of computational capabilities for the first principles quantum mechanical calculations correspond to very high concentrations of defects ($10^{19} - 10^{20}$ cm^{-3}). Therefore, the calculation of the properties of isolated defects (*e.g.*10^{14}) requires finite size effect corrections, especially for charged defects [123]. In this case, the strong and long-ranged Coulomb interaction between the localized charge distributions converge very slowly and, consequently, the super-cell sizes required to yield the converged energies become prohibitively large [122]. One way to overcome this problem is to perform calculations for super-cells with different size and extrapolate to the limit of infinitely large super-cell [124–127].

The problem with this approach is that it can get extremely demanding from the computational point [128]. The other way is to use a small super-cell then perform the correction schemes. Most common approaches consist correcting *a posteriori* the calculated formation energy. Different schemes have been proposed such as Makov and Payne (MP) [129], Freysoldt, Neugebauer, and Van de Walle (FNV) [130], and Lany and Zunger (LZ) [113]. In chapter five, we used the method introduced by Lany and Zunger (LZ). In this approach they describe how finite-size effects in the formation energy of charged defects can be accurately corrected by potential alignment in conjunction with a scaling of the Madelung-like screened first order correction term. The factor involved with this scaling depends only on the dielectric constant and the shape of the super-cell.

2.6 The Pseudopotential Method

Pseudopotential or in other word effective potential is used as an approximation to make the atomistic calculations simpler. In the chemical processes the valance shell electrons are more active than the core electrons. This is because they are less bound to nucleus and can participate in the chemical reactions and even move from one atom to the other, while the core electrons are almost insensitive to the changes from the external environment.

According to this fact one of the ways to speed up the quantum simulations is to substitute the core electrons in the self-consistent calculation of the charge density with a new external potential called pseudopotential V^{sp} which combines the potential of the nuclear charge with the core electrons potential. In this case, Schrödinger equation contains a modified effective potential term instead of the Coulomb potential terms raised from the core electrons. Depending on the quality of pseudopotential and the number of valence electrons considered, the results can be close to those of all-electron calculations. The pseudopotential approximation was introduced by Hans Hellmann in 1934 [131]. The valance electrons are described by pseudo-wavefunctions which are orthogonal to all core states. The pseudopotential functions are derived from an atomic reference state requiring that the pseudopotential and all-electron valance eigenstates must have the same energy and density outside a cut-off radius r_c. In this approximation one condition is that there is no significant overlap between core and valance wavefunctions. Outside of r_c the norm of the wavefunctions, core and valance must be identical to their corresponding all-electron wavefunctions.

There are different approaches to implement pseudopotentials. A recent approach that is gaining widespread acceptance is generalization of pseudopotentials and linear augmented plane-wave in a method called projector augmented wave (PAW). This method provides efficient and accurate density functional theory based calculations. As valance wavefunctions tend to oscillate quickly near ion cores many Fourier components are required to describe the wavefunctions accurately. For solving this problem, PAW approach transforms these rapidly oscillating wavefunctions into smooth wavefunctions. The new smooth wavefunctions can be dealt with lower

computational power.

$$|\psi_\mu\rangle = \tau|\tilde{\psi_\mu}\rangle \tag{2.23}$$

where $|\psi\rangle$ is all-electron wavefunction (Kohn-Sham single particle wavefunction), τ is the transformer and $|\widetilde{\psi}\rangle$ is the artificial pseudo wavefunction outside the core region (augmented region).

$$\tau = 1 + \sum_R \tau_R \tag{2.24}$$

In the above equation the τ_R is non-zero only within spherical argumentation region Ω_R. Outside this region the pseudopotential wavefunctions are equal to the all-electron partial waves but inside this region can be any smooth functions such as a linear combination of polynomials. τ_R acts only on the atom site R

$$\tau_R|\tilde{\phi_\mu}\rangle - |\phi_\mu\rangle - |\tilde{\phi_\mu}\rangle. \tag{2.25}$$

The partial wavefunction ϕ_μ is equal to the pseudo partial wavefunction $\tilde{\phi}_{mu}$ outside the core radius r_c. Since τ is linear, the wavefunction can be obtained from the pseudo wavefunction:

$$|\psi_\mu\rangle = |\tilde{\psi_\mu}\rangle + \sum_i (|\phi_\mu - |\tilde{\phi_\mu}\rangle)\langle\tilde{p_i}|\psi_\mu\rangle \tag{2.26}$$

here $\tilde{p_i}$ is the projected function and $\langle\tilde{p_i}|\tilde{\psi_\mu}\rangle = \delta_{i\mu}$. In this case, the charge density ρ cab be written as:

$$\rho(r) = \rho(\tilde{r}) + \rho^1(r) + \rho^{-1}(r) \tag{2.27}$$

the first term is the pseudo charge density outside the core region and it corresponds to $\tilde{\psi_\mu}$, the last two terms are charge densities inside the augmentation region.

2.7 Density Functional Tight Binding (DFTB)

Density Functional Tight Binding (DFTB) [132–134] is a semi-empirical method derived from DFT. This method is based on the second order expansion of the Kohn-Sham total energy of

initial charge density and its functional.

$$\begin{aligned} E = &[\sum_{i}^{occ}\langle\Psi_i|\hat{H}_0|\Psi_i\rangle] \\ &+ [-\frac{1}{2}\int\int^{'}\frac{n_0 n_0^{'}}{r-r^{'}} + E_{xc}[n_0] - \int V_{xc}[n_0]n_0 + E_{ii}] \\ &+ [\frac{1}{2}\int\int^{'}(\frac{1}{r-r^{'}} + \frac{\delta^2 E_{xc}}{\delta n \delta n^{'}})\delta n \delta n^{'}]. \end{aligned} \tag{2.28}$$

In this equation the wave function can be written as expanding to a linear combination of atomic orbitals (LCAO) for valance electrons:

$$\Psi_i(\mathbf{r}) = \sum_l c_l^i \phi_l(\mathbf{r}-\mathbf{R}) \tag{2.29}$$

In equation 2.28 the first term is the band structure (E_{BS}), the second term is a short-range repulsive two particle interaction and the last term is the electrostatic interaction accounting for charge fluctuations. This part can be replaced by a pair-wise potential

$$\frac{1}{2}\int\int^{'}(\frac{1}{r-r^{'}} + \frac{\delta^2 E_{xc}}{\delta\delta^{'}}|_{n_0})\delta n \delta n^{'} = \frac{1}{2}\sum_{\alpha\beta}\Gamma(R_{\alpha\beta})\Delta q_\alpha \Delta q_\beta \tag{2.30}$$

where $\Gamma_{\alpha\beta}(R_{\alpha\beta})$ is determined by the Coulomb interaction of two spherical charge distribution centered in the atoms α and β. Δq_α and Δq_β are atomic charge fluctuations.

By applying the two particle approximation, the Hamiltonian can be given as:

$$H_{\mu l}^0 = \begin{cases} \epsilon_\mu^\alpha, & \text{if } \alpha = \beta \text{ and } \mu = l \\ \langle\phi_\mu^\alpha|\hat{T} + V_{KS}^{\alpha,\beta}|\phi_\nu^\beta\rangle & \text{otherwise} \end{cases} \tag{2.31}$$

where $V_{KS}^{\alpha,\beta}$ stands for a pair of effective potentials. It acts on the electrons in the atoms α and β. By applying the variation principle, we have a self-consistent charge density functional theory (SCC-DFTB):

$$\sum_l c_l^{KS}(H_{\mu l}^0 - \epsilon_{KS}S_{\mu l}) = 0 \tag{2.32}$$

where $S_{\mu l}$ depict the overlap between the local pseudoatomic orbitals.

$$S_{\mu l} = \langle\phi_\alpha|\phi_\beta\rangle \tag{2.33}$$

Then, the total energy (eq. 2.28) can be rewritten as:

$$\begin{aligned} E = & \sum_{\mu l} c_{\mu}^{KS*} c_{\mu}^{KS} H_{\mu l}^{0} \\ & + \sum_{\alpha<\beta} V_{rep}^{\alpha\beta}(R_{\alpha\beta}) \\ & + \frac{1}{2} \sum_{\alpha\beta} \Gamma_{\alpha\beta}(R_{\alpha,\beta}) \Delta q_{\alpha} \Delta q_{\beta} \end{aligned} \tag{2.34}$$

where $V_{rep}^{\alpha\beta}(R_{\alpha\beta})$ is a distance dependent pair wise repulsion potential. By solving the equation 2.32 the eigenstates (c_l^{KS}) can be determined plus the first part of the equation 2.34 can also be determined. The second term of the equation 2.34 can be investigated by empirically fitting E_{Elec}^{DFTB} to the corresponding total energy E_{Elec}^{DFT}. The last term of this equation explains the role of the charge transfer.

The SCC-DFTB calculations in this work were carried out in the DFTB+ code [135].

Chapter 3

Thermal Stability of Nanodiamonds

3.1 Introduction

Phase-pure diamond based materials consist of polycrystalline diamond films, diamond nanoparticles and their aggregates. Their mechanical and optical properties as well as the large specific area of NDs offer many applications [66, 67]. Recently, it was found that they are nontoxic which makes them a very suitable candidate for drug delivery [136] and bio-labeling [54–56, 137]. For such biomedical applications NDs should be produced as small as possible to be comparable with biomolecules [55, 56, 137]. They can be produced either by a milling process or by the detonation method [46, 70]. Transmission electron microscopy studies have shown that NDs are polyhedra with a diamond core, partly covered by a shell of graphitic or amorphous carbon [66]. While the phase diagram between graphite and diamond is clear in the bulk, in the nano range the size of the clusters is critical, due to the relative contribution of the surface energy which increases with decreasing size. In addition, ab initio calculations have shown that in the size range of 1-3 nm, the morphology of the nanoparticles also plays an important role [74]. For example, the surface of clusters with cubic shape pretty much preserve the structure of bulk diamond [138, 139]. In contrast, relaxation of the surface of octahedral and cuboctahedral clusters leads to a transition from sp^3 to sp^2 bonding [140, 141].

Detonation NDs are in the size range of ∼2-5nm and experimental investigations indicate their graphitization temperature to be around ∼1400 K (for references see. *e.g.* Ref.[142]). Around ∼2000 K concentric shells of fullerenes are formed. Theoretical simulation of the an-

nealing has thus so far concentrated on NDs with a diameter of 2 nm in a temperature range up to 1800 K [142, 143], using classical force fields, or of NDs with a diameter of 1.3 nm at 2000 K, using quantum mechanical tight binding methods [144, 145].

A precondition for biological applications is to diminish the size of nanodiamonds. In this chapter I try to answer the following question: "How small can NDs be to begin with, in order to preserve the diamond core at elevated temperature?" Based on the average bond energies, NDs between 1.9 to 5.2 nm have been estimated to be more stable than fullerene structures [145]. This does not mean, however, that smaller NDs cannot be kinetically stable (metastable) up to high temperatures, once they had been formed. Therefore, I investigate NDs between 0.3 and 1.3 nm by simulated annealing, using quantum mechanical molecular dynamics (MD) with a non-empirical tight binding method. Since static investigations [145] as well as MD-studies on spherical and cubocathedral clusters [142] have pointed out the shape-dependence of graphitization, I investigate NDs with octahedral, cuboctahedral and cubic shape. Besides annealing in vacuum we also consider the effect oxygen on the graphitization process. Corrosion in actual biological environment (at room temperature) will not yet be investigated here, as my primary goal is to establish the size limit for NDs which can at all be created in some non-equilibrium process.

3.2 Simulation Details

For MD simulation of the thermal annealing we use the charge self-consistent density functional based tight-binging (SCC-DFTB) method [132–134]. The SCC-DFTB method has been well tested in carbon based systems and is known to reproduce *ab initio* results quite well [132, 133, 146–154]. This method has also been applied in earlier studies of NDs at T = 0 K [138, 139], and in dynamic simulation of fullerene formation from NDs [155]. Our tests with *ab initio* DFT on very small diamond clusters gave surface relaxations qualitatively very similar to the DFTB results. At the first step of our investigations we relaxed the NDs (without any surface passivation) in vacuum at 0 K, using a conjugate-gradient optimization. These structures were then exposed to successive isothermal MD annealing steps at increasing temperatures, to establish the temperature where graphitization (amorphization) occurs, and to investigate the

arising structures. In the MD simulations, carried out under NVT condition with the canonical ensemble numerically realized by the Anderson thermostat, we applied the temperature program shown in Fig.3.1.

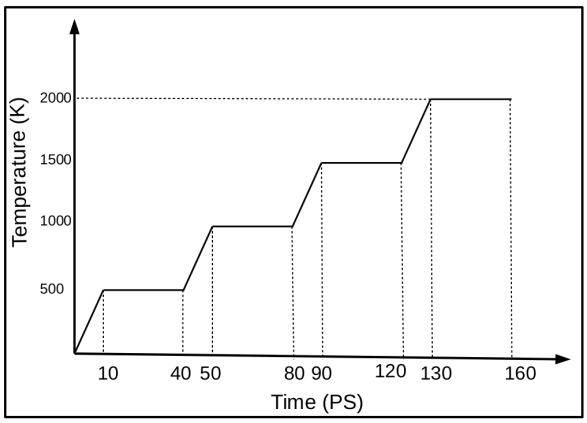

Figure 3.1: Temperature program of the annealing.

In a few cases, intermediate temperatures were also considered (always preceded and followed by 10 ps ramps). The time step for integrating the equations of motion was 2 fs. The clusters were put in a cubic vacuum box of the size l = 500 Å, to prevent interaction between periodically repeated images. The isothermal annealing time was chosen to be 30 ps, more by necessity than choice. Obviously, at low temperatures this is not sufficient to achieve thermal equilibration. However, tests at 1500 K up to 250 ps indicate that the results after 30 ps are already close to that. We have monitored the graphitization process by means of the percentage of purely sp^2, sp^3 and $sp^{(2+x)}$ bonded atoms with respect to the total number of carbon atoms. (These bonding configurations are defined here as follows: sp^2 means threefold coordinated, all of the atoms are in a plane with bond angles around 120 degree. sp^3 means fourfold coordinated in tetrahedral arrangement with bond angles around 109 degrees, and $sp^{(2+x)}$ means threefold coordinated but one of the neighbors is out of the plane.) The contribution of twofold and singly coordinated carbons will not be displayed. For the purpose of this work, we have considered the equality between the percentage of sp^2 and sp^3-bonded carbon as the "graphitization point", although the expression "amorphization point" could have been more appropriate. We note, that in the presence of oxygen, CO_x species are formed on the surface and they dissociate from it partly or

completely. CO_x species appear explicitly in our graphs only if the carbon is at least threefold coordinated, which is never the case for dissociated fragments. The decrease in the percentage of sp^3-bonded carbon (with respect to the total number of atoms, including dissociated ones) is a good indicator for the loss of the diamond structure.

3.3 Results and discussion

3.3.1 Relaxation at 0 K

It has been shown [139, 147, 151, 156, 157] that the surface graphitization of NDs depends on their shape, because of the different diamond-to-graphite transformation rate of the various diamond surfaces. Based on theoretical and experimental studies, the transformation rate of the (111) diamond planes to graphite-like sheets is higher than those of other planes like (110) or (100). NDs with an ideal octahedral shape are enclosed solely by (111) surfaces, so one expects easy delamination of the surface layers and conversion to graphitic planes. Here we compare octahedral diamond clusters to cube-shaped ones, with [100] surfaces only, and with cuboctahedral ones, having 64% (100) and 36% (111) facets. The investigations were started from the ideal T_d symmetry. Such diamond clusters can be built around an atom (atom-centered, or AC clusters) or around the tetrahedral interstitial position (TC clusters). For the AC and TC clusters considered, the number of atoms, the shape, and percentage of atoms with sp^2 and sp^3 hybridization after relaxation are given in table 3.1.

As can be seen, even relaxation at 0 K leads to the "graphitization" of octahedral clusters. The cuboctahedral clusters retain a larger percentage of sp^3-bonded atoms after relaxation; for small sizes the TC clusters less than the AC ones. Cube-shaped clusters contain predominantly sp^3-hybridized carbons even at small sizes, and centering plays a lesser role. Table 3.1 also shows the number of times the vacuum annealing up to 2000 K have been carried out, in order to estimate the statistical scattering. In case of octahedral clusters the "graphitization" occurs practically already at 0 K, so only one run was made. For clusters larger than 200 atoms only one run could be performed. The statistical scattering has turned out to be fairly low (see Figs.3.5 and 3.7). Since there is no reason to expect a significantly higher scattering in the presence of oxygen, the oxygen annealing was carried out only ones in each case.

Shape	Number of atoms	Center	Sp3-percentage in the relaxed structure	Sp2-percentage in the relaxed structure	Number of MD runs at each T 2000K
Octahedral (OC)	84	TC	1.2 %	66.7%	1
	16	AC	4.2 %	67.3%	1
	286	TC	1.0 %	79.7%	1
Cuboctahedral (CuOc)	66	TC	15.2 %	6.1%	4
	87	AC	48.3 %	10.3%	4
	208	TC	37.5 %	16.3%	4
	251	AC	69.7 %	0.0%	1
Cuboid (Cu)	94	TC	48.9%	0.0%	4
	171	AC	55.6%	0.0%	4
	279	AC	78.9%	0.0%	1
	428	TC	70.6%	0.2%	1

Table 3.1: Description of the clusters considered in the MD study and the number of independent identical annealing cycles up to 2000 K.

3.3.2 Annealing in vacuum

Fig.3.2 illustrates the structural changes in **octahedral clusters (OC)** from the ideal and the relaxed structure through snapshots taken during the temperature program of Fig.3.1. The smallest cluster (TC 84) has no sp^3-bonded carbon atom by the end of the annealing, but in larger clusters the sp^3 content increases somewhat upon annealing , as shown also in Fig.3.3. The end results is amorphous carbon with some tetrahedral carbon content.

In **Cuboctahedral (CuOc)** clusters only about 36% of the surface is (111), so they are expected to be more resistant to surface graphitization than octahedral ones. As shown in Fig. 3.4, larger clusters of this type retain a considerable diamond core up to very high temperatures (in a short anneal), whereas small clusters are quickly and entirely graphitized between 1100 and 1300 K. Over 200 atoms the sp^3 content remains fairly constant up to 2000 K, and higher temperatures are needed for a significant reduction, as shown in Fig. 3.5. While after annealing up to 1500 K the TC 208 cluster can more or less be regarded as tetrahedral amorphous carbon, the AC 251 cluster definitely retains its diamond core, covered by an $sp^{(2+x)}$ surface layer. (In that particular case even 30 ps "accelerated" MD cycles up to 5000 K did not bring about the loss of the diamond core).

Cube-shaped clusters with only [100] surfaces are most stable against graphitization. Even smaller clusters retain a diamond core in short anneals up to about 1000 K and, as can be seen

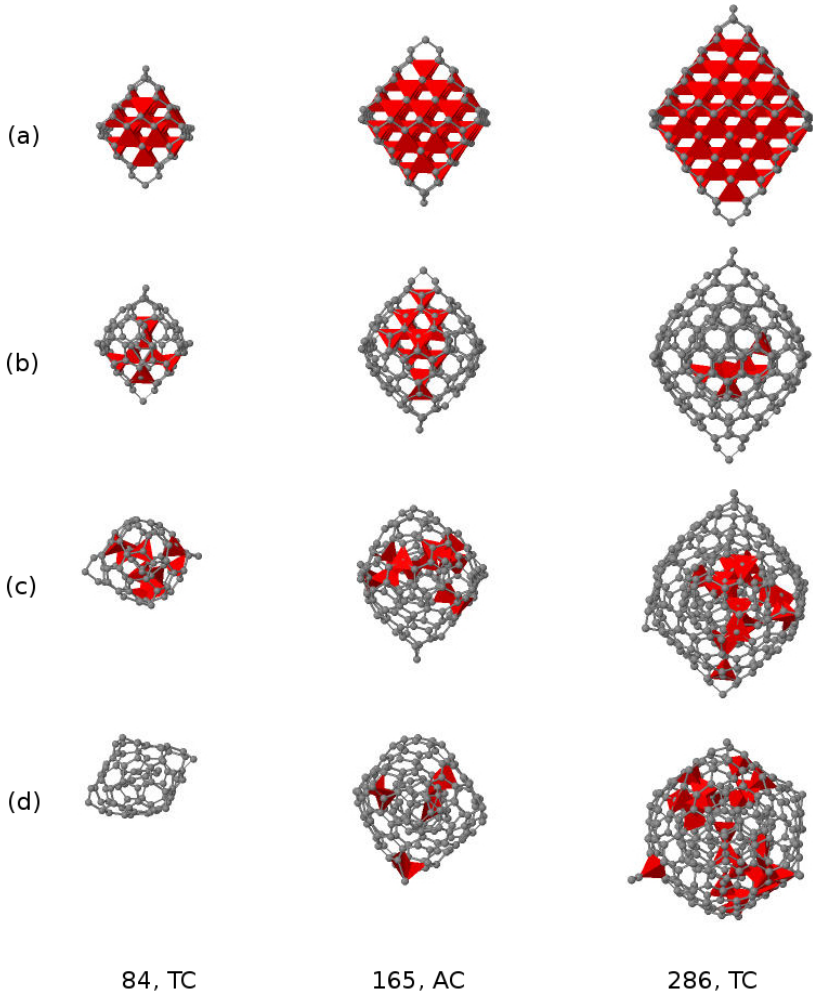

Figure 3.2: Structure of octahedral clusters. (a) unrelaxed (initial), (b) relaxed, (c) after annealing in vacuum up to 1500 K and (d) after 160 ps at 2000 K. The carbon atoms are illustrated with grey spheres, and atoms with sp^3 hybridization are shown as red polyhedra.

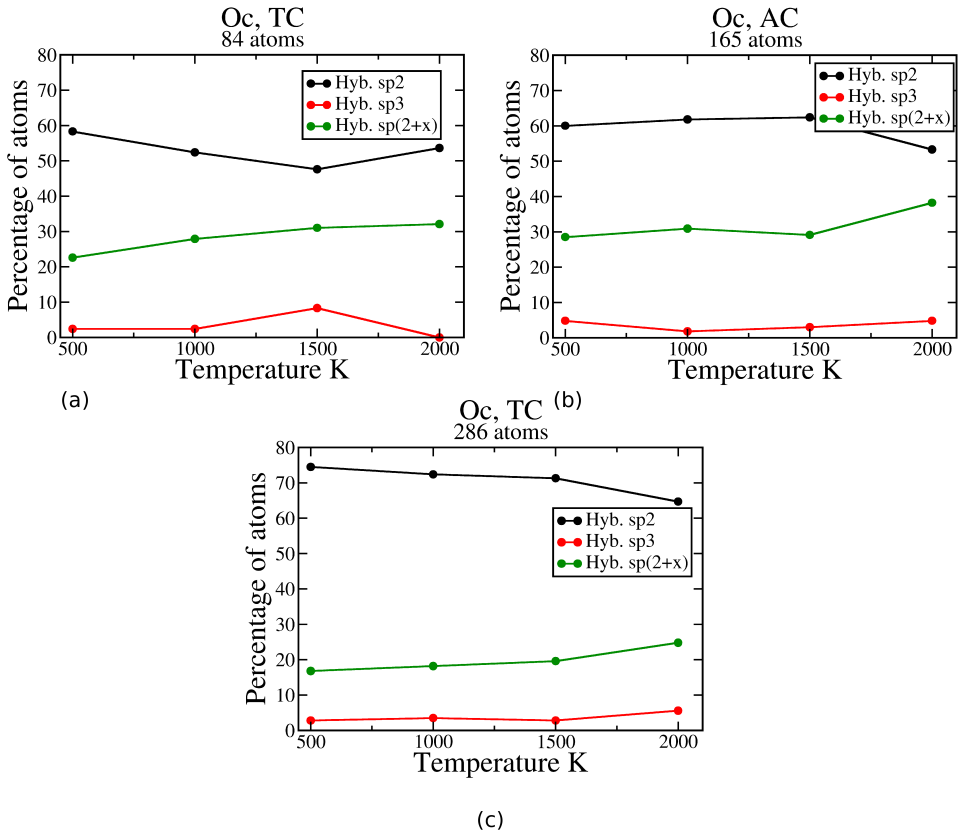

Figure 3.3: Structure evolution of the octahedral clusters upon vacuum annealing. (a) 84 atoms, (b) 165 atoms and (c) 286 atoms.

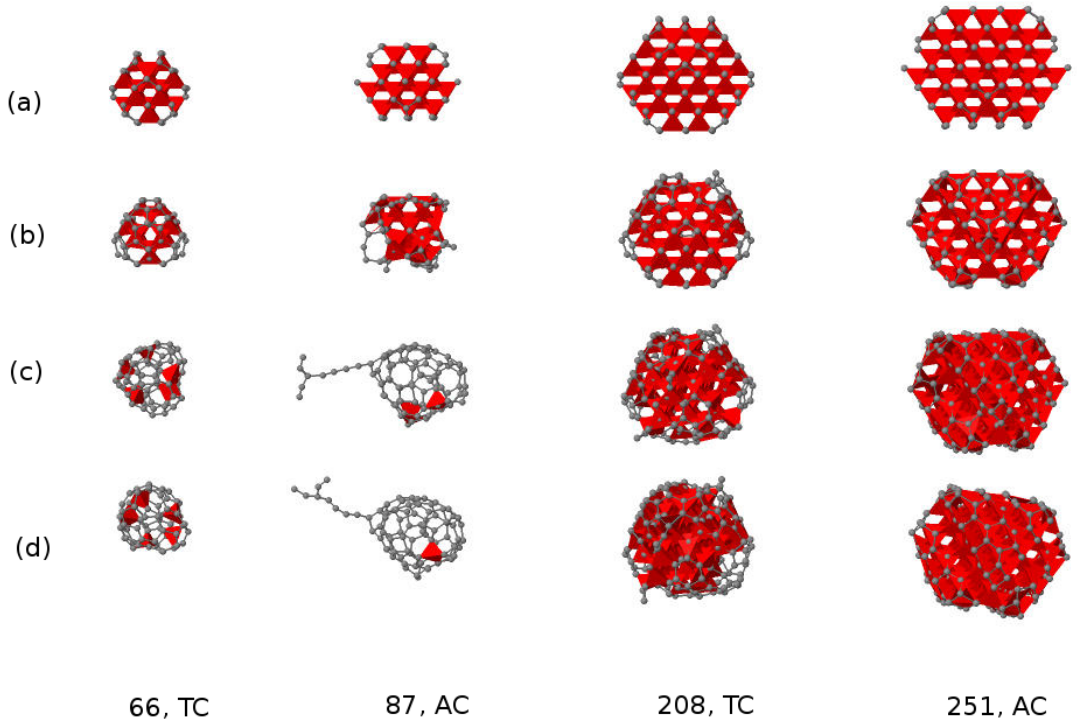

Figure 3.4: Structure of cuboctahedral clusters. (a) unrelaxed (initial), (b) relaxed, (c) after annealing in vacuum up to 1500 K and (d) after 160 ps in 2000 K.

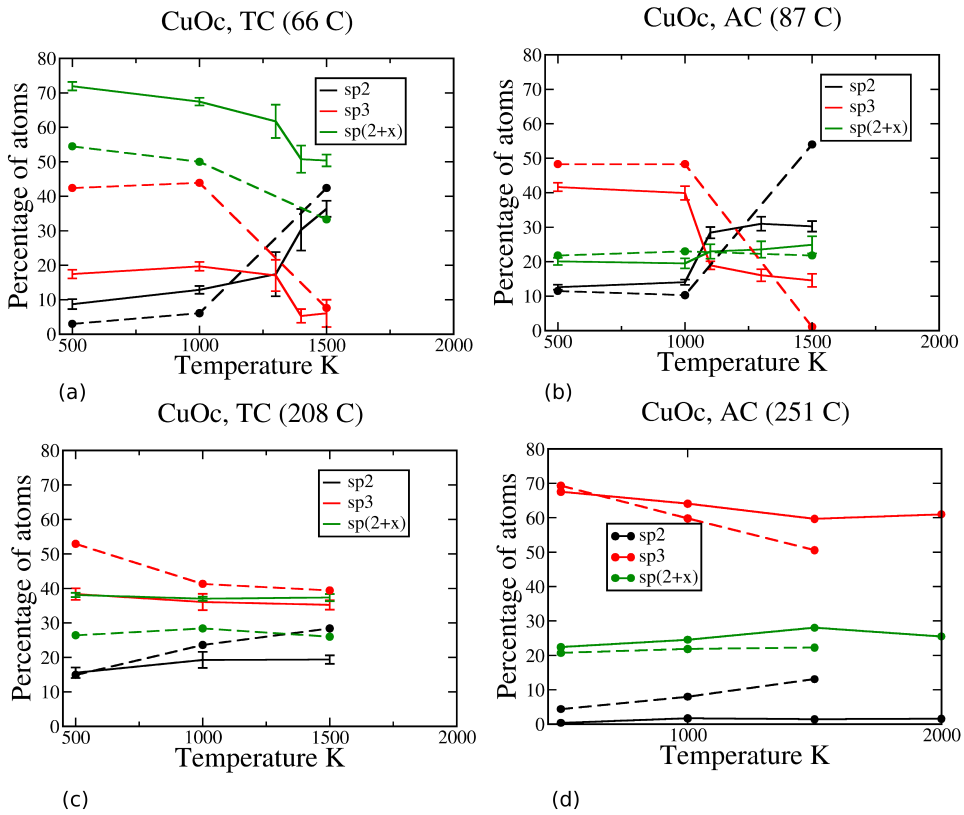

Figure 3.5: Structural evolution of the cuboctahedral clusters upon annealing in vacuum (solid lines) and in oxygen (dashed lines). (a) 66 atoms, (b) 87 atoms, (c) 208 atoms and (d) 251 atoms. Data points for the vacuum anneal represent the average of four independent annealing cycles, starting from the same ideal structure. Error bars depict the root mean square of the deviations from the average in the four runs.

in Fig. 3.6, larger clusters even above 1500 K.

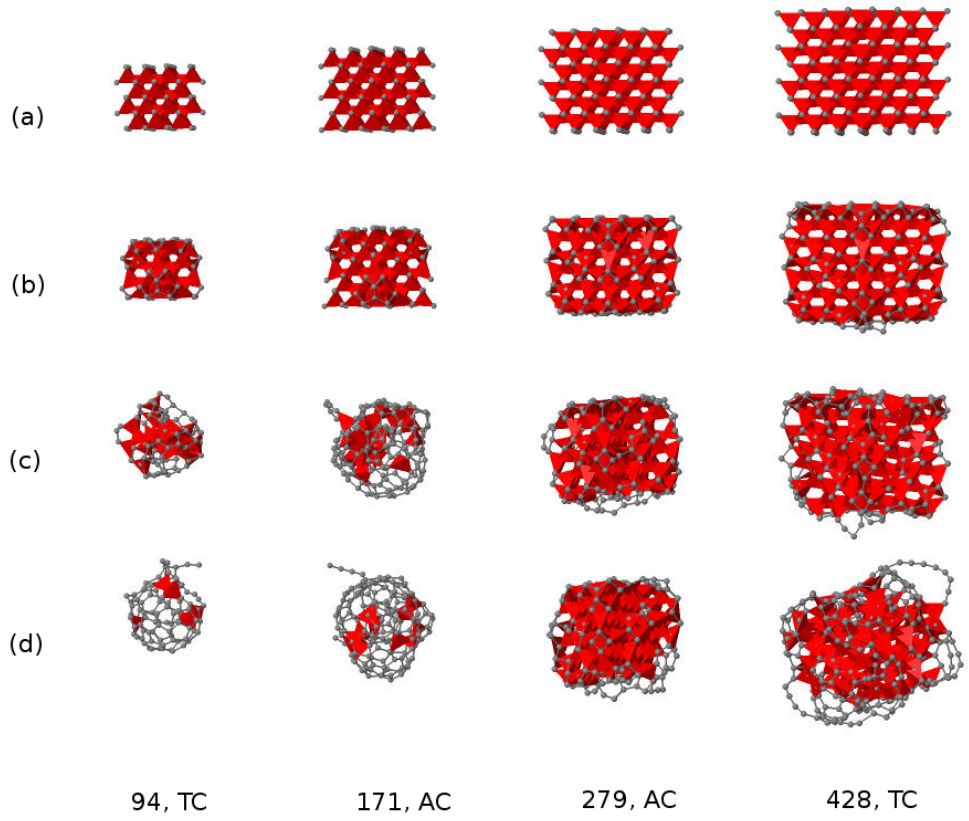

Figure 3.6: Structure of cube-shaped clusters. (a) unrelaxed (initial) structures, (b) relaxed structures, (c) after annealing in vacuum up to 1500 K and (d) after 160 ps in 2000 K.

Fig. 3.7 shows the structural evolution of the cube-shaped clusters with temperature. For clusters below 200 atoms the "graphitization temperature" is between 1400-1600 K (for short annealing times), significantly higher than for the cuboctahedral clusters. In larger clusters "graphitization" occurs only in short annals at very high temperatures (∼2500 K). We have continued the 1500 K anneal for the AC 279 cluster, up to 250 ps. As shown in Fig. 3.8, the 1500 K data point in Fig. 3.7 (at 30 ps) was already close to equilibration. Therefore, these clusters can survive realistic annealing times at 1500 K.

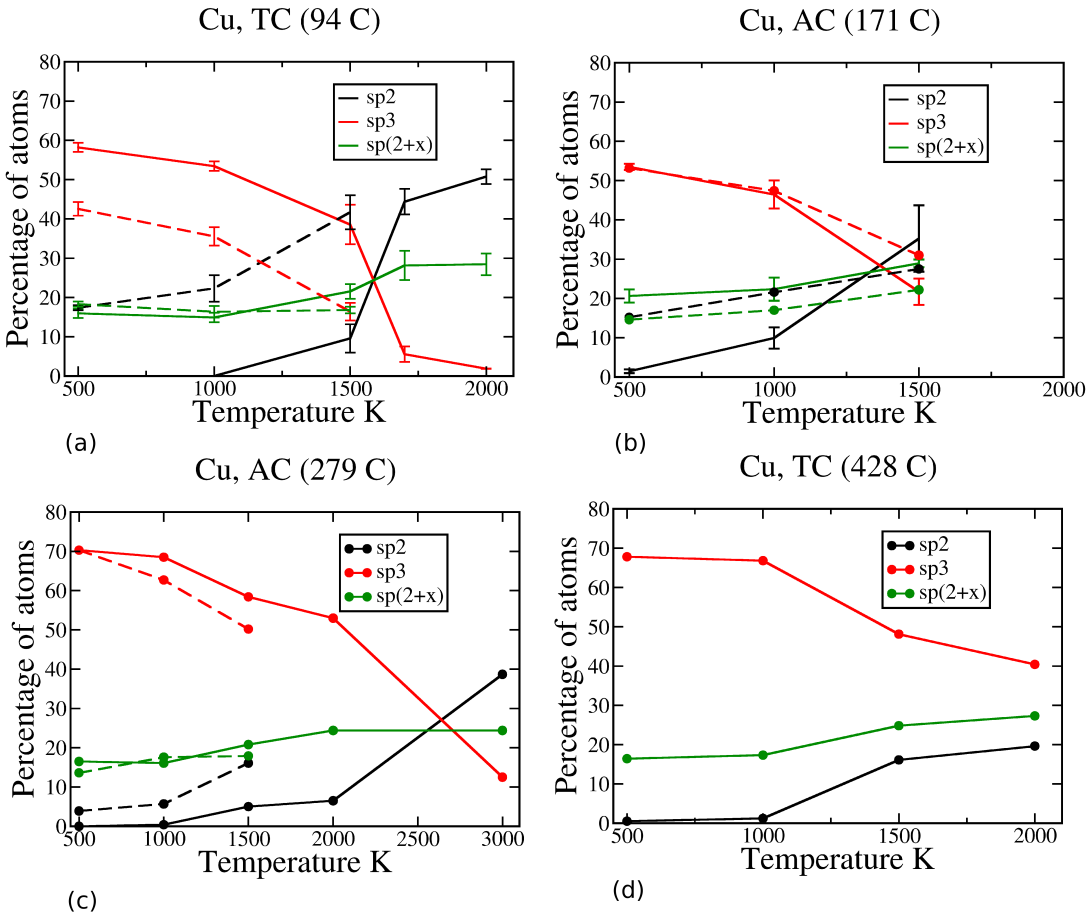

Figure 3.7: Structural evolution of the cube-shaped clusters upon annealing in vacuum (solid lines) and in oxygen (dashed lines). (a) 94 atoms, (b) 171 atoms, (c) 279 atoms and (d) 428 atoms. (N.B.: for small percentages the error bar is too small to be seen.

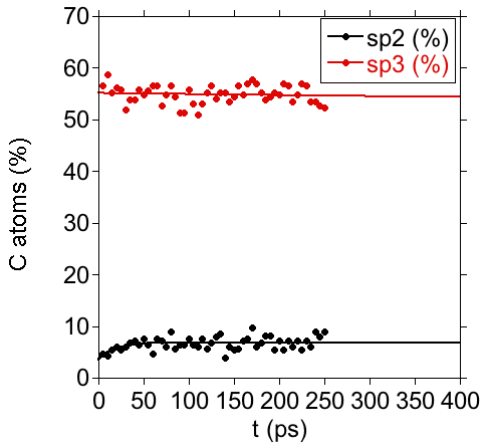

Figure 3.8: Time evolution of the sp^3 and sp^2 content in the 279 atom cluster during an additional anneal at 1500 K. In vacuum. Here t = 0 corresponds to t = 90 ps in Fig. 1. (The 1500 K data point of Figs 3.5 and 3.7 appear at 30 ps here.) The solid curves are exponential extrapolations.

3.3.3 Annealing in the presence of oxygen

Nanodiamonds are often prepared or being treated after synthesis in the presence of oxygen which is known to etch carbon but can also form stabilizing species on the surface. Therefore, we have also performed simulated annealing in the presence of oxygen. For the sake of simplicity, we assumed O_2 molecules in the simulation box. In order to ensure a constant "exposure" of the clusters of various sizes, the number of the O_2 molecules have been set to be 1/3 of the number of surface carbon atoms (in the ideal structure).

Figs. 3.9 and 3.10 compare the structure of cuboctahedral and cube-shaped clusters, respectively, after annealing up to 1500 K in vacuum and in oxygen, while Figs. 3.5 and 3.7 (dashed lines) show the structural evolution during the annealing cycles. As can be seen, the primary effect of oxygen is the saturation of surface atoms, leading to an increased percentage of sp^3 carbon at the early stage of the annealing (with respect to the vacuum anneal). At later stages, the non-sp^3 surface carbon is etched away in the first place. In the larger cuboctahedral structures the etching seems to lead to a cube-like shape.

Though oxygen accelerates the graphitization process, at 1500 K a somewhat smaller diamond core (0.8 nm) is still preserved in clusters with ∼250 atoms. Here again, we have checked the effect of extending the annealing time of the 279 atom cluster at 1500 K up to 250 ps. As

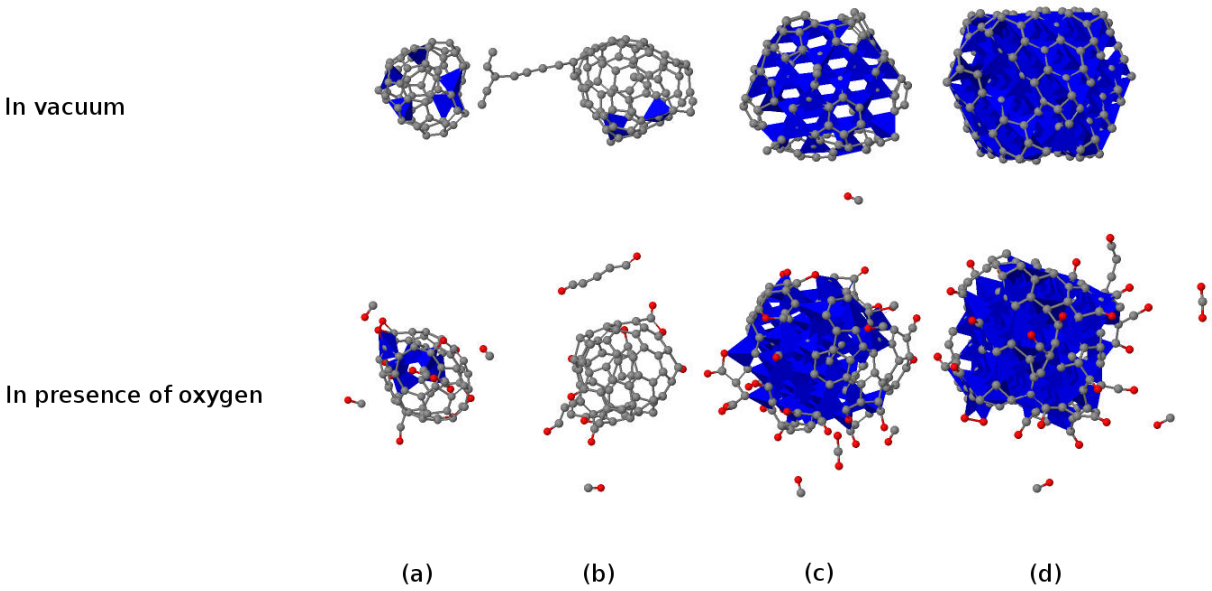

Figure 3.9: Structure of cuboctahedral clusters at 1500 K in vacuum and in presence of O_2. Clusters of (a) TC 66 (b) AC 87 (c) TC 208 and (d) AC 251 carbon atoms. Grey and red spheres represent carbon and oxygen atoms, respectively. Carbon atoms with sp^3 hybridization are shown as blue polyhedra.

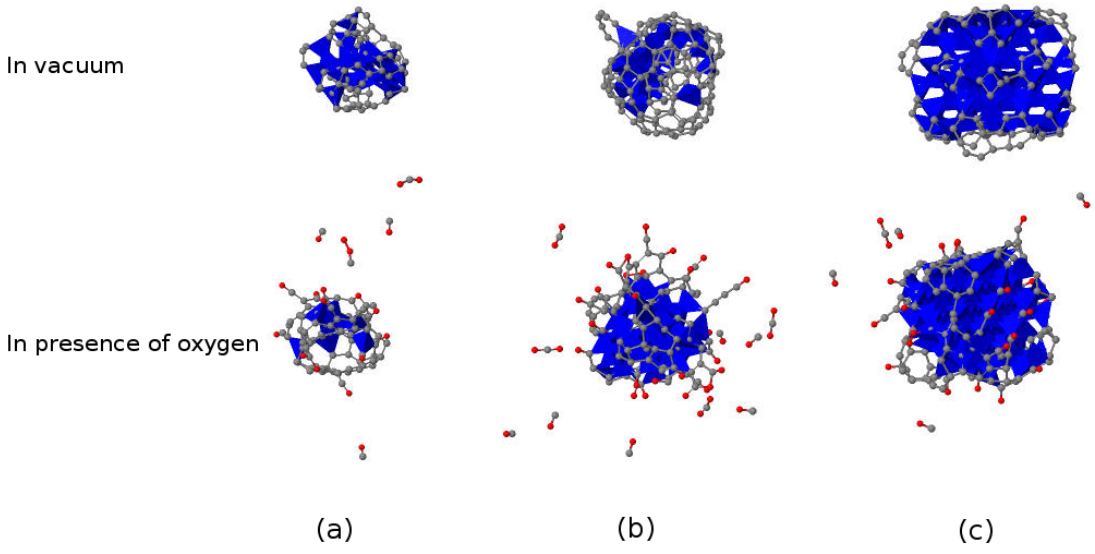

Figure 3.10: Structure of cube-shaped clusters at 1500 K in vacuum and in presence of O_2. Clusters of (a) TC 94 , (b) AC 171, and (c) AC 279 carbon atoms.

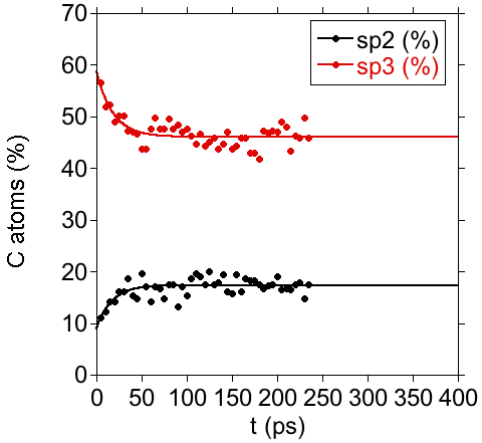

Figure 3.11: Time evolution of the sp^3 and sp^2 content in the 279 atom cluster during an additional anneal at 1500 K in oxygen. Here t = 0 corresponds to t = 90 ps in Fig. 3.1. (The 1500 K data point of Figs 3.5 and 3.7 appear at 30 ps here.) The solid curves are exponential extrapolations.

shown in Fig. 3.11, when thermal equilibration is reached, the sp^3 content is still about 47% and at the end the cube-shaped diamond core is still present.

3.4 Conclusion of the MD study

By performing MD simulation of the annealing in vacuum and in the presence of oxygen, we have found that diamond clusters of cubic or cuboctahedral shapes with over ∼250 atoms can survive long term annealing up to 1500 K. The primary role of oxygen is the saturation of surface carbon atoms and the etching of the graphitic part, i.e. to increase the sp^3-ratio. (The etching seem to result in cubes even in the case of cuboctahedral clusters.) Our results mean that if (100) faceted nanodiamonds as small as 1 nm in diameter are formed during synthesis, they will be kinetically stable up to 1500 K, although the thermodynamic stability limit was estimated to be 1.9 nm [145]. This results strengthen the position of nanodiamonds in biological and medical applications.

Chapter 4

Formation of Nitrogen-Vacancy (NV) Center in Bulk Diamond

4.1 Introduction

The NV center is a well-known point defect in diamond; a nitrogen atom substitutes a carbon atom in the lattice, adjacent to a vacancy (Fig. 4.1a). This defect can be found in the neutral NV(0) state or negatively charged NV(-) state with the symmetry of C_{1h} [9] and C_{3v} [158], respectively. The NV defect produces two highly localized defect states in the fundamental gap of diamond [159]. The lower lying a_1 level is fully occupied, the higher lying double degenerate e level is occupied by one electron in NV(0) and is occupied by two electrons in NV(-), forming a triplet state (S=1). The excitation of this center can be well described by promoting one electron from the a_1 level to the e level, while in the luminescence process the excited electron from the e level goes back to the lower a_1 level, see Fig. 4.1b [158, 160]. Due to the non-zero spin, the NV(-) center can interact with external magnetic fields or electron spins. Exploring the NV(0) and NV(-)-centers can lead to the following applications.

Both NV(-) and NV(0)-centers in nanodiamonds are leading candidates for noninvasive bioimaging [161]. Out of these two charge states of the NV-center, NV(-) has a strong and stable luminescence at the room temperature: a phonon side band at around 700 nm wavelength corresponding to red light [20, 162]. NV(-) can be probed by optically detected magnetic resonance (ODMR) at a single defect level even at room temperature [24] which is the basis of

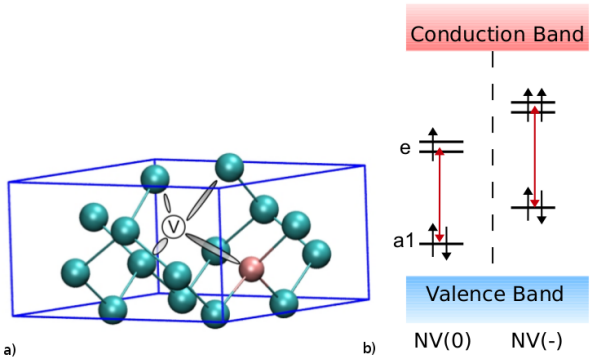

Figure 4.1: Nitrogen-vacancy (NV) defect in bulk diamond. a) Schematic picture of the geometry of the NV-defect. b) Levels of this defect in the band gap in the neutral and in the negatively charged state. The excitation (de-excitation) from (to) the $a1$ level to(from) the e level is responsible for the absorption(emission) of the neutral and negatively charged defects.

quantum optics protocols that can be applied to sense magnetic [35, 36] and electric fields [38], or temperature [39–41] at atomic scale. It has been recently proposed that NV(-) defects may realize a large-scale quantum simulator on the diamond surface operating at room temperature [163].

NV(-) can be routinely found in natural Type Ib diamonds, but generally, the concentration of NV natural or as-grown synthetic diamonds is very low for applications [164]. The concentration of NV can be substantially increased by creating vacancies in N-doped diamond by irradiation with energetic neutrons, electrons, or ions [13, 165], followed by annealing above $\sim 600°C$, where vacancies become mobile [20, 166]. According to the present consensus in the literature, mobile vacancies can get trapped by substitutional nitrogen (N_s) and form NV centers [167–170]. Understanding the formation of NV defects requires accurate knowledge about the formation energy of the isolated constituents, N_s and the vacancy (V), and about competing defect complexes (NV, N_2V, V_2, NVH). The mobility of the species and the energy of complex formation may depend on the charge states; thus, it is highly critical to determine the charge transition levels of these defects across the band gap. Since diamond is a wide gap material, it is extremely difficult (or sometimes impossible) to determine deep adiabatic (thermal) charge transition levels by traditional techniques such as deep-level transient spectroscopy (DLTS). The vertical ionization energies may be obtained by optical excitation of the samples, but it is not

trivial to interpret the signals from these experiments. Fortunately, recent advances in density functional theory have made it possible to calculate transition levels with very good accuracy.

In this chapter, advanced DFT calculations are used to investigate the formation and excitation energies, the charge transition levels, and the diffusion activation energies for nitrogen and vacancy-related defects in diamond. The focus was specifically on the formation of small complexes, such as the divacancy (V_2), the pair of N_s atoms (N_2), the NV, and the N_2V, from isolated constituents, considering all possible charge states of these defects.

We have analyzed possible formation routes of NV and concluded that the concentration of NV can not be significantly increased by increasing the vacancy concentration due to the preference for V_2 over NV formation. In contrast, the formation of NV can be expected to dominate over V formation *during* irradiation. In addition, the V_2 defects crucially influence the charge state of NV and that having the latter predominantly in the negative charge state requires the reduction of the V_2 concentration.

4.2 Method

Defect calculations in solids are almost always carried out by applying two basic approximations: first, the adiabatic principle, *i.e.*, the separation of the electron problem from that of the lattice vibrations, and second, the one-electron approximation, which expresses either the wave function (in Hartree-Fock theory) or the density (in the Kohn-Sham theory) of the many-electron system in terms of independent single-particle states. The neutral vacancy (V(0)), in diamond is the school book example for the failure of both of these approximations. Strong electron-phonon coupling gives rise to a dynamic Jahn-Teller effect, obliterating in room-temperature measurements the static Jahn-Teller distortion predicted by theoretical calculations at 0 K, and the degenerate ground state cannot be described with just one single-particle configuration. Still, the system sizes necessary to model V-related defects in the solute limit are just too big for abandoning these approximations. Therefore, they will still be used in this study in the hope that in calculated energy differences the lack of many-body effects and electron-phonon coupling causes errors of 0.1-0.2 eV at most due to error compensation. As I will show, comparison of our results to experimental data supports this expectation.

4. FORMATION OF NITROGEN-VACANCY (NV) CENTER IN BULK DIAMOND

Nitrogen- and V-related defects were investigated thoroughly earlier by using DFT within the local density or the generalized gradient approximation (LDA and GGA) and by semiempirical methods [165, 171–176]. While these studies have revealed the basic configurations of the relevant defects, calculated gap levels and optical transitions were impaired even in *ab initio* calculations by the electron self interaction error involved with the standard approximations of DFT. Precise calculations of these data is important for defect identification, but the correct reproduction of the defect levels is also crucial for calculating relative energies of different configurations and for the activation energy of diffusion [11]. The present calculations have been carried out in the framework of the generalized Kohn-Sham theory [177] by using the screened hybrid functional of Heyd, Scuseria, and Ernzerhof (HSE06) with the original parameters (0.2Å^{-1} for screening and 25 percent mixing) [178]. HSE06 in diamond happens to be nearly free of the electron self-interaction error and is capable of providing defect levels and defect-related electronic transitions within ~ 0.1 eV to experiment [159, 179].

I have used the Vienna Ab initio Simulation Package (VASP) 5.2.12 with the projector-augmented wave method (applying projectors originally supplied to the 5.2 version) [172]. To avoid size effects as much as possible, a 512-atom supercell was used in the Γ approximation for defect studies. Parameters for the supercell calculations were established first by using the GGA exchange of Perdew, Burke, and Ernzerhof (PBE) [173] in bulk calculations on the primitive cell with a 8×8×8 Monkhorst-Pack (MP) set for Brillouin-zone sampling [174]. (Increasing the MP set to 12×12×12 has changed the total energy by <0.002 eV). Constant volume relaxations using a cutoff of 370 eV in the plane-wave expansion for the wavefunction and 740 eV in the plane-wave expansion for the charge density resulted in an equilibrium lattice parameter of a_{PBE} = 3.570 Å. Increasing the cutoff to 420 and 840 eV for the wavefunction and charge density, has changed the lattice constant by only 0.003 Å. Therefore, considering the demands of the supercell calculations, the lower cutoff was selected. An HSE06 calculation with the 8×8×8 MP set and 370 and 740 eV cutoff for the wavefunction and charge density, respectively, resulted in the lattice constant, the bulk modulus , and the indirect band gap, shown in table 4.1 in very good agreement with the experimental values.

Defects in the supercell were allowed to relax in constant volume until the forces were below 0.01 eV/Å. Diffusion activation energies were determined by the nudged elastic band method

	Theory	Experiment
Lattice constant, Å	3.545	3.567
Bulk modulus, GPa	425	443
Indirect band gap, eV	5.34	5.48

Table 4.1: Comparing the experimental and theoretical data for lattice constance, bulk modulus and indirect band gap for the diamond (see, e.g., Ref. [177]).

(NEB) [180].

4.2.1 Charge transition levels (CTL)

The formation energy of a defect D in its charge state q is a function of the electron chemical potential (Fermi level):

$$E^{D,q}(E_F) = E^{D,q}_{tot} - E^{bulk}_{tot} - \sum_{\alpha} \mu_\alpha n_\alpha + q(E_V + E_F + \Delta V) \tag{4.1}$$

where equation $E^{D,q}_{tot}$ is the total energy of the defect system, E^{bulk}_{tot} the total energy of the unperturbed host, n_α the number of extra atoms of species α needed to create the defect D, and μ_α is the corresponding atomic chemical potential. E_F is referred to the valance band maximum (VBM) E_V and is varies between zero and the band-gap (E_g). ΔV is the term used for alignment the electrostatic potentials of the bulk and the defective supercell.

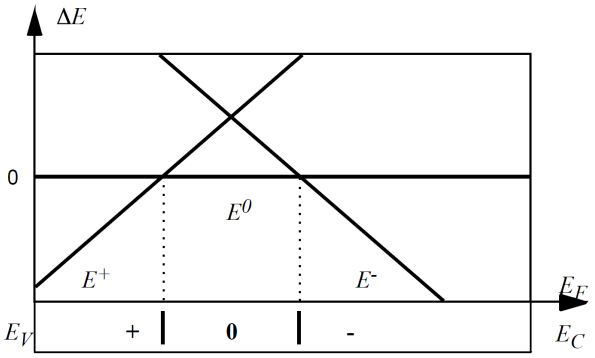

Figure 4.2: Relative energies of the different charge states of the same complex show which one is in equilibrium as a function of the Fermi-level. The Fermi-level positions where the charge state changes are called occupation levels, and are often incorporated in a band diagram showing the charge state below and above.

The charge transition levels correspond to the specific values of the Fermi level for which two

charge states have equal formation energies (see Fig. 4.2). Lets consider charge states q and q'. Equating the expression of the formation energies defined in Eq. 4.1; the value obtained for the charge transition level $\epsilon(q/q')$ is:

$$\epsilon(q/q') = \frac{E_{tot}^{D,q} - E_{tot}^{D,q'}}{q - q'} - (E_V + \Delta V). \tag{4.2}$$

For the Fermi-level positions below $\epsilon(q/q')$ the defect is stable in charge state q, while for Fermi-level positions above $\epsilon(q/q')$, the defect is stable in the charge state q' (see Fig. 4.2). The total energies of charged systems, $E_{tot}^{D,q}$, in Eq. 4.2 must be corrected to speed up the convergence with respect to the supercell size. The size effect arises from the periodic repetition of the charged defect and of the compensating Jellium charge. The scheme of Lany and Zunger has been applied [113, 181]. In a recent comparative paper on charge corrections [128], the Lany-Zunger scheme [as described there by Eqs. (15) and (20)] was found to work best for defects with medium localization.

4.3 Results of the charge transition levels

By applying HSE06 functional, we have calculated the CTLs for the N_s and V and their related complexes such as NV, N_2V, V_2, NVH. We were able to reproduce the experimentally observed electronic transitions of these defects with an accuracy better than 0.2 eV and without any *a posteriori* correction. In addition, we have also calculated all possible charge states of these defects which are needed to study the complex formation of these defects. The results are summarized in table 4.2.

4.4 Creation of the NV(-) center

Having calculated the formation energy in different charge states, it was possible to calculate CTLs shown in Fig. 4.3. The relative position of CTL will be of great importance to establish the charge state of coexisting defects. In addition, the formation energies allow us to determine the CTLs.

The possibility of manipulating the optical emission and the magnetic states of the NV center makes it a desirable defect for many applications. Therefore, control over the concentration

		Vertical		Adiabatic	
Defect	CTL	HSE06	Exp.	HSE06	Exp.
N_s	(+/0)	E_C-3.1	E_C-3.3[a]	E_C-1.8	E_C-1.7[b]
	(0/-)	E_V+4.9		E_V+4.6	
V	(2+/+)	E_C-5.0		E_C-4.9	
	(+/0)	E_C-4.5		E_C-4.4	E_C-4.3[c]
	(0/-)	E_V+2.1		E_V+2.0	
	(-/2-)	E_V+4.8		E_V+4.9	
NV	(+/0	E_C-4.6		E_C-4.4	
	(0/-)	E_V+2.7	E_C-2.6[d]	E_V+2.7	
	(-/2-)	E_V+4.9		E_V+4.9	
N_2	(+/0)	E_C-4.4		E_C-4.0	E_C-4.0[e]
N_2V	(+/0)	E_C-4.8		E_C-4.7	
	(0/-)	E_V+3.3		E_V+3.2	
V_2	(+/0)	E_C-4.3		E_C-4.3	
	(0/-)	E_V+2.4		E_V+2.3	
	(-/2-)	E_V+3.2		E_V+3.2	
NVH	(+/0)	E_C-4.9		E_C-4.5	
	(0/-)	E_V+2.6		E_V+2.4	E_V+2.4[f]
	(-/2-)	E_V+4.6		E_V+4.4	

Table 4.2: Vertical and adiabatic charge transition levels, Comparison of the vertical and adiabatic charge transition levels, calculated by HSE06 and experiment Donor levels are given with respect to EC, and acceptor levels are given with respect to E_V (in electron volts) [2].
a) Since the excited effective-mass-like states in diamond are within 0.1 eV of the band edges, within the accuracy of the calculations, the vertical ionization energy of N can be compared to the observed A band of the optical absorption spectrum (Ref. [182]).
b) Thermal activation energy of conductivity (Ref. [182]).
c) DLTS (Refs. [183, 184]).
d) PL microscopy (Ref. [185]) *e*) Photoconductivity (Ref. [186]).
f) Absorption (Ref. [164]).

and charge state of this defect is required. However, these depend on the concentration of other defects. Assuming equilibrium conditions, the calculated formation energies allow us to predict the relative concentrations in different charge states by solving the neutrality equation, considering all defects i, with charge q_i,

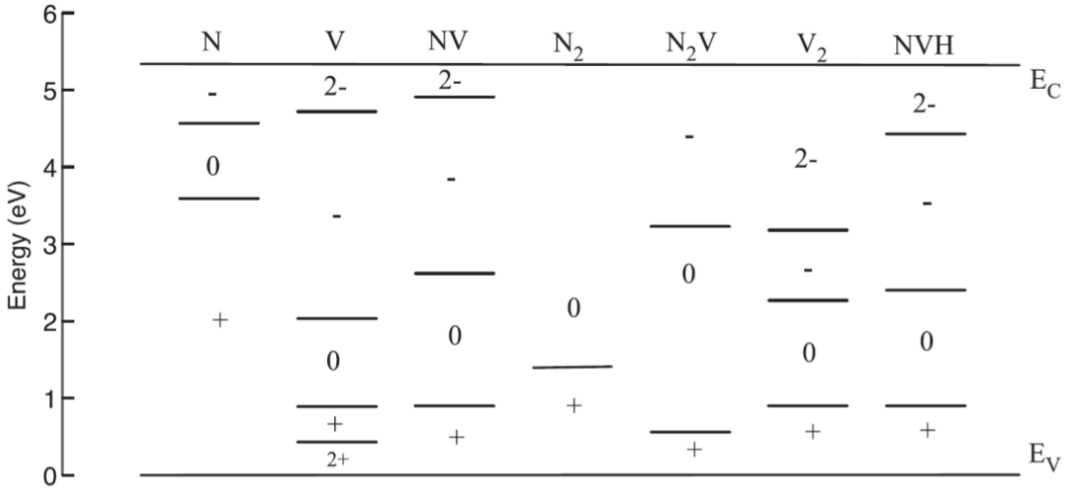

Figure 4.3: Comparison of the adiabatic charge transition levels.

$$\begin{aligned} N_C exp[-\frac{E_C - E_F}{kT}] + \sum_i |q_i|(N_{Ai} - p_{Ai}) \\ = N_V exp[-\frac{E_F - E_V}{kT}] + \sum_i |q_i|(N_{Di} - n_{Di}) \end{aligned} \tag{4.3}$$

where

$$N_C = 2(\frac{2m_e^* \pi kT}{h^2})^{3/2}; N_V = 2(\frac{2m_h^* \pi kT}{h^2})^{3/2} \tag{4.4}$$

are the effective (number) densities of states in the conduction and valence band of diamond, calculated from the density-ofstates mass of the electrons, $m_e^* = 0.57m_0$, and the holes, $m_h^* = 0.8m_0$, respectively. The remaining terms in Eq. 4.3 are the occupancies of the acceptor and donor levels, determined by the Fermi-Dirac distribution and the degeneracy factors g

$$\begin{aligned} p_{Ai} = N_{Ai}[g_{Ai} exp(\frac{E_F - E_{Ai}}{kT}) + 1]^{-1}; \\ n_{Di} = N_{Di}[g_{Di} exp(\frac{E_{Di} - E_F}{kT}) + 1]^{-1} \end{aligned} \tag{4.5}$$

The defect concentrations in Eq. 4.3 must be determined from the calculated energies of formation $E^{i,q}_{form}$ as

$$N_{(A,D)i} = N^0_{(A,D)i} exp(\frac{E^{i,q}_{form}}{kT}) \tag{4.6}$$

for all acceptors (A) and donors (D). Here N^0_i is the density of i sites in the perfect lattice. I have calculated the defect formation energies with reference to the perfect 512-atom diamond supercell and the chemical potential of nitrogen in the gas phase, μ_N, as

$$\begin{aligned} E^{i,q}_{form} = E^q[C_{512} : N_n V_m] - \frac{512 - n - m}{512} E[C512] \\ - n\mu_N + q(E_F + E_V + \delta V_{aling}) + E^q_{corr} \end{aligned} \tag{4.7}$$

where $E^{i,q}_{form}$ and δV_{aling} are the charge and potential alignment corrections, respectively, and E_F is the Fermi energy with respect to E_V. In this study the μ_N have chosen to be half of the HSE06 energy of an N_2 molecule, E(N_2) = 22.78 eV, as a reference, to list the calculated formation energies in Table 4.3. (We also provide the formation energy of the NVH complex, using the energy of a hydrogen atom in a surface C-H bond on the 2×1-reconstructed (001) surface with 22 carbon layer, as chemical potential for the hydrogen [187].) Since both Eqs. 4.3 and 4.7 contain the Fermi energy, this system of equations has to be solved self-consistently. This has been done by our partner Professor Adam Gali in various scenarios.

In calculating the diffusion barriers by the NEB method, I have followed the route given in Ref. [173]. While my result for V(0) is identical with that of the LDA calculation (Table 4.4), the HSE06 barrier for V(-) is substantially higher, giving rise to diffusivities 10^6 times smaller than that of V(0) at 1000 K, in agreement with experiment [188].

Although NV(-) centers are in practice usually not created in equilibrium processes, the study of scenarios leading to thermal equilibrium will provide insight into the formation process. First, we study the equilibrium achieved after the heat treatment of N-doped crystals (without prior irradiation), by assuming different nitrogen concentrations. It is known from the study of type Ib natural diamonds that nitrogen impurities do not aggregate when the concentration of nitrogen is below 500 ppm, unless the temperature is above 2000 K. Therefore, one can exclude the formation of N_2 and N_2V defects in a heat treatment at lower temperature. In practice, the

Defect	Q	$E^{i,q}_{form}$-qE_F
N	+	0.37
	0	3.96
	-	8.53
V	2+	5.72
	+	6.15
	0	7.14
	-	9.19
	2-	14.05
NV	+	5.31
	0	6.21
	-	8.82
	2-	13.83
N_2	+	2.55
	0	3.92
N_2V	+	4.78
	0	5.41
	-	8.64
V_2	+	9.08
	0	10.08
	-	12.42
	2-	15.59
NVH	-	4.34
	0	5.19
	-	7.59
	2-	12.19

Table 4.3: HSE06 formation energies (in electron volts) of the nitrogen- and V-related defects according to Eq. 4.7, with $\mu_N = 11.39$ eV (corresponding to the energy of a nitrogen atom in the N_2 molecule at 0 K). The formation energies of charged defects are referred to E_V (in Eq. 4.7). The chemical potential of hydrogen was set as in Ref. [187] (see text for more details).

nitrogen concentration depends on the growth conditions (temperature, pressure, and nitrogen precursors present), which determine the chemical potential of nitrogen. Here we tuned the value of μ_N (and with it the values in Table 4.3) in order to set the total concentration of nitrogen defects in the desired region between 10 and 500 ppm. We solved Eqs. 4.3-4.7 self-consistently under these conditions, assuming the formation of Ns, V, NV, and V_2 defects in a heat treatment at the example temperature of T = 1100 K.

We find that V and V_2 practically do not form because of their much too high formation energies. As shown in Fig. 4.4, the calculated $[N_s]/[NV]$ concentration ratio is constantly $\sim 10^3$ under these conditions. As a consequence, the Fermi level is pinned at $E_V + 4.0$ eV, where the vast majority of N_s are neutral (see Fig. 4.3). Thus, $\sim 0.1\%$ of the N_s defects donates an

Defect	HSE06 (LDA)	Experimental
V(0)	2.8 (2.8)	$2.3 \sim 0.3^a$
V(-)	3.5 (2.5)	Immobile^a
NV(0)	4.7 (4.8)	

Table 4.4: Diffusion activation energies. Numbers in parentheses are from the LDA calculations of Refs. [172, 174].
^{a} Reference [188]

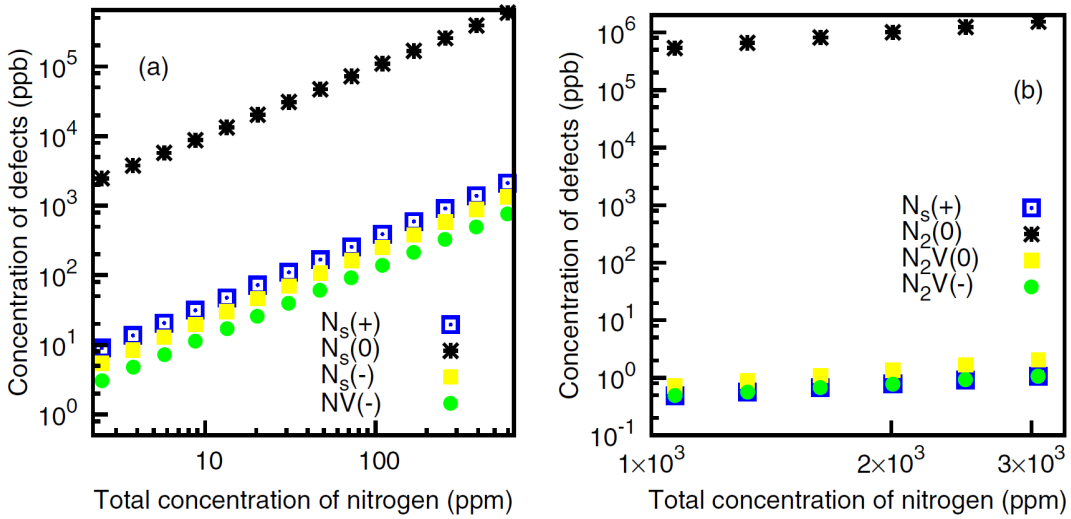

Figure 4.4: Concentration of defects. Calculated concentrations of defects characteristic in (a) Type Ib and (b) Type IaA diamonds after annealing at 1100 K. The other defects with the corresponding charge states have lower concentrations and are not shown in these plots.

electron to NV defects. As a consequence, all the NV defects will be negatively charged. All in all, our calculations indicate that NV(-) is introduced at concentrations < 1000 ppm in lightly N-doped diamond, where neutral N_s (with s = 1/2 electron spin) will donate one electron to the NV and turns to $N_s(+)$.

At the next step the higher nitrogen contents are considered between 1000 and 3000 ppm, which correspond to Type Ia natural diamonds. In this case, the average distance between nitrogen impurities is just a few lattice constants; thus, nitrogen impurities may aggregate even at a relatively low temperature such as 1100 K, and N_2 and N_2V may form under these conditions. To simulate these conditions, we tuned μ_N to set the total concentration of nitrogen defects in the desired region and considered all the defects in all charge states as listed in Table

4.3, except NVH. Our simulations indicate [Fig.4.4b] that nitrogen occurs predominantly as $N_2(0)$, while a small fraction of N_ss and N_2V ($\sim$1 ppb) can coexist. The NV concentration is negligible under these conditions. Since N_2 stays in the neutral charge state, the Fermi level is pinned near the acceptor level of N_2V (see Fig. 4.3) at ΔE_V + 3.2 eV, so the neutral charge state of that defect is slightly more abundant than the negative one.

Synthetic diamonds can also be grown by CVD, with substrate temperatures $\sim$1100 K. Here, the formation of NV is influenced by hydrogen impurities, which enter the crystal in the CVD process. According to recent experiments, NVH defects form in a ratio of 0.01-0.02 to the incorporated N_s, when the concentration of N_s is $\sim$0.5-1.2 ppm [164, 189]. The concentration of NV is below the detection limit of 0.1 ppb in these samples, which means $[NV]/[N_s] < 0.1\%$. According to the calculated formation energies (Table 4.2), the NVH complex has $\sim$1 eV lower formation energy than that of NV. This result explains why the NVH defect can out compete the NV defect in a CVD diamond. The NVH complex is stable against annealing up to 1600°C [164]. Above that temperature, NV defects can already diffuse; thus, NVH defects cannot be converted to NV by thermal annealing. So, the NV concentration in CVD samples is again insufficient for practical applications.

In practice, the concentration of NV(-) centers can be increased by irradiation and subsequent annealing. The irradiation creates Frenkel pairs and other damage in the diamond lattice. Annealing leads to recombination, but some of the Frenkel pairs may split to produce isolated vacancies and self interstitials with concentrations much above that of thermal equilibrium. The self interstitials are mobile even at room temperature; they will aggregate to the surface or grain boundaries or form platelet like defects. In the meantime, they can assist nitrogen diffusion and aggregation. Subsequent to irradiation, a heat treatment has to be applied to anneal out luminescence-quenching parasitic defects. This is usually done slightly above 600 °C, where neutral vacancies become mobile. It is usually assumed that NV centers are formed during this heat treatment when vacancies get trapped at N_s defects. However, vacancies may also get trapped at existing N_2 defects or can form divacancies. The post irradiation annealing can be regarded as a quasi equilibrium process, and an insight into the creation of NV(-) centers can be gained by close inspection of the formation energies and occupation levels of the considered defects. First, one can assume that the initial concentration of isolated N_s defects is high enough

to pin the Fermi level initially above midgap. In order to have mobile, i.e. neutral vacancies after the irradiation, the Fermi level must be lowered drastically, below the single acceptor level of V ($\sim$ E_V + 2.0 eV). Thus, if NV defects are to be created by irradiation and annealing, the V concentration should be in excess of the N_s concentration ([V] > [N_s]), even after the trivial recombination with interstitials. Then, two basic reactions can occur:

$$V(0) + V(0) \rightarrow V_2(0) + 4.2eV \tag{4.8}$$

and

$$V(0) + N_s(+) \rightarrow NV(0) + h + 3.3eV, \tag{4.9}$$

where h is a hole with energy corresponding to the given Fermi-level position. Both reactions are strongly exothermic, as can be derived from the data in Table 4.3. Since [V] > [N_s] and Eq. 4.8 provides a higher energy gain than Eq. 4.9, the majority of the vacancies will form divacancies; only a small fraction creates NV defects. Since the formation of V_2 is $\sim$ 0.9 eV more favorable than that of NV, the equilibrium concentration of V_2 will be several orders of magnitude larger than that of NV, even at relatively high temperatures (at 1100 K by a factor of 2×10^4). This implies that the concentration of NV defects, arising through the reaction in Eq. 4.9, will not be significantly higher than they would be without irradiation. In addition, the generally assumed process of creating NV defects by V diffusion would be self-limiting. As isolated vacancies start to form V_2 and NV defects, the Fermi level shifts up, because both V_2 and NV are deeper acceptors than V (Fig. 4.3). As a result, the remaining isolated vacancies will become negatively charged and immobilized. **So increasing the V concentration cannot help to increase [NV].**

The observed increase in [NV] can, therefore, be explained only by assuming that NV defects dominantly form during irradiation, not during the annealing. Our results support this assumption. With the data of table 4.3, the creation of a V near N_s requires an energy of

$$N_s(0) + 2.26eV \rightarrow NV(0) + C \tag{4.10}$$

while that of a V in a perfect part of the crystal needs,

$$perfect - lattice = 7.14eV + V(0) + C \tag{4.11}$$

where C is a carbon atom in the perfect diamond lattice. The reason for the difference is that to remove the C atom opposite to N_s requires breaking only three strong C-C bonds , whereas four such bonds have to be broken in the perfect diamond lattice to form an isolated V. Such a big energy difference should lead to a strong preference for NV creation even in the nonequilibrium process of irradiation, explaining most of the arising NV concentration. **Therefore, the dominant part of the NV concentration is created directly by the irradiation**.

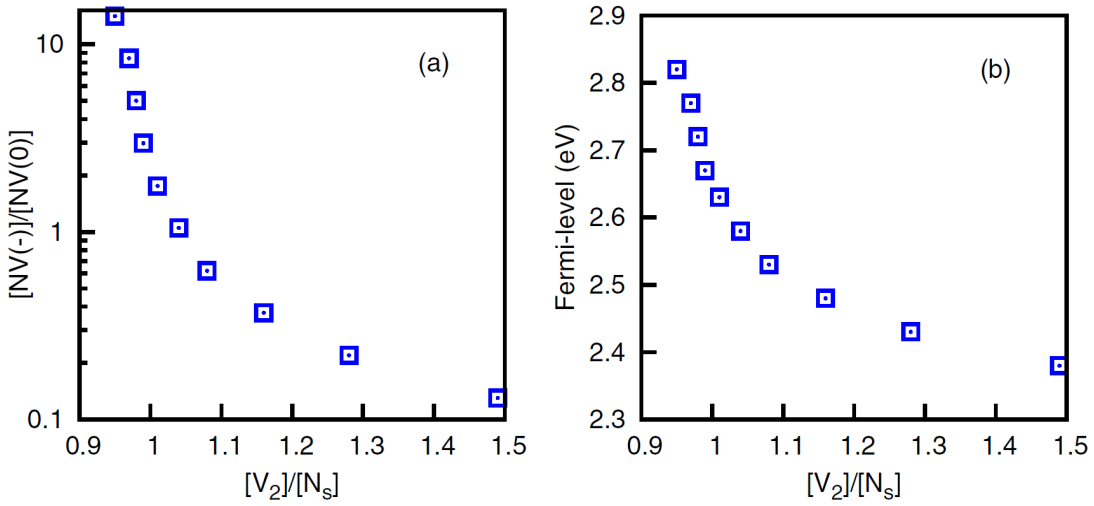

Figure 4.5: NV(-) to NV(0) ratio. (a) The calculated concentration ratio [NV()]/[NV(0)] and (b) the corresponding Fermi-level position (with respect to E_V) as a function of the ratio of $[V_2]/[N_s]$ at T = 1100 K. The total concentration of nitrogen is set to ∼386 ppm, while the Ns-to-NV conversion factor is 1.4 percent.

According to our simplified model, the dominant point defects in N-doped, irradiated, and annealed diamond samples are N_s, NV, and V_2. The charge state of the NV defect will depend on the relative concentrations of the N_s donors and the V_2 acceptors. To study the chances for creating negatively charged NV centers, we have tuned the formation energies of these three defects to obtain a total nitrogen concentration of 386 ppm and an N_s-to-NV conversion factor

of 1.4% (i.e., within the range of experimental observations between 0.5 and 2.5%), at various $[V_2]/[N_s]$ ratios. Figure 4.5 shows how the [NV(-)]/[NV(0)] ratio depends on $[V_2]/[N_s]$.

If divacancies dominate, i.e., $[V_2]/[N_s] > 1$, then the Fermi level will be pinned near the single acceptor level of V_2 at E_V +2.3 eV. Since the first acceptor level of NV is at E_V + 2.7 eV, our simulation results in an [NV(-)]/[NV(0)] concentration ratio of ∼0.1. Therefore, for $[V_2] > [N_s]$ the neutral NV would dominate. Reducing $[V_2]$ will shift the Fermi level toward the acceptor level of NV and, as soon as $[V_2]/[N_s] < 1$, the negative charge state of NV becomes dominant. Our simulation demonstrates (Fig. 4.5) that the charge state of NV is very sensitive to the concentration of V_2 in this range. Changing the concentration of V_2 by less than a factor of two, can change the [NV(-)]/[NV(0)] ratio by a factor of ∼100.

These results show that the postirradiation annealing not only does not contribute significantly to the NV production but also, by creating divacancies, may prevent the achievement of negatively charged NV defects. The annealing is unavoidable, but our analysis indicates that its temperature should be chosen in the range where V_2 becomes mobile while NV does not. Here a possible way of optimizing the concentration of the required negatively charged defect is predicted which has been very quickly confirmed experimentally by one of the leading groups in the field ([190]).

The annihilation of the divacancies may occur by out diffusion but also by recombination at interstitial clusters or by the formation of V aggregates, which are also electrically active [191–193]. However, it appears likely that the V aggregates are acceptor defects, with a charge transition level ∼E_V + 3.5 eV [164]. This is well above the (0/-) level of NV, so they can donate electrons to turn NV(0) to NV(-). Thus, elimination of V_2 can stabilize the charge state of NV(-).

Our analysis is in line with the observed higher efficiency of NV(-) creation, when annealing irradiated diamonds at higher than usual temperatures (1100-1200 °C) [170]. The annihilation of V_2 is important even when $[NV(-)]/[NV(0)] > 1$ happens to be the case after irradiation and annealing, because V_2 will be negatively charged under this condition and can compromise the photostability of NV(-). High-temperature postannealing treatments could help stabilize the charge state of NV(-) [194]. Our results highlight the need for careful characterization of

irradiated and annealed diamond samples, particularly focusing on V_2 or larger V aggregates [195], and the need for more detailed studies of the annealing temperature.

4.5 Conclusion of the NV formation study

I calculated the charge transition levels, barrier energy for migration, and reaction energies of basic V- and nitrogen-related defects by the HSE06 supercell plane wave method. I have reproduced the known experimental data regarding electronic transitions, substantially improving over previous (standard) DFT calculations. In particular, without any a *posteriori* correction, our HSE06 calculation reproduces all experimentally observed charge transition levels. The proven accuracy of the method has allowed me to predict missing data on the charge transitions of all the investigated defects (N_s, V, NV, NVH, N_2, N_2V, and V_2), which are crucial for establishing the charge state of different defects. My results also comply with the experimental finding on the migration of isolated V, i.e., that only its neutral form is mobile, while it is immobile in its negative charge state.

By assuming quasiequilibrium conditions, the NV center may be created in lightly N-doped diamond ([N] $<$ 500 ppm) in small concentration, whereas the formation of N_2V defects is more likely for high concentrations ([N] $>$ 1000 ppm). The basic reaction for the formation of NV centers in irradiated and annealed samples was also investigated. The key findings are that: I) Irradiation is more likely to directly create NV defects than vacancies. II) In postirradiation annealing, much more divacancies are formed than NV defects, and only short-range diffusion of vacancies proximate to N_s defects can increase the concentration of NV centers. III) Since V_2 is a deeper acceptor, the created NV defects will dominantly be in the neutral charge state, unless the concentration of divacancies is sufficiently decreased by annealing above $\sim$ 1100 K.

Chapter 5

Luminescence of the Near-Surface NV Centers in Diamond

5.1 Introduction

As the quantum-optics protocols of the nitrogen-vacancy (NV) center rely on its negative charge state in diamond, the control of the charge state of the NV center [42, 72, 81, 196] is a prerequisite to apply them in sensor applications [39–41, 161, 197–201] or for quantum computing [202–206] where NV centers should be placed as close as possible to the surface of diamond for efficient sensing of the targeted nano-objects. NV centers used in biolabeling are usually close to the surface, because of the small size of the hosting nanodiamond. Advanced technologies have made it possible to implant NV centers < 1 nm in depth from the surface [207] in a controlled fashion, and luminescent ultrasmall $\sim$5 nm nanodiamonds could be also fabricated [53] where NV centers are naturally located very close to the nanodiamond surface. It has been recently found that NV(-) centers engineered in the range of $5 - 200$ nm below the surface of hydrogenated diamond tend to lose their charge and NV(0) dominantly appears [72, 81, 196], which is caused by a surface band-bending effect (see Fig. 5.1) [208].

Previous experiments have shown [209] that the electron affinity, χ, is negative ($\chi = -1.3 \pm 0.1$ eV) for hydrogenated while positive for oxygenated diamonds, where its actual value depends on the oxygen coverage and the type of oxidation. The largest positive electron affinity (PEA), $\chi = +2.56$ eV for diamond was measured on the fluorinated (001) surface [210]. As a consequence

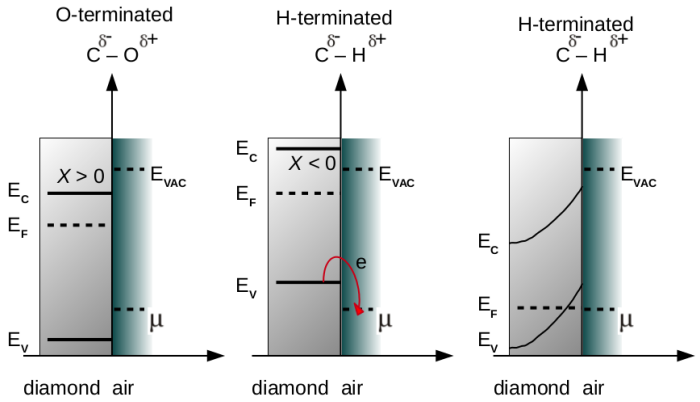

Figure 5.1: Energy-band scheme of diamond. (a) O-terminated diamond: The conduction band E_C lies below the vacuum level E_{VAC} (electron affinity $\chi > 0$ eV). The NV- level lies beneath the Fermi level E_F , where the position is mainly determined by the bulk concentration of nitrogen. (b) H-terminated diamond: The bands are shifted upward by the hydrogen termination ($\chi < 0$ eV). Electrons can transfer into acceptor states μ of an adsorbed water layer. Surface band-bending in H-terminated surfaces results in surface conductivity. [77, 196].

of the negative electron affinity (NEA), the conduction and valence bands of hydrogenated diamond bend upward at the surface at ambient conditions, so, except for heavy n-type doping, the Fermi-level will shift below the acceptor level of the NV-defect, and NV(0) will dominantly appear [72]. Oxidation removes this bending, and luminescent NV(-) defects also appear beside NV(0) [72, 81]. In fluorinated surface diamonds further enhancement of the luminescent NV(-) to NV(0) ratio was observed [27]. This band-bending model was applied to explain the enhanced NV(-) to NV(0) ratio in larger nanodiamonds after oxygenation [42], however, we note that it does not explain all the features of the NV center near the diamond surface. For instance, intermittency in fluorescence, i.e. blinking, was detected in nanodiamonds of 5 nm in diameter [53] where the concept of solid state bands is strictly not valid any more, so acceptor states should play a role in this process [211]. In a recent study, 30% of the NV$(-)$ centers engineered $5-2$ nm beneath the F-terminated diamond surface showed permanent bleaching. [212] Since F-termination of diamond leads to a PEA surface [210], a band-bending model cannot account for such a bleaching behavior of the NV(-) defects. Blinking or bleaching is detrimental for NV-based nanoscale sensing based on the intrinsic ODMR signal of the NV-defect, so it is of immediate and high interest to explore the properties of the diamond surfaces, in order to be

able to harness the unique properties of NV-centers.

In this chapter I investigate the interaction of surface related states with the defect states of the NV(-) for various surface terminations [3].

5.2 Slab calculations

I fixed the optimized lattice constants to build-up the (001) slab models. The periodic Primitive cell of the slab model the x-y plane of was chosen to be $(\sqrt{2}\times\sqrt{2})R45°$. Because of the very time demanding calculations I applied of about 2.2 nm in thickness slab models and 1.2 nm vacuum layer along the z-direction in order to avoid direct interaction between the periodic images of the slab.. The slab models with different surface terminations were first optimized using a 8×8×1 MP k-point set while the C-atoms in the middle double layer were fixed at their bulk positions. The atoms were allowed to relax until the forces were below 0.01 eV/$\mathring{A}$.

After obtaining the unit cells of the slab models a (4×4) supercell from primitive cell containing 352 C-atoms is constructed and then, a $2 \times 2 \times 1$ Γ-centered k-point mesh in the Brillouin zone sample is applied.

Into the slab models with various surface ligands I have introduced the NV defect in the middle double layer of the slab. Then, I allowed the system to fully relax except all terminators and a double layer of carbon atoms connected to the slab. These atoms were fixed at their defect-free slab coordinates. Equilibrium geometry obtained by PBE in the generalized Kohn-Sham theory [213] in the screened hybrid functional HSE06 of Heyd, Ernzerhof and Scuseria with the original parameters ($0.2\mathring{A}^{-1}$ for screening and 25% mixing) [178, 214].

5.3 Surface termination

Different surface terminations to eliminate all the dangling bonds of the carbon atoms, identically on both the bottom and top layers, is introduced. This construction eliminates the need for any dipole correction. The effect of the artificial quantum confinement due to the finite slab model on the calculated defect electronic structure is ~ 0.07 eV.

The distance between the periodic images of the NV defect is ~ 0.9 nm along the (100) and (010) directions. The negative charge of the NV defect is donated by a substitutional nitrogen

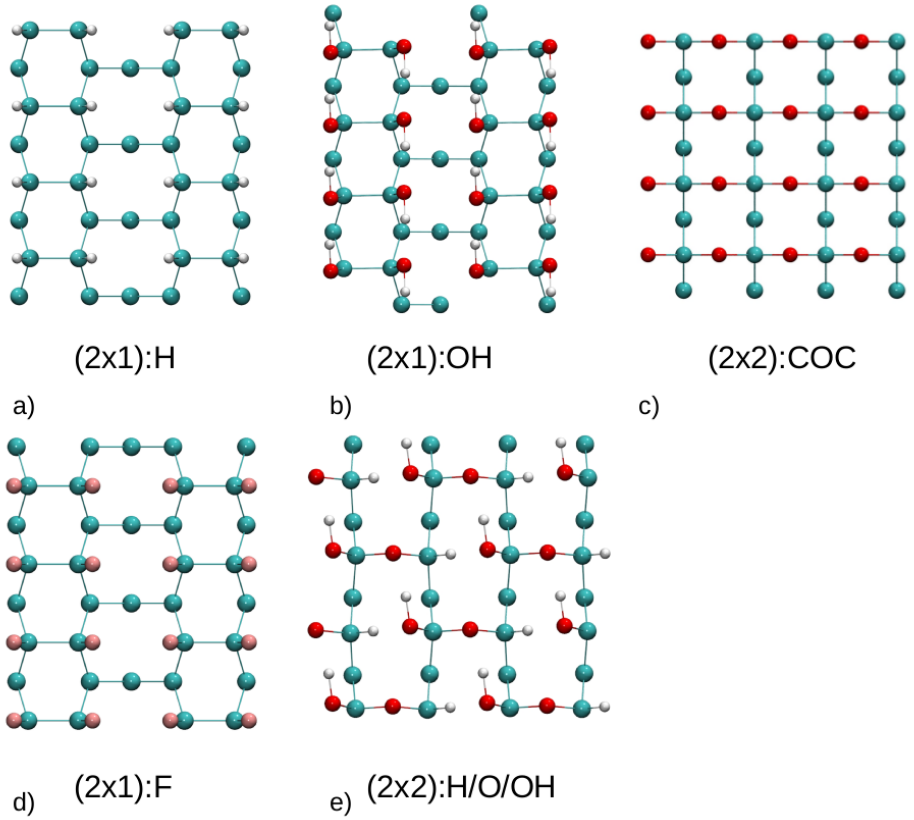

Figure 5.2: Top view of the different surface terminations considered in this work.

(N_s) defect which is placed by about 0.7 nm from the NV defect, at the same depth from the top carbon layer. This construction avoids the creation of an artificial dipole interaction across the layers of the diamond slab, whereas the dipole-dipole interaction due to the negatively charged NV defect and the positively charged N_s defect within the same layer is canceled.

The estimated maximum uncertainty for the position of the defect state within the bandgap induced by the slab model is 0.2 eV which still suffices to categorize the different (001) diamond surfaces from the aspect of the charge control of NV defects proximate to the surface. The (001) diamond surface, seeking for the best termination for nanoscale sensing with the NV-center close to this diamond surface is investigated in this study. My typified surface models are "ideal" in the sense that they are atomically smooth and do not contain any trivial defects, as e.g. dangling bonds. This approach aims to focus on the effect of various terminators. The (001) diamond surface reconstructs to (2×1) under ambient conditions. This leads to long carbon-carbon bonds (C-C bridges) at the surface, reducing the number of dangling bonds per surface C atom from two to one. With the remaining dangling bonds saturated by hydrogen atoms, one obtains the (2×1):H diamond surface (see Fig. 5.2a). After oxidation, hydroxyl (-OH) groups may replace H-terminators. This is a typical termination of nanodiamonds in biological environment. These -OH groups are placed relative to each other into the energetically most favorable configuration (see Fig. 5.2b) [215]. A planar array of "closely packed" ether-like groups (C-O-C bridges with oxygen inserted between any two carbon atoms on the surface, after removing H or OH terminators [215]) are also considered as a simplified model to study the role of C-O-C bridges (see Fig. 5.2c) in making a PEA diamond surface [209, 216]. The (2×1):F (001) diamond surface (see Fig. 5.2d), which is very similar to the (2×1):H surface, but hydrogen atoms are replaced by strongly electro-negative fluorine atoms is also studied. We also consider a partially oxidized model surface, allowing for alternating termination with -H and -OH groups as well as ether-like C-O-C bridges. I call this surface type as H/O/OH termination (see Fig. 5.2e). I investigate both NV(0) and NV(-) defects near these diamond surfaces.

5.3.1 Hydrogen termination

Slab calculations with vacuum allowed us to calculate the electron affinity (EA) of the considered diamond surfaces. For calculating this parameter, first the average potential in the direction

perpendicular to the surface is calculated. Next, The bulk-like occupied (VBM) and unoccupied (CBM) (see .5.3a) bands by plotting the charge density of the bands are identified. Finally, I obtained the electron-affinity of the system as the energy difference of the vacuum level and the calculated conduction band minimum. The electron affinity for the hydrogen terminated surface is calculated to be χ = -1.7 eV (see Fig. 5.3a), in fairly good agreement with the experimental value (-1.90 eV)[209]. By looking at the electronic structure I find that the hydrogen termination introduces deep, sub-bandgap states that are surface-related (see Fig. 5.3b and c).

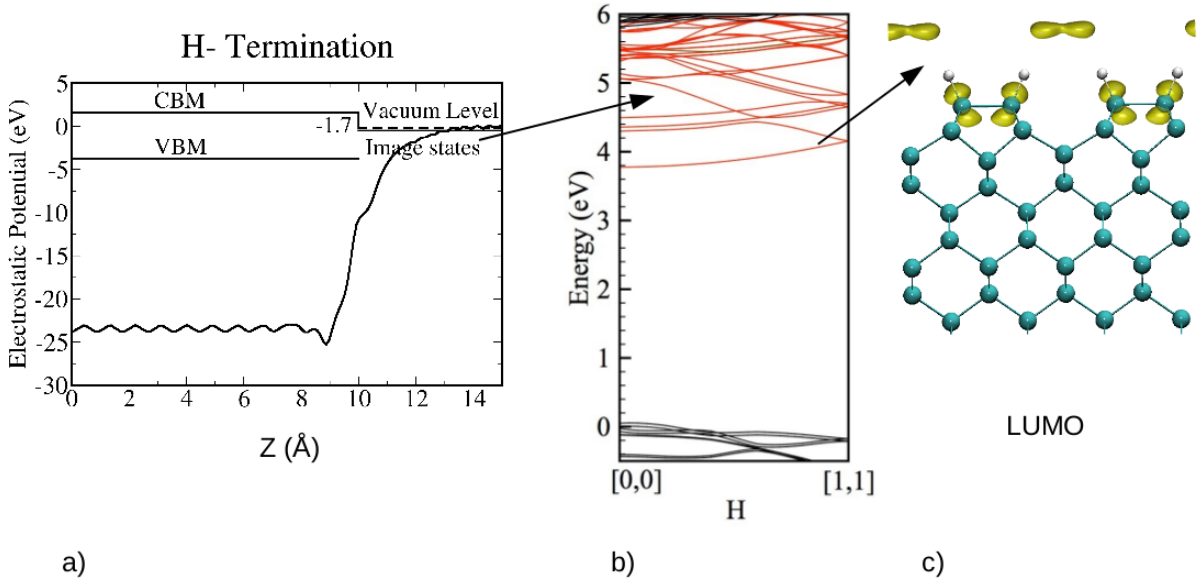

Figure 5.3: a) the calculated average potential vs. the z coordinate is plotted, where the z coordinate is the direction perpendicular to the surface. z=0.0$\mathring{A}$ corresponds to the middle of the slab. The electron-affinity is given in eV unit. b) The calculated HSE06 band structure of the (001) diamond H-terminationed surface along (110) direction in the Brillouin zone. The results are shown for slab supercells, thus band folding appears in the band structure. Red colour represents image states. c) The corresponding charge density isosurface of the surface related states are depicted on the structures. (The NV defect is located at the middle of each structure which is not shown in the figures). Charge density isosurface is depicted at isovalue of 0.0029 e/Å^3.

These so-called image states are delocalized along the surface and show strong dispersion. Image states are known at other insulator surfaces with NEA [217]. As mentioned earlier, NEA can make NV defects neutral due to band-bending, however, this does not necessarily happen above a certain level of n-type doping [207]. Thus, both NV(0) (see Fig. 5.4a) and NV(-)

(Fig. 5.4b) are considered at this surface. I find that the unoccupied defect level of NV(-), which is responsible for the spin-conserving absorption and luminescence [9], mixes with the surface image states (Fig. 5.5). Since the image states are delocalized along the surface, any excitation of NV(-) will lead to a temporary or permanent loss of the excited electron, since these delocalized states are responsible for the electron emission from a NEA surface. In other words, photo-excitation causes either fluorescence intermittency (blinking) or bleaching due to ionization of the defect (see Figure 5.13a). This is a very distinct process from the band-bending model which is usually invoked to explain the relative stability of the charge states in thermal equilibrium.

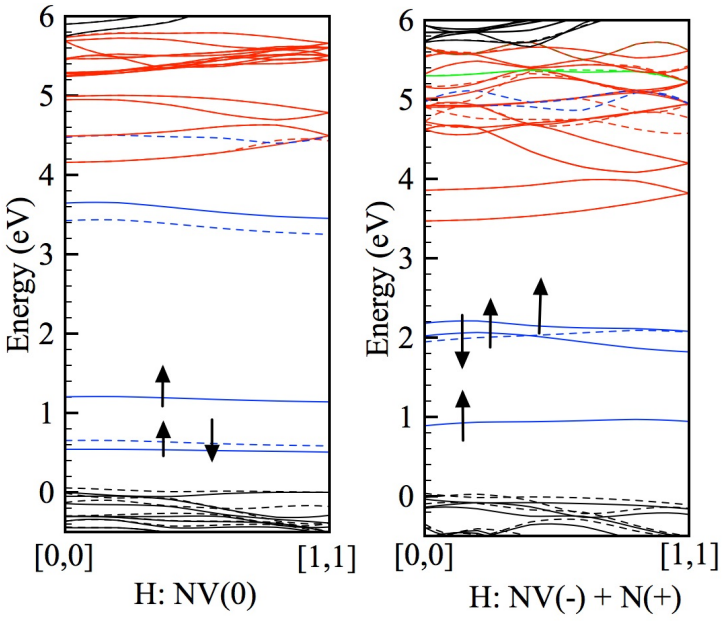

Figure 5.4: The band structure of the NV defects in the (001) diamond slab with the hydrogen termination. Right hand side NV(0) and on the left side NV(-)+ Ns(+). Color coding of the bands: black, blue, red and green lines correspond to bulk-like, NV, image and Ns states, respectively. The majority spin-up and minority spin-down bands are depicted by straight and dashed lines. The occupation of defect bands are shown by arrows. The spin-up and spin-down bands are depicted by straight and dashed lines. The occupation of defect bands are shown by arrows. The [1,1] k-point corresponds to the X point in the Brillouin zone of diamond lattice.

The defect levels of NV(0) lie much deeper than those of NV(-) [218]. NV(0) may not be directly ionized due to the image states upon the usual green light excitation (532 nm, i.e., 2.35

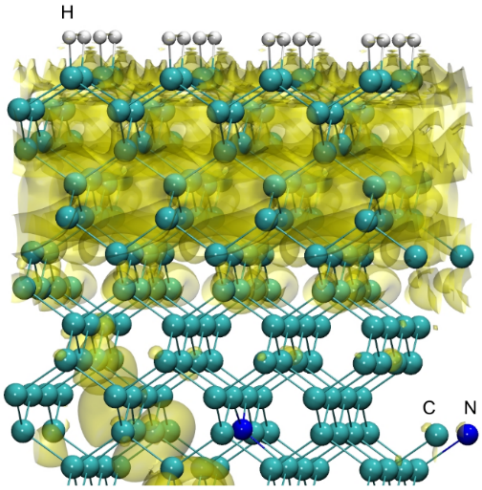

Figure 5.5: Nitrogen-vacancy (NV) defect at close proximity to the (2×1):H (001) diamond surface. The charge density of the state corresponding to the crossing point of the e state with an image state band (plot with an isovalue of 1.61 ×105 e/Å^3).

eV).

I conclude that, a hydrogenated surface is not suitable for sensing based on the NV(-) defect, not even under highly n-type doped conditions.

5.3.2 Hydroxyl termination

Oxygenation of the diamond surface does not necessarily lead to PEA. A (001) diamond surface fully terminated by hydroxyl groups, i.e. (2×1):OH, still gives rise to a slight NEA, with χ=-0.6 eV (see Fig. 5.6), again with surface related image states in the bandgap.

Because of the smaller NEA, these surface bands lie at energies higher ∼1.2 eV than those of the (2×1):H surface. The empty e defect state of the NV(-) defect crosses the surface bands (see Fig. 5.7). The unoccupied defect level of NV(-) mixes with the surface image states, and may cause the permanent loss of luminescence after a single photon absorption.

5.3.3 Ether termination

Oxygenation of the (001) diamond surface leads to PEA when ether-like C-O-C bridges appear [209, 216]. A full termination with such ether-like groups, the (2×1):O surface results in χ =

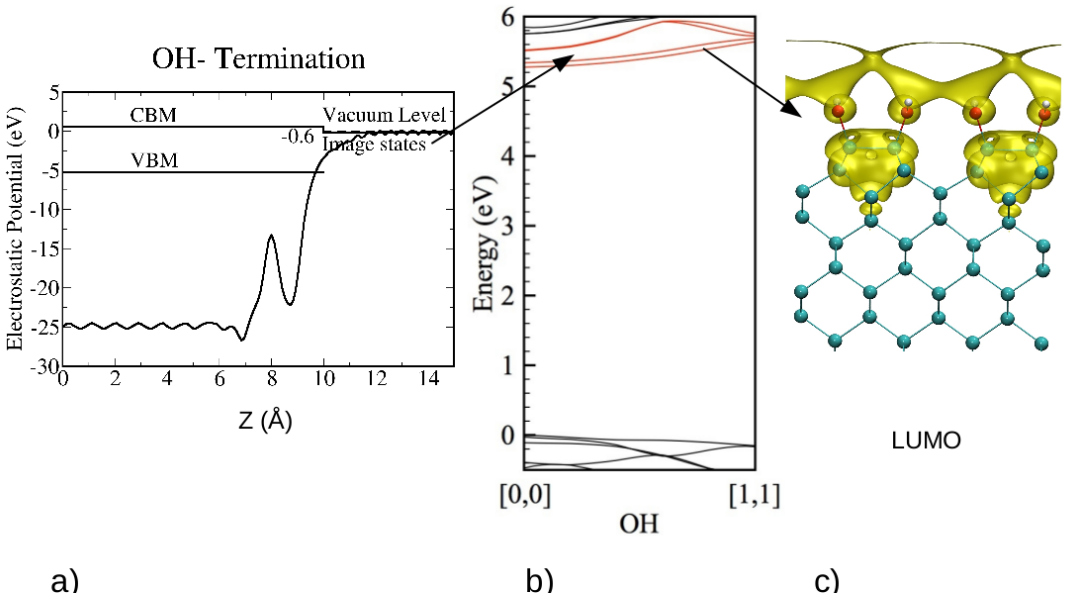

Figure 5.6: a) The calculated-electron affinity of the (001) diamond slab with HSE06 functional. The z coordinate is the direction perpendicular to the surface. $z = 0.0\mathring{A}$ corresponds to the middle of the slab. The electron-affinity is given in eV unit. b) The calculated HSE06 band structure of the (001) diamond OH-terminationed surface along (110) direction in the Brillouin zone. The results are shown for slab supercells, thus band folding appears in the band structure. Red colour represents image states. c) The corresponding charge density isosurface of the surface related states are depicted on the structures. (The NV defect is located at the middle of each structure which is not shown in the figures). Charge density isosurface is depicted at isovalue of 0.0014 e/Å^3.

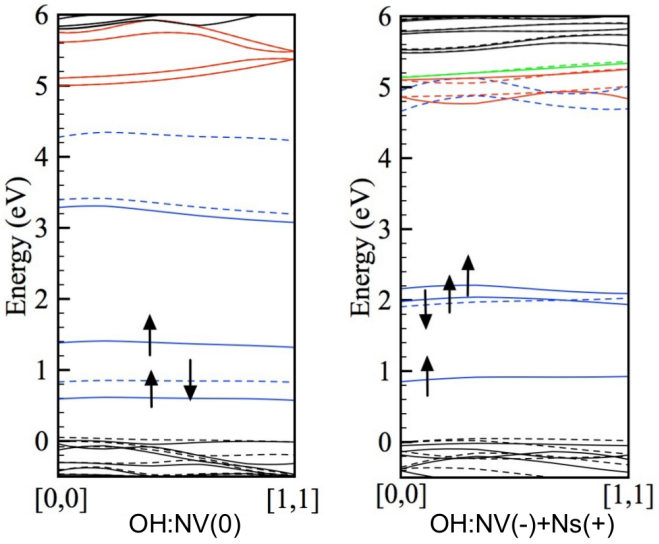

Figure 5.7: The calculated HSE06 band structure of the (001) diamond surface terminations along (110) direction in the Brillouin zone for a) NV(0) and b) NV(-)+ Ns (+). Color coding of the bands: black, blue, red and green lines correspond to bulk-like, NV, image and Ns states, respectively.

+2.40 eV, see Fig. 5.8, which is close to the value found experimentally after prolonged oxidation of the (001) diamond surface [219].

I emphasize that full termination with ether-like groups on an atomically smooth surface is not likely. Experiments show loss of periodicity and surface roughening after long-term oxidation [219]. However, the interaction between closely packed C-O-C units can be well studied in a two-dimensional periodic model with an atomically smooth surface. At such a high concentration of ether-units, surface related occupied bands appear above the valence band edge and unoccupied bands deep below the conduction band edge. The deep sub-bandgap occupied bands appear due to the interaction of the oxygen lone pairs. The steric repulsion of these states will push up the energies of these lone pair states see Fig. 5.9c. The nature of the sub-bandgap unoccupied bands can be understood by the nature of ether (C-O-C) bridges; the closely packed C-O-C units forces the surface carbon atoms toward the bulk diamond in order to arrive at the usual C-O-C angle characteristic for this ether configuration. Thus, the surface carbon atoms significantly move out from the ideal sp^3 bonding configuration, and p orbitals appear pointing perpendicular to the plane of the C-O-C unit. The interaction of these empty p orbitals form the deep unoccupied bands below the conduction band edge (see Fig. 5.9b).

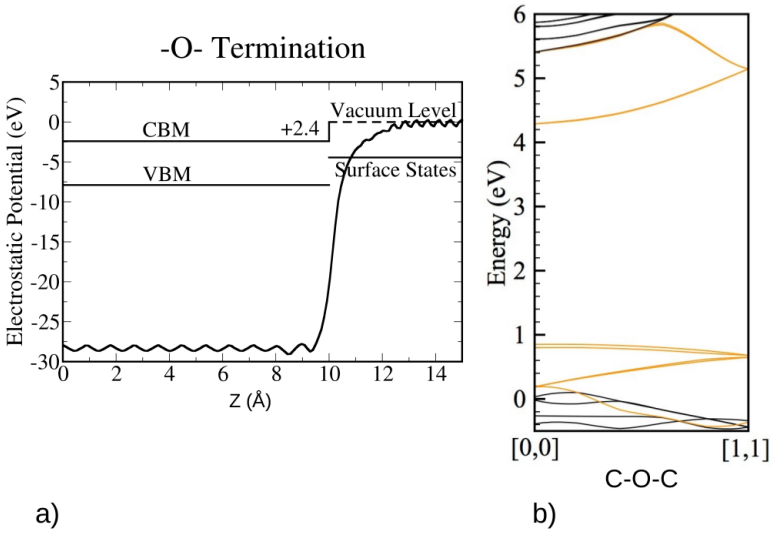

Figure 5.8: The calculated HSE06 band structure of the (001) diamond surface ether terminations along (110) direction in the Brillouin zone. The results are shown for slab supercells, thus band folding appears in the band structure. The surface related bands are colored. Orange represents localized states.

The empty defect states of NV(-) mix with these unoccupied surface states. So, even single photon absorption may lead to intermittency in the fluorescence of NV(-) in this case, because the excited electron may be trapped by the ether terminated surface. Because of the PEA, this surface is not an electron emitter, and direct photoionization may not occur. The surface bands act as shelving states, and the electron may travel back to the NV defect with some probability, giving rise to phosphorescence (see Fig. 5.13c). So, the presence of the surface bands can cause blinking when high-power laser excitation is applied in order to address single NV-centers beneath the diamond surface. In this case, two-photon absorption occurs which will again trap the high energy electron in the surface related bands. The probability of such a process is increasing with the excitation power. Indeed, such phenomena has been recently reported in relatively small oxygenated nanodiamonds [220].

5.3.4 H/O/OH termination

Based on what I have learned on the effect of full H, OH or ether terminations finally, I consider a novel arrangement with a mixed termination of the (001) diamond surface with -H and -OH

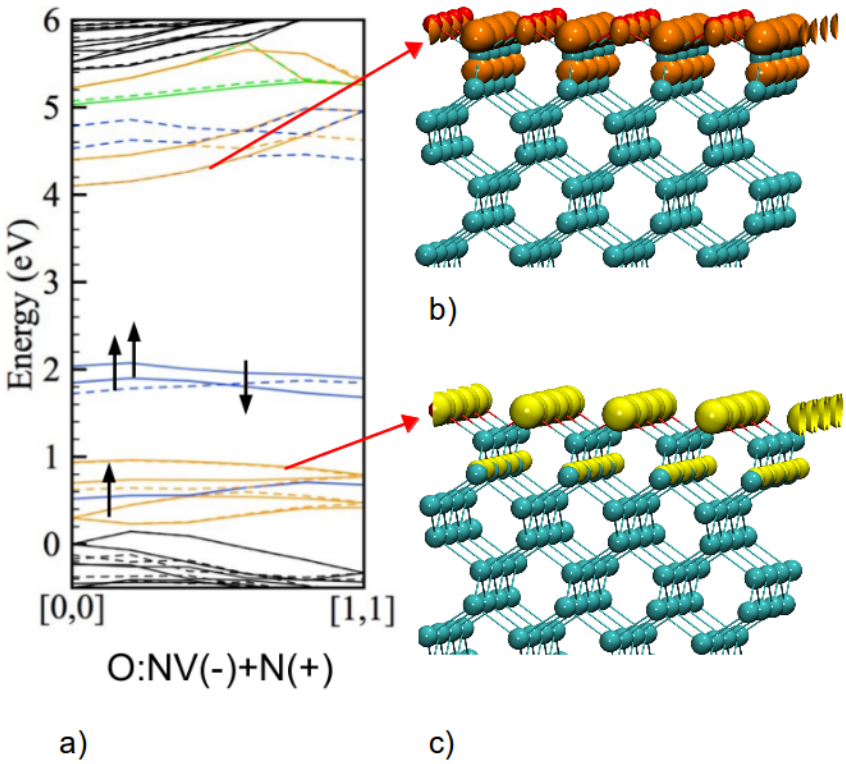

Figure 5.9: The calculated band structure of the NV defects in the (001) diamond slab and the charge density of the wavefunctions. a) Color coding of the bands: black, blue, yellow and green lines correspond to bulk-like, NV, localized surface and Ns states, respectively. The majority spin-up and minority spin-down bands are depicted by straight and dashed lines, respectively. The occupation of defect bands are shown by arrows. The isovalue of the charge density is 0.0048. b), The highest occupied defect band (HOMO) is shown by yellow lobes on ether-like terminated surface. c), The lowest unoccupied defect band (LUMO) is shown by orange lobes on ether-like terminated surface.)

groups and C-O-C bridges. Within our two-dimensional periodic model I arrange them to avoid next neighbor C-O-C bridges either in a chain or parallel to each other. The resulting surface can be described as (2×2):H/O/OH (Figure 5.10). (Note that my model differs from that of a previous theoretical study where next neighbor C-O-C bridges are lined up parallel to each other [77])

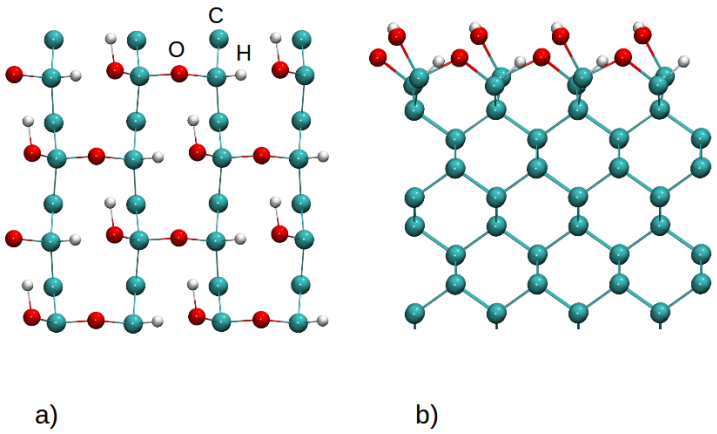

Figure 5.10: The (2×2):H/O/OH model surface, with no surface related states in the bandgap. It is proposed as an ideal model to host the NV(-) defect.

This zigzag arrangement may be the most realistic, still atomically smooth and periodic model of a disordered, partially oxygenated (001) diamond surface. The steric repulsion acting on the 2p states of the oxygen atoms is minimized, and the ether-like bridge can take on a natural geometry, without distorting the sp^3-bonding configuration of the surface carbon atoms. As a consequence the band of oxygen lone pairs is below the valence band edge, and no acceptor-like state appear near the conduction band. Our model results in a clear gap and a PEA of $\chi = +0.50$ eV, and no surface acceptors (see Fig. 5.11).

Similar combination of surface terminators may be formed in the early stage of thermal oxidation of hydrogenated diamond [219]. I note that oxygenated diamond surfaces with such an electron affinity have been observed [219].

The calculated defect levels of NV(0) and NV(-) resemble the calculated defect levels in bulk diamond 5.12. Since this surface type has PEA, no extra doping is needed to stabilize the negative charge state, and no sub-bandgap states interfere with the ODMR signal of NV(-).

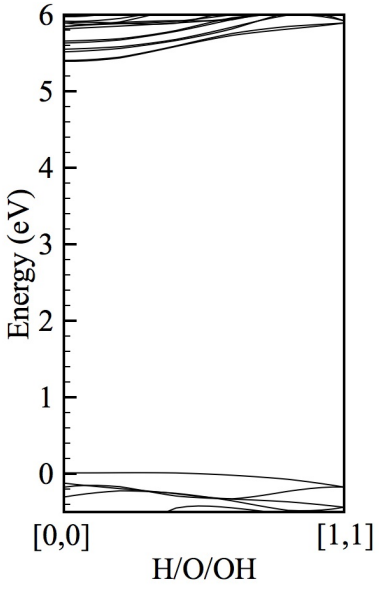

Figure 5.11: The calculated HSE06 band structure of the (001) diamond surface terminations along the (110) direction in the Brillouin zone.

Thus, I identified a combination of surface terminators on the (001) diamond surface which is ideal for NV-based nano-sensing.

I emphasize that this is not the consequence of the ordered surface. In fact, beside the positive electron affinity, it is the disorder in the distribution of ether-like C-O-C bridges which is important. Replacing a pair of nearby H and OH terminators by an O bridge in our ideal model, brings back the occupied surface states near the VBM, due the steric interaction of the oxygen lone pairs of three stacked bridges in parallel. The arising occupied surface states are about half as deep as in the case of the fully oxygenated surface. The unoccupied surface states, due to the frustrated bonding configuration of the two middle carbon atoms of the arising three ether-like bridges in a row, also reappear but are very shallow.

This shows that a small excess of oxygen bridges with respect to H and OH terminators is still tolerable. Increasing oxygen excess, however, can cause more stacking of O-bridges and deeper states which can interfer with the NV luminescence. Removal of two oxygen atoms, to create an H-C-C-H configuration out of an H-C-O-C-OH unit, on the ideal H/O/OH terminated surface leads to the reappearance of image states, about 0.2 eV below the CBM. Since the final

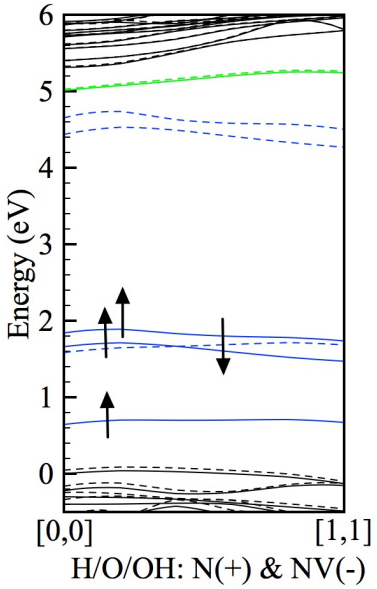

Figure 5.12: The calculated HSE06 band structure of the (001) diamond surface termination along the (110) direction in the Brillouin zone. The NV(-) defect is placed in the middle of the surface.

state of the excitation of the NV(-) centers are about 0.6 eV below the CBM, this might be tolerable, but increasing H-excess will lead to increasing the NEA and deepen the image states. So I may conclude that the ideal surface termination should contain oxygen bridges "diluted" among H- or OH-terminated sites, and the H/O ration should be about 1.0 ± 0.2. Such surfaces can probably be created by gentle thermal oxidation of a hydrogenated surface, or by oxidation with an acid.

Beside direct photoionization, an additional mechanism can take place in the excitation process. In confocal microscope setups, applied for NV-based sensing, the NV(-) is excited with a high density of photons which leads to two-photon absorption via its real excited state, so the electron will be promoted into the conduction band with rather high probability [218]. After an Auger process, the NV(-) defect converts temporarily to NV(0), but can be rapidly reionized to NV(-) after appropriate photo-excitation [218]. Typically, continuous green light excitation (532 nm) suffices to drive this process. This process is an intrinsic property of the NV defect, and occurs in ultra pure bulk diamond [218]. Now, the presence of delocalized surface acceptor states with energies close to or slightly above those of the defect levels can seriously alter the

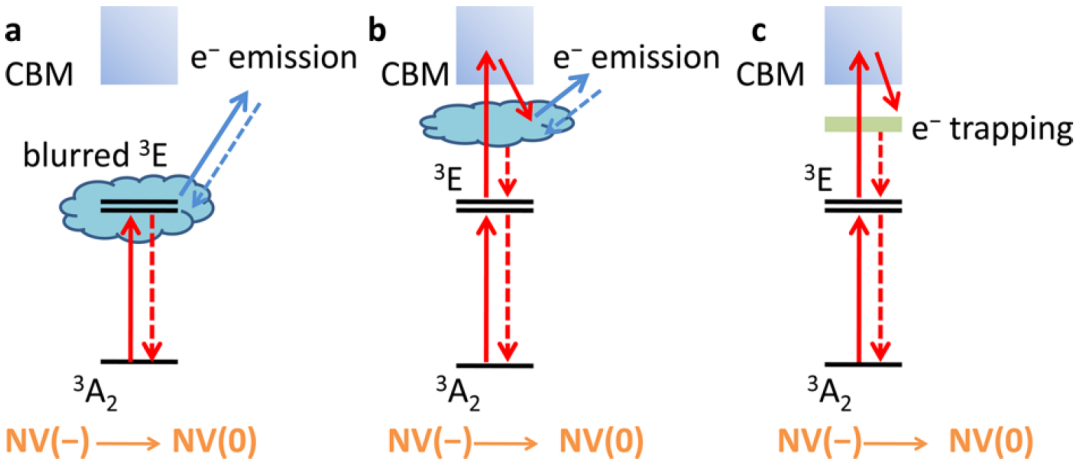

Figure 5.13: Photoexcitation and decay processes at the nitrogen-vacancy (NV) center in close proximity to the (001) diamond surface. (a) Direct photoionization via photoexcitation to a mixed excited state consisting of the defect state and the image state (blurred 3E) from the ground state ($^3A_2$) which emits the electron from the surface due to the negative electron affinity. An electron may be scattered back to the excited state with low probability, leading to luminescence i.e. intermittency in fluorescence may also occur (blinking). (b) After two photon absorption via the real excited state, the electron scatters to the image state which emits the electron from the surface; backscattering to the excited state and luminescence has a low probability. (c) After two photon absorption via the real excited state, the electron scatters to a localized surface state in the gap where the electron is trapped; after some time it relaxes to the excited state and luminesces (phosphorescence); the probability of this blinking is high at the surfaces with positive electron affinity.

aforementioned process. The photoexcited electrons from the close-to-surface NV defects can scatter into the acceptor image state. In the case of a NEA diamond surface, this electron can leave the material with high probability (see Figure 5.13b) and can bleach NV(-). Thus, full hydroxyl termination is definitely not preferred for NV-based sensing.

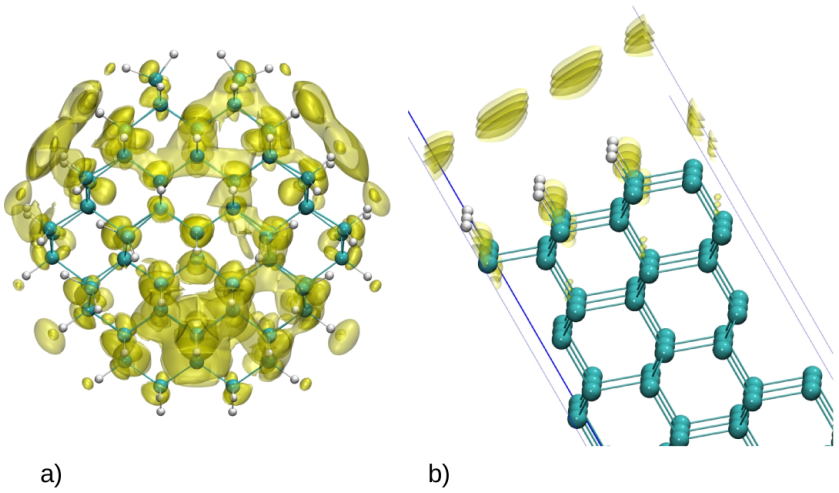

Figure 5.14: The lowest unoccupied states in small nanodiamonds of about 1.5 nm in diameter with H-terminations (charge density isovalues of 3×10^5) demonstrating that the quantum confinement does not remove the low-energy image states.

The analyse was in the slab but picture 5.14a and b propose the same things happen in the nanodiamonds. Therefore, the blinking and bleaching in nanodiamonds which could not be explained by the band bending, now can be explained by the direct interaction between surface states and defect states.

5.4 Conclusion of the luminescent study

Here we reported quantum mechanical simulations of different terminations of the (001) diamond surface, which is the dominant surface of small nanodiamonds [1] and a typical orientation to introduce NV-centers into bulk diamond. The applied method was able to reproduce the fundamental bandgap [9], as well as defect levels including charge transition levels [221] and excitation energies [9] in bulk diamond. we found that the hydrogen terminated diamond surface introduces deep, sub-bandgap states that are surface-related, delocalized image states. The

empty defect states of NV(-) would mix with these delocalized states. As a consequence, an electron excited by light into such a state, will be driven to the surface, will delocalize, and eventually get emitted (because of the NEA), leaving the NV defect in the neutral state. I also showed that, depending on the type of oxygenation, blinking or quenching of the luminescence can still occur. Full hydroxylation of the diamond surface still yields sub-bandgap image states. Even though these are shallower than on the hydrogenated surface, OH-coverage may still lead to either direct ionization of the NV(-) center or to bleaching at high-power laser excitation.

I also showed that even small nanodiamonds with H-termination have image states, influencing the photophysical properties of the embedded NV centers. Oxidation producing ether-like C-O-C bridges on the (001) diamond surface can lead to PEA and stabilize NV(-), but closely packed ether-like bridges introduce deep localized surface states into the bandgap, again causing bleaching or blinking. The fully fluorinated diamond surface provides the highest PEA, but here, too. I found surface related localized acceptor states close to the conduction band edge, which again can cause blinking at high power laser excitation of the NV-centers. On the basis of my study, I identified a combination of surface terminators, consisting of hydrogen, hydroxyl groups, and C-O-C bridges which in a random distribution lead to slight PEA and no surface related states would be ideal for NV-based nanosensing.

Chapter 6

Effect of the Size on the Diffusion Activation Energies

6.1 Introduction

Materials technology often relies on mass transfer by defect diffusion, therefore, understanding the diffusion processes is crucial for technology optimization [2, 222–224]. Diffusion can also play a significant role in controlling atomic redistribution and phase transformation during the fabrication of nano-crystalline materials [225]. In describing such processes, usually diffusion activation energy (DAE) data from the bulk are used even in nanoscale materials, although small size can have an effect on the DAE. There are two conflicting tendencies. On one hand, quantum confinement (QC) is expected to raise the energy difference between two configurations, and so the DAE. On the other hand, the increased relaxation freedom (RF), due to the closeness of the surface, should decrease it. These two effects have different strengths and length-scales, and their interplay will depend both on the material and on the particular diffusion mechanism. Within this study, this has been investigated for the DAE of a neutral vacancy (V) in diamond, by separating the two effects.

The diffusion of V in diamond is of special interest for the formation of the nitrogen-vacancy (NV) centers, which, as mentioned before, have received special attention lately, due to their stable, room-temperature, visible luminescence and unique spin states, with potential applications in quantum computing [44, 202–204, 226, 227], nanosensing [35], and biolabeling [54–58]. In

particular, this latter application requires NV centers in very small-sized nanodiamonds (ND). Therefore, the question arises: How such NDs with at least one NV center in them can be created? The answer is by irradiating and annealing nitrogen-doped nanodiamonds [13, 14, 69, 70]. It is usually assumed that NV centers are created by the capture of mobile (neutral) V at substitutional nitrogen impurities (N_s) [13, 14, 20, 166]. Obviously, out-diffusion of V from the ND is a competing process with NV formation. By a theoretical analysis of these processes, Barnard et al. [228] have predicted that the likelihood for the occurrence of an NV center in NDs, smaller than 5 nm in diameter is negligible. However, luminescence of the NV center in such NDs have been observed [53] in discrete 5 nm nanodiamonds at room temperature and their blinking has been switched on and off by modifying the surface of the nanodiamonds [53].

It is not clear whether this controversy could be due to an underestimation of the DAE by ignoring nanosize effects or not. Hereafter, we will explore the effect of size of nanodiamonds on the DAE.

6.2 Results

Standard density functional theory (DFT) in the generalized gradient approximation (GGA), using the Perdew-Burke-Ernzerhof (PBE) functional [97] is applied for the calculations. The calculations have been performed with the Vienna Ab initio Simulation Package (VASP 5.3) [229] using the projected augmented wave method [230]. The parameters of the present calculations are identical with those in our earlier paper on the formation of NV centers in bulk diamond [2]. 370 (740) eV as cut-off in the expansion of the wave function (charge density), and 0.01 eV/Å as the convergence limit for the forces have been used. DAE has been determined in hydrogen saturated clusters of different size and compared the results to the one obtained in the bulk, which is represented by a 512-atom 3D-periodic supercell. In the latter the DAE was obtained as 2.67 eV at 0 K, in good agreement with earlier LDA calculations ([231]), and reasonably overestimating the experimental value of 2.3±0.3 eV [188], observed at high temperature. (It should be noted that taking into account the vibrational contributions to the free energy, the barrier is lowered by 0.2 eV at 1000 K [2]). Three different cluster sizes have been considered,

$C_{44}H_{42}$, $C_{106}H_{86}$ and $C_{208}H_{139}$, with approximately 0.6, 0.8 and 1.2 nm in diameter, respectively (see Fig. 6.1).

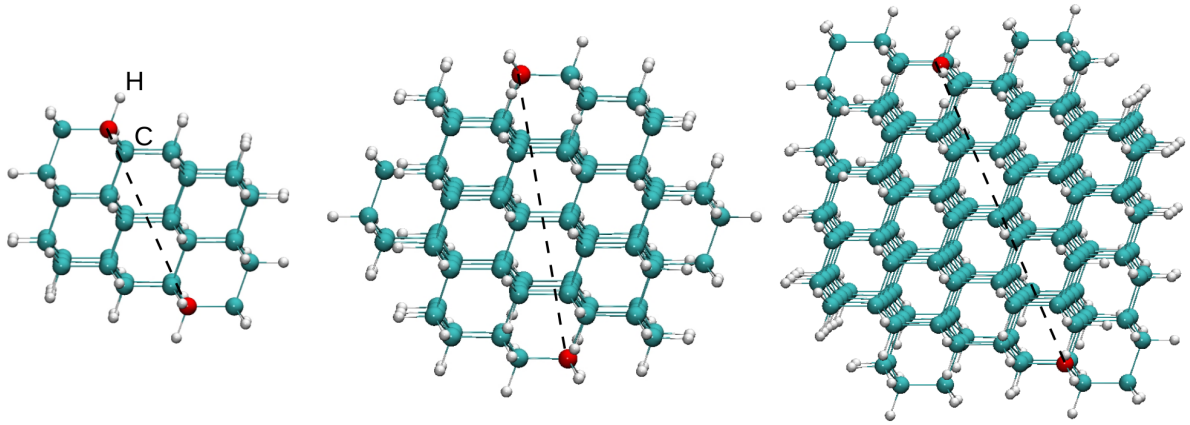

Figure 6.1: The clusters with a) 0.6 nm, b) 0.8 nm and c) 1.2 nm size. Carbon atoms are cyan and hydrogen atoms white. The size of the cluster was measured as the distance between the two farthermost carbon atoms shown in red.

Vacancy diffusion occurs through the jump of a neighboring lattice atom into the vacancy. In diamond, the saddle point of this motion is in the plane orthogonal to and halving the C-C bond, but off the bond center [232]. Therefore, clusters with increasing number of carbon shells around the bond-center site is built. The clusters were then truncated and terminated by hydrogen atoms in such a way that steric repulsion of the terminators be minimal. The perfect clusters have been fully relaxed and then a carbon atom has been removed from one side of the central bond, to create the vacancy.

In order to separate the QC effect from that of RF, two series of calculations have been performed. In the first one, the equilibrium state of the vacancy was determined by allowing all atoms to relax without constraint. The saddle point was then searched for by confining the moving carbon atom to the halving plane of the bond and minimizing the total energy. The energy difference between the saddle point and the ground state, *i.e.*, the DAE-Ea, for each cluster is shown in column 3 of table 6.1, and by large blue dots in Fig. 6.2.

In the second series, only the first neighbors of the two sites forming the central bond were allowed to relax, both in finding the equilibrium and the saddle point configuration. This way the RF is kept at the same level in all clusters and in the bulk supercell, so the change in

		Diffusion activation enery (DAE) in eV			
Clusters	L (nm)	Fully relaxed E_a (eV)	Constrained	$E_{QC} = E_a+E_c+E_c^\infty$	$E_{RF} = E_a -(E_c - E_c^\infty)$
$C_{44}H_{42}$	0.64	1.85	3.37	2.93	1.15
$C_{106}H_{86}$	0.89	2.51	3.24	2.80	1.94
$C_{214}H_{134}$	1.21	2.51	3.17	2.73	2.01
BULK	∞	2.67	3.11	2.67	2.23

Table 6.1: The DAE of the neutral V in diamond as a function of cluster size L. The 5th and 6th columns separate the effect of quantum confinement (QC) from the increasing relaxation freedom (RF). For more explanation see the text.

the DAE is expected to be entirely due to the QC effect. The corresponding values are shown in column 4 of table 6.1, and by large red dots in Fig. 6.2. The restriction to first-neighbor relaxation obviously leads to a higher DAE than the bulk value (black line in Fig. 6.2). The net effect of the QC can be estimated by shifting the points rigidly to match the bulk curve at the diameter of the 512-atom bulk supercell. The resulting values EQC are given in column 5 of table 6.1, and by small green dots in Fig. 6.2. The increase of the DAE due to quantum confinement can be matched by an $1/L^3$ curve (green in Fig. 6.2). To deduce the effect of the increasing RF, the increase due to QC (E_c - E_c^∞) has been subtracted from the DAE obtained with full relaxation. The resulting values E_{RF} are shown in column 6 of table 6.1, and as small pink dots in Fig. 6.2. The change of DAE with increasing RF can also be fitted by an $-1/L^3$ curve (pink in Fig. 6.2). The scattering of the data point with respect to the fitted curves are due to the fact that the clusters are of the same shape and the number of carbon atoms are only approximately $\sim L^3$. (This was necessary to avoid strong steric repulsion of H-terminators.)

Fig. 6.2 shows that the DAE is not a monotonous function of the size (see blue dots in Fig. 6.2). The reason for that in this particular case is that decrease of the DAE due to increasing RF ($-0.28/L^3$) is faster than the increase due to QC ($0.07/L^3$). It should be noted, however, that the effect of RF depends on the crystal structure and bond strength, *i.e.* on the host material, while the QC effect is determined by the diffusion mechanism, and the changes induced by that in the electronic structure. Therefore, the actual change of the DAE has to be calculated in each case explicitly.

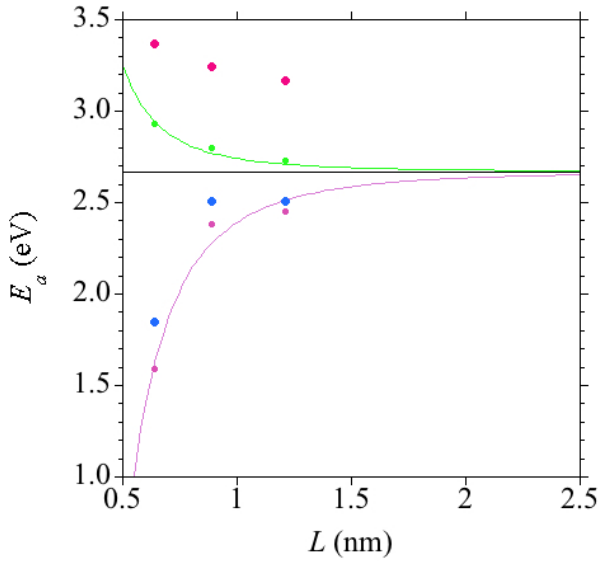

Figure 6.2: Size dependence of the DAE for the neutral V in diamond. The black line corresponds to the bulk value. Large red and large blue dots are the DAE values calculated with and without constraint, respectively. The green and pink lines represent the effect of quantum confinement (QC) and increasing relaxation freedom (RF) separately. For explanation see the text.

6.3 Conclusion of the diffusion study

In the particular case of nanodiamonds in the range desirable for biolabeling applications, that is less than 5 nm, our results clearly show that the bulk DAE is - if anything - an overestimation. This reinforces the estimate of Barnard et al. [228], who used the bulk value in their analysis. Still, very small NDs with NV-centers in them can be produced. This controversy may be resolved if the diffusion of V does not play a significant role in the formation of the NV-centers. In our earlier work [2], we have shown that the diffusion of V is more likely to lead to the formation of divacancies (V_2) than to NV-centers, while the formation of NV-centers by creating a vacancy next to a substitutional N during irradiation is energetically much more favorable than creating an isolated vacancy. These findings mean that, while annealing is important to heal the lattice after irradiation, diffusion of vacancies is not the primary mechanism to create NV centers.

Chapter 7

Conclusions

7.1 Works performed

In this thesis various structural and electronic properties of NV-center defects in diamond with the help of first-principles methods is investigated. These properties were unknown and of large interest to the theoretical and experimental community working on different disciplines from defect theory to the luminescent of nanostructures. Formation mechanisms of the NV-center and its interaction with different terminations of the diamond surface have been extensively studied. We have also investigated the formation of nanodiamonds and their thermal stability. We believe our study provides answers to the size limits of such structures. Further on, we have studied the defect diffusion in them.

In the course of this thesis computational methods at different levels have been used for various needs. Highly efficient, yet accurate enough method of density-functional-based tight-binding (DFTB) for molecular dynamics simulation of annealing processes has been used. This allowed us to investigate systems at sizes and time-scales that have not been studied before utilizing a first-principle level of precision. For some of the electronic structure calculations where precise gap states were desired we employed highly accurate and expensive first-principles method based on hybrid functionals in density functional theory (DFT) to predict the quantum states of defects which led to novel results.

Here in this closing chapter, important conclusions resulted from the studies performed are presented and later some ideas for future works are discussed.

7.1.1 Thermal stability of nanodiamonds

In this study I have established that nanodiamonds with special shapes (cube and cuboctahedral), above 1 nm in diameter, can sustain their crystalline structure even in high temperature annealing up to 1500 K. These studies have been performed in the presence of oxygen which plays two roles. First saturating the surface atoms and second etching the graphitic part. The interplay between these two mechanisms resulted in the findings that have halved the theoretical size-limit of nanodiamonds. This is an important finding as it will increase the potential of nanodiamonds for biomarker applications where the size of nanodiamond should be on the order of the size of biomolecules in the experiment. Experimentalist may benefit from these findings as a guideline toward the minimum size of nanodiamonds they can aim for.

7.1.2 Formation of nitrogen-vacancy(NV) center in bulk diamond

Based on calculated charge transition levels, barrier energy for migration and reaction energies of basic V- and nitrogen-related defects (NV, NVH, N_2, N_2V and V_2) we were able to reproduce charged transition levels and the prediction of the missing ones in accordance to current available experiments. In addition, the activation energies for V and NV diffusion have been calculated.We were also able to predict the conditions for creating NV centers enjoying the best possible efficiency in N-doped, irradiated and annealed diamond.My results show that irradiation is more likely to create NV defects directly than isolated vacancies while in post-irradiation annealing, many more divacancies are formed than NV defects. Since the divacancies are deeper acceptors than NV, the created NV defects will dominantly be in the neutral charge state, unless the concentration of divacancies are sufficiently decreased by annealing in higher temperatures. The prediction I had made here about a possible way of optimizing the concentration of the required negatively charged defect, has been very quickly confirmed experimentally by one of the leading groups in the field (PRB 90, 081117, 2014).

7.1.3 Luminescent of the near-surface NV centers in diamond

Our calculations in this part indicate that the diamond surface with full hydrogen and hydroxyl group terminations possess deep empty delocalized image states in the band gap due to their

negative electron affinity. The empty defect states of NV(-) would mix with these delocalized states. As a consequence, an electron excited by light into such a state, will be driven to the surface, will delocalize, and eventually get emitted, leaving the NV defect in the neutral state. Furthermore, I have shown that strongly oxidized surfaces (C-O-C bridge) with highly positive electron affinity (PEA) have empty acceptor type surface states below the conduction band. In case of high intensity (multi-photon excitation), these states can shelve the excited electrons, leading to blinking of the luminescence. Finally, I identified a combination of surface terminators, consisting of hydrogen, hydroxyl groups, and C-O-C bridges which in a random distribution lead to slight PEA and no surface related states. Similar combination of surface terminators may be formed in the early stage of thermal oxidation of hydrogenated diamond. This would be ideal for NV-based nanosensing.

7.1.4 Effect of the size on the diffusion

In the last part of this work the consequences of nano-size phenomena on the diffusion of defects were studied. Here, I investigated that in the nanosize range, the diffusion activation energy can be influenced by two effects: First, the quantum confinement effect and second, the relaxation freedom due to the closeness of the surface. The quantum confinement will increase the value of the diffusion activation energy while the relaxation decreases it. We have chosen the diffusion of the neutral vacancy defect for the purpose of creating the NV-centers in nanodiamonds. It has been shown that using the bulk value of the activation energy for this particular case is an overestimation. This reinforces the estimate of Barnard et al. [228], who used the bulk value in their analysis. Yet, very small nanodiamonds containing fluorescence NV centers have been reported. We believe that this controversy can be resolved if the diffusion of V does not play a significant role in the formation of the NV centers. In fact in our previous publication 7.1.2 we have shown that the diffusion of vacancy is more likely to lead to the formation of divacancies (V_2) than to the NV centers, while the formation of NV centers by creating a vacancy next to a substitutional N during irradiation is energetically much more favorable than creating an isolated vacancy.

7.2 Future works

During working on the topics presented in this thesis, questions and subsequently ideas for further research come up. Here, I briefly mention few of them:

- The DFTB based MD techniques used here in realizing nanodiamond structures are a powerful tool which can be used on a variety of systems. Particularly, it showed success for the case of carbon based systems (sp^2 and sp^3 formations) interacting with saturating/etching oxygens. There are many other systems that can benefit from this large-scale and long time-scale first-principles based method such as graphene, carbon nanotubes and fullerenes. These are the most probable candidates for nanoelectronics applications. A detailed MD study on any of these carbon bases systems in the presence of oxygen and hydrogen can be useful for obtaining a more clear picture of the nanostructures worked on in experiments. Using first-principle quality MD on systems with thousands of atoms in the picosecond regime is possible with DFTB using a moderate computational power.

- One topic parallel to our bulk study [2] that can be worked on is investigating other defects in the bulk diamond such as vacancy-related emitters XV (V: vacancy, X: Si, Ni, Cr). Silicon is in the same column with carbon sharing many electronic properties, however, for transition metals such as nickel and chromium many different features are expected to rise. Incorporation of magnetic elements in semiconductors is an active research field that can lead to applications in spintronics.

- For altering the electronic properties of diamonds and find other ways to obtain negatively charged NV-centers there are still many choices for surface doping that have not been tested. Elements from halogens, transition metals or even heavy elements alone or in combination with each other and/or oxygen can have unpredicted results along with fascinating physics to uncover.

References

[1] M. Kaviani, P. Deák, B. Aradi, T. Köhler, and T. Frauenheim. How small nanodiamonds can be? md study of the stability against graphitization. *Diamond and Related Materials*, 33:78–84, 2013.

[2] P. Deák, B. Aradi, M. Kaviani, T. Frauenheim, and A. Gali. Formation of nv centers in diamond: A theoretical study based on calculated transitions and migration of nitrogen and vacancy related defects. *Physical Review B*, 89(7):075203, 2014.

[3] M. Kaviani, P. Deák, B. Aradi, T. Frauenheim, J. Chou, and A. Gali. Proper surface termination for luminescent near-surface nv centers in diamond. *Nano letters*, 14(8):4772–4777, 2014.

[4] M. Kaviani, T. Frauenheim, and P. Deák. Formation of nv-centers in nanodiamonds: nano-size effects on point defect diffusion. In preparation.

[5] E. Kaxiras. *Atomic and electronic structure of solids*. Cambridge University Press, 2003.

[6] M. Omar. *Elementary solid state physics: principles and applications*, volume 157. Addison-Wesley Reading, MA, USA:, 1975.

[7] A. Alkauskas, J. Neugebauer, A. Pasquarello, C. Van de Walle, et al. *Advanced Calculations for Defects in Materials: Electronic Structure Methods*. John Wiley & Sons, 2011.

[8] C. Kittel and P. McEuen. *Introduction to solid state physics*, volume 8. Wiley New York, 1976.

[9] A. Gali. Theory of the neutral nitrogen-vacancy center in diamond and its application to the realization of a qubit. *Physical Review B*, 79(23):235210, 2009.

[10] A. Stoneham. *Theory of defects in solids*. Clarendon, 1975.

[11] P. Deák, A. Gali, B. Aradi, and T. Frauenheim. Accurate gap levels and their role in the reliability of other calculated defect properties. *physica status solidi (b)*, 248(4):790–798, 2011.

[12] II. Vlasov, VG. Ralchenko, AV. Khomich, SV. Nistor, D. Shoemaker, and RA. Khmelnitskii. Relative abundance of single and vacancy-bonded substitutional nitrogen in cvd diamond. *physica status solidi (a)*, 181(1):83–90, 2000.

[13] FC. Waldermann, P. Olivero, J. Nunn, K. Surmacz, ZY. Wang, D. Jaksch, RA. Taylor, IA. Walmsley, M. Draganski, P. Reichart, et al. Creating diamond color centers for quantum optical applications. *Diamond and Related Materials*, 16(11):1887–1895, 2007.

[14] A. Mainwood. Nitrogen and nitrogen-vacancy complexes and their formation in diamond. *Physical Review B*, 49(12):7934, 1994.

[15] J. Tisler, G. Balasubramanian, B. Naydenov, R. Kolesov, B.ernhard Grotz, R. Reuter, J. Boudou, P. Curmi, M. Sennour, A. Thorel, et al. Fluorescence and spin properties of defects in single digit nanodiamonds. *Acs Nano*, 3(7):1959–1965, 2009.

[16] J. Meijer, B. Burchard, M. Domhan, C. Wittmann, T. Gaebel, I. Popa, F. Jelezko, and J. Wrachtrup. Generation of single color centers by focused nitrogen implantation. *Applied Physics Letters*, 87(26):261909, 2005.

[17] M. Doherty, N. Manson, P. Delaney, F. Jelezko, J. Wrachtrup, and L. Hollenberg. The nitrogen-vacancy colour centre in diamond. *Physics Reports*, 528(1):1–45, 2013.

[18] J. Loubser and J. van Wyk. Electron spin resonance in the study of diamond. *Reports on Progress in Physics*, 41(8):1201, 1978.

[19] JHN. Loubser and JA. Van Wyk. Optical spin-polarisation in a triplet state in irradiated and annealed type 1b diamonds. 1977.

[20] G. Davies and MF. Hamer. Optical studies of the 1.945 ev vibronic band in diamond. *Proceedings of the Royal Society of London. A. Mathematical and Physical Sciences*, 348(1653):285–298, 1976.

[21] Y. Mita. Change of absorption spectra in type-ib diamond with heavy neutron irradiation. *Physical Review B*, 53(17):11360, 1996.

[22] DA. Redman, S. Brown, RH. Sands, and SC. Rand. Spin dynamics and electronic states of n-v centers in diamond by epr and four-wave-mixing spectroscopy. *Physical review letters*, 67(24):3420, 1991.

[23] K. Iakoubovskii, GJ. Adriaenssens, and M. Nesladek. Photochromism of vacancy-related centres in diamond. *Journal of Physics: Condensed Matter*, 12(2):189, 2000.

[24] A. Gruber, A. Dräbenstedt, C. Tietz, L. Fleury, J. Wrachtrup, and C. Von Borczyskowski. Scanning confocal optical microscopy and magnetic resonance on single defect centers. *Science*, 276(5321):2012–2014, 1997.

[25] HB. Dyer, FA. Raal, L. Du Preez, and JHN. Loubser. Optical absorption features associated with paramagnetic nitrogen in diamond. *Philosophical Magazine*, 11(112):763–774, 1965.

[26] G. Davies. Dynamic jahn-teller distortions at trigonal optical centres in diamond. *Journal of Physics C: Solid State Physics*, 12(13):2551, 1979.

[27] S. Cui and E. Hu. Increased negatively charged nitrogen-vacancy centers in fluorinated diamond. *Applied Physics Letters*, 103(5):051603, 2013.

[28] C. Kurtsiefer, S. Mayer, P. Zarda, and H. Weinfurter. Stable solid-state source of single photons. *Physical Review Letters*, 85(2):290, 2000.

[29] L. Childress, M. Dutt, JM. Taylor, AS. Zibrov, F. Jelezko, J. Wrachtrup, and MD. Hemmer, PR .and Lukin. Coherent dynamics of coupled electron and nuclear spin qubits in diamond. *Science*, 314(5797):281–285, 2006.

[30] P. Hemmer, S. Prawer, E. Trajkov, J. Wrachtrup, F. Jelezko, N. Manson, and M. Sellars. Vlsi quantum computer in diamond. In *Integrated Optoelectronic Devices 2006*, pages 61300E–61300E. International Society for Optics and Photonics, 2006.

[31] M. Dutt, L. Childress, L. Jiang, E. Togan, J. Maze, F. Jelezko, AS. Zibrov, PR. Hemmer, and MD. Lukin. Quantum register based on individual electronic and nuclear spin qubits in diamond. *Science*, 316(5829):1312–1316, 2007.

[32] P. Neumann, N. Mizuochi, F. Rempp, P. Hemmer, H. Watanabe, S. Yamasaki, V. Jacques, T. Gaebel, F. Jelezko, and J. Wrachtrup. Multipartite entanglement among single spins in diamond. *science*, 320(5881):1326–1329, 2008.

[33] JS Jiang, L., P. Maze, JR .and Maurer, JM. Taylor, DG. Cory, PR. Hemmer, RL. Walsworth, A. Yacoby, AS. Zibrov, et al. Repetitive readout of a single electronic spin via quantum logic with nuclear spin ancillae. *Science*, 326(5950):267–272, 2009.

[34] GD. Fuchs, VV. Dobrovitski, DM. Toyli, FJ. Heremans, and DD. Awschalom. Gigahertz dynamics of a strongly driven single quantum spin. *Science*, 326(5959):1520–1522, 2009.

[35] J. Maze, P. Stanwix, J. Hodges, S. Hong, J. Taylor, P. Cappellaro, L. Jiang, M. Dutt, E. Togan, A. Zibrov, et al. Nanoscale magnetic sensing with an individual electronic spin in diamond. *Nature*, 455(7213):644–647, 2008.

[36] G. Balasubramanian, I. Chan, R. Kolesov, M. Al-Hmoud, J. Tisler, C. Shin, C. Kim, A. Wojcik, P. Hemmer, A. Krueger, et al. Nanoscale imaging magnetometry with diamond spins under ambient conditions. *Nature*, 455(7213):648–651, 2008.

[37] JM. Taylor, P. Cappellaro, L. Childress, L. Jiang, D. Budker, PR. Hemmer, A. Yacoby, R. Walsworth, and MD. Lukin. High-sensitivity diamond magnetometer with nanoscale resolution. *Nature Physics*, 4(10):810–816, 2008.

[38] F. Dolde, H. Fedder, M. Doherty, T. Nöbauer, F. Rempp, G. Balasubramanian, T. Wolf, F. Reinhard, LCL. Hollenberg, F. Jelezko, et al. Electric-field sensing using single diamond spins. *Nature Physics*, 7(6):459–463, 2011.

[39] G. Kucsko, PC. Maurer, NY. Yao, M. Kubo, HJ. Noh, PK. Lo, H. Park, and MD. Lukin. Nanometre-scale thermometry in a living cell. *Nature*, 500(7460):54–58, 2013.

[40] D. Toyli, F. Charles, D. Christle, V. Dobrovitski, and D. Awschalom. Fluorescence thermometry enhanced by the quantum coherence of single spins in diamond. *Proceedings of the National Academy of Sciences*, 110(21):8417–8421, 2013.

[41] P. Neumann, I. Jakobi, F. Dolde, C. Burk, R. Reuter, G. Waldherr, J. Honert, T. Wolf, A. Brunner, J. Shim, et al. High-precision nanoscale temperature sensing using single defects in diamond. *Nano letters*, 13(6):2738–2742, 2013.

[42] V. Petráková, A. Taylor, I. Kratochvilova, F. Fendrych, J. Vacík, J. Kučka, J. Štursa, P. Cigler, M. Ledvina, A. Fišerová, et al. Luminescence of nanodiamond driven by atomic functionalization: towards novel detection principles. *Advanced Functional Materials*, 22(4):812–819, 2012.

[43] R. Brouri, A. Beveratos, J. Poizat, and P. Grangier. Photon antibunching in the fluorescence of individual color centers in diamond. *Optics Letters*, 25(17):1294–1296, 2000.

[44] F. Jelezko, T. Gaebel, I. Popa, M. Domhan, A. Gruber, and J. Wrachtrup. Observation of coherent oscillation of a single nuclear spin and realization of a two-qubit conditional quantum gate. *Physical Review Letters*, 93(13):130501, 2004.

[45] C. Fu, H. Lee, K. Chen, T. Lim, H. Wu, P. Lin, P. Wei, P. Tsao, H. Chang, and W. Fann. Characterization and application of single fluorescent nanodiamonds as cellular biomarkers. *Proceedings of the National Academy of Sciences*, 104(3):727–732, 2007.

[46] J. Rabeau, A. Stacey, A. Rabeau, S. Prawer, F. Jelezko, I. Mirza, and J. Wrachtrup. Single nitrogen vacancy centers in chemical vapor deposited diamond nanocrystals. *Nano letters*, 7(11):3433–3437, 2007.

[47] O. Shenderova, V. Grichko, S. Hens, and J. Walch. Detonation nanodiamonds as uv radiation filter. *Diamond and Related Materials*, 16(12):2003–2008, 2007.

[48] Y. Sonnefraud, A. Cuche, O. Faklaris, J. Boudou, T. Sauvage, J. Roch, F. Treussart, and S. Huant. Diamond nanocrystals hosting single nitrogen-vacancy color centers sorted by photon-correlation near-field microscopy. *Optics letters*, 33(6):611–613, 2008.

[49] Y. Chang, H. Lee, K. Chen, C. Chang, D. Tsai, C. F, Tsong-Shin L, Yan-Kai T, Chia-Yi F, CC Han, et al. Mass production and dynamic imaging of fluorescent nanodiamonds. *Nature nanotechnology*, 3(5):284–288, 2008.

[50] W. WuáPai et al. Fluorescence enhancement and lifetime modification of single nanodiamonds near a nanocrystalline silver surface. *Physical Chemistry Chemical Physics*, 11(10):1508–1514, 2009.

[51] C. Bradac, T. Gaebel, N. Naidoo, J. Rabeau, and A. Barnard. Prediction and measurement of the size-dependent stability of fluorescence in diamond over the entire nanoscale. *Nano letters*, 9(10):3555–3564, 2009.

[52] I. Vlasov, O. Shenderova, S. Turner, O. I Lebedev, A. Basov, I. Sildos, M. Rähn, A. Shiryaev, and G. Van Tendeloo. Nitrogen and luminescent nitrogen-vacancy defects in detonation nanodiamond. *Small*, 6(5):687–694, 2010.

[53] C. Bradac, T. Gaebel, N. Naidoo, M. Sellars, J. Twamley, L. Brown, A. Barnard, T. Plakhotnik, A. Zvyagin, and J. Rabeau. Observation and control of blinking nitrogen-vacancy centres in discrete nanodiamonds. *Nature nanotechnology*, 5(5):345–349, 2010.

[54] K. Ushizawa, Y. Sato, T. Mitsumori, T. Machinami, T. Ueda, and T. Ando. Covalent immobilization of dna on diamond and its verification by diffuse reflectance infrared spectroscopy. *Chemical Physics Letters*, 351(1):105–108, 2002.

[55] S. Dahoumane, M. Nguyen, A. Thorel, J. Boudou, M. Chehimi, and C. Mangeney. Protein-functionalized hairy diamond nanoparticles. *Langmuir*, 25(17):9633–9638, 2009.

[56] V. Vaijayanthimala and H. Chang. Functionalized fluorescent nanodiamonds for biomedical applications. 2009.

[57] D. Ho. Beyond the sparkle: the impact of nanodiamonds as biolabeling and therapeutic agents. *ACS nano*, 3(12):3825–3829, 2009.

[58] A. Schrand, S. Hens, and O. Shenderova. Nanodiamond particles: properties and perspectives for bioapplications. *Critical reviews in solid state and materials sciences*, 34(1-2):18–74, 2009.

[59] N. Mohan, C. Chen, H. Hsieh, Y. Wu, and H. Chang. In vivo imaging and toxicity assessments of fluorescent nanodiamonds in caenorhabditis elegans. *Nano letters*, 10(9):3692–3699, 2010.

[60] JP. Goss, R. Jones, SJ. Breuer, PR. Briddon, and S. Öberg. The twelve-line 1.682 ev luminescence center in diamond and the vacancy-silicon complex. *Physical review letters*, 77(14):3041, 1996.

[61] A. Gali, M. Fyta, and E. Kaxiras. Ab initio supercell calculations on nitrogen-vacancy center in diamond: Electronic structure and hyperfine tensors. *Physical Review B*, 77(15):155206, 2008.

[62] J. Larsson and P. Delaney. Electronic structure of the nitrogen-vacancy center in diamond from first-principles theory. *Physical Review B*, 77(16):165201, 2008.

[63] Faruque M Hossain, M. Doherty, H. Wilson, and L. Hollenberg. Ab initio electronic and optical properties of the n-v-center in diamond. *Physical review letters*, 101(22):226403, 2008.

[64] BV. Spitsyn, JL. Davidson, MN. Gradoboev, TB. Galushko, NV. Serebryakova, TA. Karpukhina, II. Kulakova, and NN. Melnik. Inroad to modification of detonation nanodiamond. *Diamond and related materials*, 15(2):296–299, 2006.

[65] G. Post, V. Dolmatov, VA. Marchukov, VG. Sushchev, MV. Veretennikova, and AE. Sal'ko. Industrial synthesis of ultradisperse detonation diamonds and some fields of their use. *Russian journal of applied chemistry*, 75(5):755–760, 2002.

[66] V. Mochalin, O. Shenderova, D. Ho, and Y. Gogotsi. The properties and applications of nanodiamonds. *Nature Nanotechnology*, 7(1):11–23, 2012.

[67] O. Shenderova and D. Gruen. *Ultrananocrystalline diamond: synthesis, properties and applications*. William Andrew, 2012.

[68] VL. Kuznetsov, IL. Zilberberg, Y. Butenko, AL. Chuvilin, and B. Segall. Theoretical study of the formation of closed curved graphite-like structures during annealing of diamond surface. *Journal of applied physics*, 86(2):863–870, 1999.

[69] V. Dolmatov. Detonation synthesis ultradispersed diamonds: properties and applications. *Russian Chemical Reviews*, 70(7):607, 2001.

[70] A. Krüger, F. Kataoka, M. a al Ozawa, T. Fujino, Y. Suzuki, AE. Aleksenskii, A. Vul, and E. Ōsawa. Unusually tight aggregation in detonation nanodiamond: identification and disintegration. *Carbon*, 43(8):1722–1730, 2005.

[71] S. Osswald, G. Yushin, V. Mochalin, S. Kucheyev, and Y. Gogotsi. Control of sp2/sp3 carbon ratio and surface chemistry of nanodiamond powders by selective oxidation in air. *Journal of the American Chemical Society*, 128(35):11635–11642, 2006.

[72] K. Fu, C. Santori, PE. Barclay, and RG. Beausoleil. Conversion of neutral nitrogen-vacancy centers to negatively charged nitrogen-vacancy centers through selective oxidation. *Applied Physics Letters*, 96(12):121907, 2010.

[73] J. Havlik, V. Petrakova, Ivan Rehor, Vaclav P., G. Michal, Jan S., Jan K., Jan R., Torsten R., San-Yung L., et al. Boosting nanodiamond fluorescence: towards development of brighter probes. *Nanoscale*, 5(8):3208–3211, 2013.

[74] J. Raty and G. Galli. Ultradispersity of diamond at the nanoscale. *Nature Materials*, 2(12):792–795, 2003.

[75] J. Raty and G. Galli. First principle study of nanodiamond optical and electronic properties. *Computer physics communications*, 169(1):14–19, 2005.

[76] B. Pate. The diamond surface: atomic and electronic structure. *Surface science*, 165(1):83–142, 1986.

[77] SJ. Sque, R. Jones, and PR. Briddon. Structure, electronics, and interaction of hydrogen and oxygen on diamond surfaces. *Physical review B*, 73(8):085313, 2006.

[78] R. Long, Y. Dai, and M. Guo. Characterization of diamond (100) surface with oxygen termination. *Applied Surface Science*, 254(9):2851–2855, 2008.

[79] S. Harris and DG. Goodwin. Growth on the reconstructed diamond (100) surface. *The Journal of Physical Chemistry*, 97(1):23–28, 1993.

[80] A. Paoletti and A. Tucciarone. *The physics of diamond*, volume 135. IOS Press, 1997.

[81] L. Rondin, G. Dantelle, A. Slablab, F. Grosshans, F. Treussart, P. Bergonzo, S. Perruchas, T. Gacoin, M. Chaigneau, H-C. Chang, et al. Surface-induced charge state conversion of nitrogen-vacancy defects in nanodiamonds. *Physical Review B*, 82(11):115449, 2010.

[82] M. Born and R. Oppenheimer. Zur quantentheorie der molekeln. *Annalen der Physik*, 389(20):457–484, 1927.

[83] P. Hohenberg and W. Kohn. Inhomogeneous electron gas. *Physical review*, 136(3B):B864, 1964.

[84] W. Kohn and L. Sham. Self-consistent equations including exchange and correlation effects. *Physical Review*, 140(4A):A1133, 1965.

[85] M. Marques and E. Gross. Time-dependent density functional theory. *Annu. Rev. Phys. Chem.*, 55:427–455, 2004.

[86] E. Runge and E. Gross. Density-functional theory for time-dependent systems. *Physical Review Letters*, 52(12):997, 1984.

[87] A. Alkauskas, P. Broqvist, and A. Pasquarello. Defect levels through hybrid density functionals: Insights and applications. *physica status solidi (b)*, 248(4):775–789, 2011.

[88] J. Tao, J. Perdew, V. Staroverov, and G. Scuseria. Climbing the density functional ladder: Nonempirical meta–generalized gradient approximation designed for molecules and solids. *Physical Review Letters*, 91(14):146401, 2003.

[89] J.ohn P Perdew and K.arla Schmidt. Jacob's ladder of density functional approximations for the exchange-correlation energy. In *AIP Conference Proceedings*, pages 1–20. IOP INSTITUTE OF PHYSICS PUBLISHING LTD, 2001.

[90] W. Kohn. Nobel lecture: Electronic structure of matter¯wave functions and density functionals. *Rev. Mod. Phys.*, 71:1253–1266, Oct 1999.

[91] M. Gell-Mann and K. Brueckner. Correlation energy of an electron gas at high density. *Physical Review*, 106(2):364, 1957.

[92] D. Ceperley and B. Alder. Ground state of the electron gas by a stochastic method. *Physical Review Letters*, 45(7):566, 1980.

[93] J. Perdew and A. Zunger. Self-interaction correction to density-functional approximations for many-electron systems. *Physical Review B*, 23(10):5048, 1981.

[94] J. Perdew and Y. Wang. Accurate and simple analytic representation of the electron-gas correlation energy. *Physical Review B*, 45(23):13244, 1992.

[95] S. Vosko, L. Wilk, and M. Nusair. Accurate spin-dependent electron liquid correlation energies for local spin density calculations: a critical analysis. *Canadian Journal of Physics*, 58(8):1200–1211, 1980.

[96] J. Perdew. Accurate density functional for the energy: Real-space cutoff of the gradient expansion for the exchange hole. *Physical Review Letters*, 55(16):1665, 1985.

[97] J. Perdew, K. Burke, and M. Ernzerhof. Generalized gradient approximation made simple. *Physical review letters*, 77(18):3865, 1996.

[98] A. Becke. Density-functional exchange-energy approximation with correct asymptotic behavior. *Physical Review A*, 38(6):3098, 1988.

[99] C. Lee, W. Yang, and R. Parr. Development of the colle-salvetti correlation-energy formula into a functional of the electron density. *Phys. Rev. B*, 37:785–789, Jan 1988.

[100] W. Kohn, Y. Meir, and D. Makarov. van der waals energies in density functional theory. *Physical review letters*, 80(19):4153, 1998.

[101] M. Lein, J. Dobson, and E. Gross. Toward the description of van der waals interactions within density functional theory. *Journal of computational chemistry*, 20(1):12–22, 1999.

[102] J. Dobson and B. Dinte. Constraint satisfaction in local and gradient susceptibility approximations: Application to a van der waals density functional. *Physical review letters*, 76(11):1780, 1996.

[103] Y. Andersson, D. C. Langreth, and B. I. Lundqvist. van der waals interactions in density-functional theory. *Phys. Rev. Lett.*, 76:102–105, Jan 1996.

[104] C. Freysoldt, Blazej Grabowski, Tilmann H., J. N., G. Kresse, A. Janotti, and C. Van de Walle. First-principles calculations for point defects in solids. *Reviews of Modern Physics*, 86(1):253, 2014.

[105] S. Lany and A. Zunger. Assessment of correction methods for the band-gap problem and for finite-size effects in supercell defect calculations: case studies for zno and gaas. *Physical Review B*, 78(23):235104, 2008.

[106] A. Janotti and C. Van de Walle. Native point defects in zno. *Physical Review B*, 76(16):165202, 2007.

[107] C. Stampfl, C. G. Van de Walle, D. Vogel, P. Krüger, and J. Pollmann. Native defects and impurities in inn: First-principles studies using the local-density approximation and self-interaction and relaxation-corrected pseudopotentials. *Phys. Rev. B*, 61:R7846–R7849, Mar 2000.

[108] S. Lany and A. Zunger. Polaronic hole localization and multiple hole binding of acceptors in oxide wide-gap semiconductors. *Physical Review B*, 80(8):085202, 2009.

[109] D. Bilc, R. Orlando, R. Shaltaf, G. Rignanese, J. Íñiguez, and P. Ghosez. Hybrid exchange-correlation functional for accurate prediction of the electronic and structural properties of ferroelectric oxides. *Physical Review B*, 77(16):165107, 2008.

[110] S. Lany and A. Zunger. Accurate prediction of defect properties in density functional supercell calculations. *Modelling and Simulation in Materials Science and Engineering*, 17(8):084002, 2009.

[111] C. Persson, Y. Zhao, S. Lany, and A. Zunger. n-type doping of cuin se 2 and cuga se 2. *Physical Review B*, 72(3):035211, 2005.

[112] S. Zhang. The microscopic origin of the doping limits in semiconductors and wide-gap materials and recent developments in overcoming these limits: a review. *Journal of Physics: Condensed Matter*, 14(34):R881, 2002.

[113] S. Lany and A. Zunger. Assessment of correction methods for the band-gap problem and for finite-size effects in supercell defect calculations: Case studies for zno and gaas. *Phys. Rev. B*, 78:235104, Dec 2008.

[114] A. Becke. Density-functional thermochemistry. iii. the role of exact exchange. *The Journal of Chemical Physics*, 98(7):5648–5652, 1993.

[115] J. Robertson, P. Peacock, M. Towler, and R. Needs. Electronic structure of p-type conducting transparent oxides. *Thin Solid Films*, 411(1):96–100, 2002.

[116] C. Patterson. Role of defects in ferromagnetism in zn 1- x co x o: a hybrid density-functional study. *Physical Review B*, 74(14):144432, 2006.

[117] M. Usuda, N. Hamada, T. Kotani, and M. van Schilfgaarde. All-electron gw calculation based on the lapw method: Application to wurtzite zno. *Physical Review B*, 66(12):125101, 2002.

[118] J. Talman and W. Shadwick. Optimized effective atomic central potential. *Physical Review A*, 14(1):36, 1976.

[119] R. Godby, M. Schlüter, and L. Sham. Accurate exchange-correlation potential for silicon and its discontinuity on addition of an electron. *Physical review letters*, 56(22):2415, 1986.

[120] A. Görling and M. Levy. Exact kohn-sham scheme based on perturbation theory. *Physical Review A*, 50(1):196, 1994.

[121] P.atrick Rinke, A. Qteish, J. Neugebauer, C. Freysoldt, and M. Scheffler. Combining gw calculations with exact-exchange density-functional theory: an analysis of valence-band photoemission for compound semiconductors. *New Journal of Physics*, 7(1):126, 2005.

[122] H. Komsa, T. Rantala, and A. Pasquarello. Finite-size supercell correction schemes for charged defect calculations. *Physical Review B*, 86(4):045112, 2012.

[123] G. Makov and M. Payne. Periodic boundary conditions in ab initio calculations. *Physical Review B*, 51(7):4014, 1995.

[124] C. W. M. Castleton and S. Mirbt. Finite-size scaling as a cure for supercell approximation errors in calculations of neutral native defects in InP. *Phys. Rev. B*, 70:195202, Nov 2004.

[125] C. W. M. Castleton, A. Höglund, and S. Mirbt. Managing the supercell approximation for charged defects in semiconductors: Finite-size scaling, charge correction factors, the band-gap problem, and the ab initio dielectric constant. *Phys. Rev. B*, 73:035215, Jan 2006.

[126] N. D. M. Hine, K. Frensch, W. M. C. Foulkes, and M. W. Finnis. Supercell size scaling of density functional theory formation energies of charged defects. *Phys. Rev. B*, 79:024112, Jan 2009.

[127] S. Taylor and F. Bruneval. Understanding and correcting the spurious interactions in charged supercells. *Phys. Rev. B*, 84:075155, Aug 2011.

[128] H. Komsa, T. Rantala, and A. Pasquarello. Finite-size supercell correction schemes for charged defect calculations. *Phys. Rev. B*, 86:045112, Jul 2012.

[129] G. Makov and M. C. Payne. Periodic boundary conditions in ab initio calculations. *Phys. Rev. B*, 51:4014–4022, Feb 1995.

[130] C. Freysoldt, J. Neugebauer, and C. Van de Walle. Fully ab initio finite-size corrections for charged-defect supercell calculations. *Phys. Rev. Lett.*, 102:016402, Jan 2009.

[131] H. Hellmann. A new approximation method in the problem of many electrons. *The Journal of Chemical Physics*, 3(1):61–61, 1935.

[132] D. Porezag, Th. Frauenheim, Th. Köhler, G. Seifert, and R. Kaschner. Construction of tight-binding-like potentials on the basis of density-functional theory: Application to carbon. *Phys. Rev. B*, 51:12947–12957, May 1995.

[133] P. Zapol, Michael Sternberg, Larry A. Curtiss, Thomas Frauenheim, and Dieter M. Gruen. Tight-binding molecular-dynamics simulation of impurities in ultrananocrystalline diamond grain boundaries. *Phys. Rev. B*, 65:045403, Dec 2001.

[134] T. Frauenheim, G. Seifert, M. Elstner, T. Niehaus, C. Köhler, M. Amkreutz, M. Sternberg, Z. Hajnal, A. Di Carlo, and S. Suhai. Atomistic simulations of complex materials: ground-state and excited-state properties. *Journal of Physics: Condensed Matter*, 14(11):3015, 2002.

[135] B. Aradi, B. Hourahine, and Th. Frauenheim. Dftb+, a sparse matrix-based implementation of the dftb method. *The Journal of Physical Chemistry A*, 111(26):5678–5684, 2007.

[136] H. Huang, E. Pierstorff, E.iji Osawa, and D.ean Ho. Active nanodiamond hydrogels for chemotherapeutic delivery. *Nano letters*, 7(11):3305–3314, 2007.

[137] W. Chan. *Bio-applications of Nanoparticles*. Springer, 2007.

[138] A. Barnard, S. Russo, and I. Snook. Ab initio modelling of band states in doped diamond. *Philosophical Magazine*, 83(9):1163–1174, 2003.

[139] A. Barnard, S. Russo, and I. Snook. Structural relaxation and relative stability of nanodiamond morphologies. *Diamond and related materials*, 12(10):1867–1872, 2003.

[140] J. Raty, G. Galli, C. Bostedt, T. van Buuren, and L. Terminello. Quantum confinement and fullerenelike surface reconstructions in nanodiamonds. *Physical review letters*, 90(3):037401, 2003.

[141] K. Holt. Diamond at the nanoscale: applications of diamond nanoparticles from cellular biomarkers to quantum computing. *Philosophical Transactions of the Royal Society A: Mathematical, Physical and Engineering Sciences*, 365(1861):2845–2861, 2007.

[142] A. Bródka, Ł. Hawełek, A. Burian, S. Tomita, and V. Honkimäki. Molecular dynamics study of structure and graphitization process of nanodiamonds. *Journal of Molecular Structure*, 887(1):34–40, 2008.

[143] J. Leyssale and G. Vignoles. Molecular dynamics evidences of the full graphitization of a nanodiamond annealed at 1500k. *Chemical Physics Letters*, 454(4):299–304, 2008.

[144] G. Lee, C. Wang, J. Yu, E. Yoon, and K. Ho. Heat-induced transformation of nanodiamond into a tube-shaped fullerene: A molecular dynamics simulation. *Physical review letters*, 91(26):265701, 2003.

[145] AS. Barnard, SP. Russo, and IK. Snook. Size dependent phase stability of carbon nanoparticles: Nanodiamond versus fullerenes. *The Journal of chemical physics*, 118(11):5094–5097, 2003.

[146] S. Skokov, B. Weiner, M. Frenklach, Th. Frauenheim, and M. Sternberg. Dimer-row pattern formation in diamond (100) growth. *Phys. Rev. B*, 52:5426–5432, Aug 1995.

[147] R. Astala, M. Kaukonen, R. M. Nieminen, G. Jungnickel, and T. Frauenheim. Properties of small carbon clusters inside the c_{60} fullerene. *Phys. Rev. B*, 65:245423, Jun 2002.

[148] Th. Frauenheim, U. Stephan, P. Blaudeck, D. Porezag, H.-G. Busmann, W. Zimmermann-Edling, and S. Lauer. Stability, reconstruction, and electronic properties of diamond (100) and (111) surfaces. *Phys. Rev. B*, 48:18189–18202, Dec 1993.

[149] M. Sternberg, Th. Frauenheim, W. Zimmermann-Edling, and H. Busmann. Stm images from diamond surfaces: steps towards comparisons of experiment and theory. *Surface science*, 370(2):232–244, 1997.

[150] G. Jungnickel, D. Porezag, T. Frauenheim, M. Heggie, W. Lambrecht, B. Segall, and J. Angus. Graphitization effects on diamond surfaces and the diamond/graphite interface. *physica status solidi (a)*, 154(1):109–125, 1996.

[151] M. Sternberg, W. R. L. Lambrecht, and Th. Frauenheim. Molecular-dynamics study of diamond/silicon (001) interfaces with and without graphitic interface layers. *Phys. Rev. B*, 56:1568–1580, Jul 1997.

[152] Th. Köhler, Th. Frauenheim, and G. Jungnickel. Stability, chemical bonding, and vibrational properties of amorphous carbon at different mass densities. *Phys. Rev. B*, 52:11837–11844, Oct 1995.

[153] G. Jungnickel, Th. Köhler, Th. Frauenheim, M. Haase, P. Blaudeck, and U. Stephan. Structure and chemical bonding in amorphous diamond. *Diamond and related materials*, 5(2):175–185, 1996.

[154] G. Seifert, T. Köhler, and T. Frauenheim. Molecular wires, solenoids, and capacitors by sidewall functionalization of carbon nanotubes. *Applied Physics Letters*, 77(9):1313–1315, 2000.

[155] F. Fugaciu, H. Hermann, and G. Seifert. Concentric-shell fullerenes and diamond particles: A molecular-dynamics study. *Phys. Rev. B*, 60:10711–10714, Oct 1999.

[156] A. Barnard and M. Sternberg. Crystallinity and surface electrostatics of diamond nanocrystals. *Journal of Materials Chemistry*, 17(45):4811–4819, 2007.

[157] A. S. Barnard, S. P. Russo, and I. K. Snook. Electronic band gaps of diamond nanowires. *Phys. Rev. B*, 68:235407, Dec 2003.

[158] A. Gali, E. Janzén, P. Deák, G. Kresse, and E. Kaxiras. Theory of spin-conserving excitation of the n-v-center in diamond. *Physical review letters*, 103(18):186404, 2009.

[159] A. Gali, E. Janzén, P. Deák, G. Kresse, and E. Kaxiras. Theory of spin-conserving excitation of the $n - V^-$ center in diamond. *Phys. Rev. Lett.*, 103:186404, Oct 2009.

[160] Y. Ma, M. Rohlfing, and A. Gali. Excited states of the negatively charged nitrogen-vacancy color center in diamond. *Physical Review B*, 81(4):041204, 2010.

[161] D. Le Sage, K. Arai, DR. Glenn, SJ. DeVience, LM. Pham, L. Rahn-Lee, MD. Lukin, A. Yacoby, A. Komeili, and RL. Walsworth. Optical magnetic imaging of living cells. *Nature*, 496(7446):486–489, 2013.

[162] AT. Collins, MF. Thomaz, and M. Jorge. Luminescence decay time of the 1.945 ev centre in type ib diamond. *Journal of Physics C: Solid State Physics*, 16(11):2177, 1983.

[163] J. Cai, A. Retzker, F. Jelezko, and M. Plenio. A large-scale quantum simulator on a diamond surface at room temperature. *Nature Physics*, 9(3):168–173, 2013.

[164] RUA. Khan, BL. Cann, PM. Martineau, J. Samartseva, JJP. Freeth, SJ. Sibley, CB. Hartland, ME. Newton, HK. Dhillon, and DJ. Twitchen. Colour-causing defects and their related optoelectronic transitions in single crystal cvd diamond. *Journal of Physics: Condensed Matter*, 25(27):275801, 2013.

[165] A. Mainwood. Nitrogen and nitrogen-vacancy complexes and their formation in diamond. *Phys. Rev. B*, 49:7934–7940, Mar 1994.

[166] A. Collins and I. Kiflawi. The annealing of radiation damage in type ia diamond. *Journal of Physics: Condensed Matter*, 21(36):364209, 2009.

[167] G. Davies. Charge states of the vacancy in diamond. *Nature*, 269:498–500, 1977.

[168] JR. Rabeau, P. Reichart, G Tamanyan, DN Jamieson, S Prawer, F Jelezko, T Gaebel, I Popa, M Domhan, and J Wrachtrup. Implantation of labelled single nitrogen vacancy centers in diamond using 15 n. *Applied Physics Letters*, 88(2):023113–023113, 2006.

[169] S. Pezzagna, B. Naydenov, F. Jelezko, J. Wrachtrup, and J. Meijer. Creation efficiency of nitrogen-vacancy centres in diamond. *New Journal of Physics*, 12(6):065017, 2010.

[170] V. M. Acosta, E. Bauch, M. P. Ledbetter, C. Santori, K.-M. C. Fu, P. E. Barclay, R. G. Beausoleil, H. Linget, J. F. Roch, F. Treussart, S. Chemerisov, W. Gawlik, and D. Budker. Diamonds with a high density of nitrogen-vacancy centers for magnetometry applications. *Phys. Rev. B*, 80:115202, Sep 2009.

[171] EB. Lombardi, A. Mainwood, K. Osuch, and EC Reynhardt. Computational models of the single substitutional nitrogen atom in diamond. *Journal of Physics: Condensed Matter*, 15(19):3135, 2003.

[172] H. Pinto, R. Jones, DW. Palmer, JP. Goss, and S. Briddon, PR .and Öberg. On the diffusion of nv defects in diamond. *physica status solidi (a)*, 209(9):1765–1768, 2012.

[173] JP. Goss, PR. Briddon, R. Jones, and S. Sque. Donor and acceptor states in diamond. *Diamond and related materials*, 13(4):684–690, 2004.

[174] S. J. Breuer and P. R. Briddon. Ab initio. *Phys. Rev. B*, 51:6984–6994, Mar 1995.

[175] BJ. Coomer, A. Resende, JP. Goss, R. Jones, S. Öberg, and PR. Briddon. The divacancy in silicon and diamond. *Physica B: Condensed Matter*, 273:520–523, 1999.

[176] R. Jones, PR. Briddon, and S. Öberg. First-principles theory of nitrogen aggregates in diamond. *Philosophical magazine letters*, 66(2):67–74, 1992.

[177] F. Fuchs, J. Furthmüller, F. Bechstedt, M. Shishkin, and G. Kresse. Quasiparticle band structure based on a generalized kohn-sham scheme. *Phys. Rev. B*, 76:115109, Sep 2007.

[178] J. Heyd, G. E Scuseria, and M. Ernzerhof. Hybrid functionals based on a screened coulomb potential. *The Journal of Chemical Physics*, 118(18):8207–8215, 2003.

[179] P. Deák, B. Aradi, T. Frauenheim, E. Janzén, and A. Gali. Accurate defect levels obtained from the hse06 range-separated hybrid functional. *Phys. Rev. B*, 81:153203, Apr 2010.

[180] G. Mills, H. Jónsson, and G. Schenter. Reversible work transition state theory: application to dissociative adsorption of hydrogen. *Surface Science*, 324(2):305–337, 1995.

[181] S. Lany and A. Zunger. Many-body *gw* calculation of the oxygen vacancy in zno. *Phys. Rev. B*, 81:113201, Mar 2010.

[182] J. Koppitz, OF. Schirmer, and M. Seal. Pseudo-jahn-teller optical absorption of isolated nitrogen in diamond. *Journal of Physics C: Solid State Physics*, 19(8):1123, 1986.

[183] CE. Nebel, R. Zeisel, and M. Stutzmann. Space charge spectroscopy of diamond. *Diamond and related materials*, 10(3):639–644, 2001.

[184] P. Muret, J.ulien Pernot, T. Teraji, and T. Ito. Deep levels in homoepitaxial boron-doped diamond films studied by capacitance and current transient spectroscopies. *physica status solidi (a)*, 205(9):2179–2183, 2008.

[185] JW. Steeds, SJ. Charles, J. Davies, and I. Griffin. Photoluminescence microscopy of tem irradiated diamond. *Diamond and Related Materials*, 9(3):397–403, 2000.

[186] E. Rohrer, C. F. O. Graeff, R. Janssen, C. E. Nebel, M. Stutzmann, H. Güttler, and R. Zachai. Nitrogen-related dopant and defect states in cvd diamond. *Phys. Rev. B*, 54:7874–7880, Sep 1996.

[187] T. Miyazaki, H. Okushi, and T. Uda. Shallow donor state due to nitrogen-hydrogen complex in diamond. *Phys. Rev. Lett.*, 88:066402, Jan 2002.

[188] G. Davies, S. Lawson, A. Collins, A. Mainwood, and S. Sharp. Vacancy-related centers in diamond. *Phys. Rev. B*, 46:13157–13170, Nov 1992.

[189] C. Glover, M. E. Newton, P. Martineau, D. J. Twitchen, and J. M. Baker. Hydrogen incorporation in diamond: The nitrogen-vacancy-hydrogen complex. *Phys. Rev. Lett.*, 90:185507, May 2003.

[190] T. Yamamoto, S. Onoda, T. Ohshima, T. Teraji, K. Watanabe, S. Koizumi, T. Umeda, L. P. McGuinness, C. Müller, B. Naydenov, F. Dolde, H. Fedder, J. Honert, M. L. Markham, D. J. Twitchen, J. Wrachtrup, F. Jelezko, and J. Isoya. Isotopic identification of engineered nitrogen-vacancy spin qubits in ultrapure diamond. *Phys. Rev. B*, 90:081117, Aug 2014.

[191] J. Lomer and A. Wild. Electron spin resonance in electron irradiated diamond annealed to high temperatures. *Radiation Effects*, 17(1-2):37–44, 1973.

[192] G. Davies. *Properties and growth of diamond*. INSPEC, the Institution of Electrical Engineers, 1994.

[193] K. Iakoubovskii and A. Stesmans. Dominant paramagnetic centers in ^{17}O-implanted diamond. *Phys. Rev. B*, 66:045406, Jul 2002.

[194] B. Naydenov, F. Reinhard, A. Lammle, V. Richter, R. Kalish, U. DHaenens-Johansson, M. Newton, F. Jelezko, and J. Wrachtrup. Increasing the coherence time of single electron spins in diamond by high temperature annealing. *Applied Physics Letters*, 97(24):242511–242511, 2010.

[195] T. Yamamoto, T. Umeda, K. Watanabe, S. Onoda, M. L. Markham, D. J. Twitchen, B. Naydenov, L. P. McGuinness, T. Teraji, S. Koizumi, F. Dolde, H. Fedder, J. Honert, J. Wrachtrup, T. Ohshima, F. Jelezko, and J. Isoya. Extending spin coherence times of diamond qubits by high-temperature annealing. *Phys. Rev. B*, 88:075206, Aug 2013.

[196] MV. Hauf, B. Grotz, B. Naydenov, M. Dankerl, S. Pezzagna, J. Meijer, F. Jelezko, J. Wrachtrup, M. Stutzmann, F. Reinhard, et al. Chemical control of the charge state of nitrogen-vacancy centers in diamond. *Physical Review B*, 83(8):081304, 2011.

[197] A. Ermakova, G. Pramanik, J-M Cai, G. Algara-Siller, U. Kaiser, T. Weil, Y-K Tzeng, H. Chang, L. McGuinness, M. Plenio, et al. Detection of a few metallo-protein molecules using color centers in nanodiamonds. *Nano letters*, 13(7):3305–3309, 2013.

[198] F. Ziem, N. Gotz, A. Zappe, S. Steinert, and J. Wrachtrup. Highly sensitive detection of physiological spins in a microfluidic device. *Nano letters*, 13(9):4093–4098, 2013.

[199] T. Staudacher, F. Shi, S. Pezzagna, J. Meijer, J. Du, CA. Meriles, F. Reinhard, and J. Wrachtrup. Nuclear magnetic resonance spectroscopy on a (5-nanometer) 3 sample volume. *Science*, 339(6119):561–563, 2013.

[200] HJ. Mamin, M. Kim, MH. Sherwood, CT. Rettner, K. Ohno, DD. Awschalom, and D. Rugar. Nanoscale nuclear magnetic resonance with a nitrogen-vacancy spin sensor. *Science*, 339(6119):557–560, 2013.

[201] M. Grinolds, S. Hong, P. Maletinsky, L. Luan, M. Lukin, R. Walsworth, and A. Yacoby. Nanoscale magnetic imaging of a single electron spin under ambient conditions. *Nature Physics*, 9(4):215–219, 2013.

[202] J. Wrachtrup, S. Kilin, and AP. Nizovtsev. Quantum computation using the 13c nuclear spins near the single nv defect center in diamond. *Optics and Spectroscopy*, 91(3):429–437, 2001.

[203] RJ. Epstein, FM. Mendoza, YK. Kato, and DD. Awschalom. Anisotropic interactions of a single spin and dark-spin spectroscopy in diamond. *Nature Physics*, 1(2):94–98, 2005.

[204] F. Jelezko, I. Popa, A. Gruber, C. Tietz, J. Wrachtrup, A. Nizovtsev, and S. Kilin. Single spin states in a defect center resolved by optical spectroscopy. *Applied physics letters*, 81(12):2160–2162, 2002.

[205] F. Jelezko, T. Gaebel, I. Popa, A. Gruber, and J. Wrachtrup. Observation of coherent oscillations in a single electron spin. *Phys. Rev. Lett.*, 92:076401, Feb 2004.

[206] F. Jelezko, T. Gaebel, I. Popa, M. Domhan, A. Gruber, and J. Wrachtrup. Observation of coherent oscillation of a single nuclear spin and realization of a two-qubit conditional quantum gate. *Phys. Rev. Lett.*, 93:130501, Sep 2004.

[207] B. K. Ofori-Okai, S. Pezzagna, K. Chang, M. Loretz, R. Schirhagl, Y. Tao, B. A. Moores, K. Groot-Berning, J. Meijer, and C. L. Degen. Spin properties of very shallow nitrogen vacancy defects in diamond. *Phys. Rev. B*, 86:081406, Aug 2012.

[208] B. Grotz, M. Hauf, M. Dankerl, B. Naydenov, S. Pezzagna, J. Meijer, F. Jelezko, J. Wrachtrup, M. Stutzmann, F. Reinhard, et al. Charge state manipulation of qubits in diamond. *Nature communications*, 3:729, 2012.

[209] F. Maier, J. Ristein, and L_ Ley. Electron affinity of plasma-hydrogenated and chemically oxidized diamond (100) surfaces. *Physical Review B*, 64(16):165411, 2001.

[210] K. Rietwyk, SL. Wong, L. Cao, KM. O'Donnell, L. Ley, A. Wee, and CI. Pakes. Work function and electron affinity of the fluorine-terminated (100) diamond surface. *Applied Physics Letters*, 102(9):091604, 2013.

[211] C. Bradac, T. Gaebel, C. Pakes, J. Say, A. Zvyagin, J. Rabeau, et al. Effect of the nanodiamond host on a nitrogen-vacancy color-centre emission state. *Small*, 9(1):132–139, 2013.

[212] K. Ohashi, T. Rosskopf, H. Watanabe, M. Loretz, Y. Tao, R. Hauert, S. Tomizawa, T. Ishikawa, J. Ishi-Hayase, S. Shikata, et al. Negatively charged nitrogen-vacancy centers in a 5 nm thin 12c diamond film. *Nano letters*, 13(10):4733–4738, 2013.

[213] F. Fuchs, J. Furthmüller, F. Bechstedt, M. Shishkin, and G. Kresse. Quasiparticle band structure based on a generalized kohn-sham scheme. *Physical Review B*, 76(11):115109, 2007.

[214] A. Krukau, O. Vydrov, A. Izmaylov, and G. Scuseria. Influence of the exchange screening parameter on the performance of screened hybrid functionals. *The Journal of chemical physics*, 125(22):224106, 2006.

[215] S. J. Sque, R. Jones, and P. R. Briddon. Structure, electronics, and interaction of hydrogen and oxygen on diamond surfaces. *Phys. Rev. B*, 73:085313, Feb 2006.

[216] P. Pehrsson and T. Mercer. Oxidation of the hydrogenated diamond (100) surface. *Surface science*, 460(1):49–66, 2000.

[217] M. Rohlfing, N. Wang, P. Krüger, and J. Pollmann. Image states and excitons at insulator surfaces with negative electron affinity. *Physical review letters*, 91(25):256802, 2003.

[218] P. Siyushev, H. Pinto, M. Vörös, A. Gali, F. Jelezko, and J. Wrachtrup. Optically controlled switching of the charge state of a single nitrogen-vacancy center in diamond at cryogenic temperatures. *Physical review letters*, 110(16):167402, 2013.

[219] F. Maier, J. Ristein, and L. Ley. Electron affinity of plasma-hydrogenated and chemically oxidized diamond (100) surfaces. *Phys. Rev. B*, 64:165411, Oct 2001.

[220] FA. Inam, AM. Edmonds, MJ. Steel, and S. Castelletto. Tracking emission rate dynamics of nitrogen vacancy centers in nanodiamonds. *Applied Physics Letters*, 102(25):253109, 2013.

[221] P. Deák, B. Aradi, T. Frauenheim, E. Janzén, and A. Gali. Accurate defect levels obtained from the hse06 range-separated hybrid functional. *Physical Review B*, 81(15):153203, 2010.

[222] P. M. Fahey, P. B. Griffin, and J. D. Plummer. Point defects and dopant diffusion in silicon. *Rev. Mod. Phys.*, 61:289–384, Apr 1989.

[223] K. Weiser. Theory of diffusion and equilibrium position of interstitial impurities in the diamond lattice. *Phys. Rev.*, 126:1427–1436, May 1962.

[224] M. Depas, B. Vermeire, PW. Mertens, RL. Van Meirhaeghe, and MM. Heyns. Determination of tunnelling parameters in ultra-thin oxide layer poly-si/sio¡ sub¿ 2¡/sub¿/si structures. *Solid-state electronics*, 38(8):1465–1471, 1995.

[225] Tzu-Liang Chan and James R Chelikowsky. Controlling diffusion of lithium in silicon nanostructures. *Nano letters*, 10(3):821–825, 2010.

[226] Fedor Jelezko, T Gaebel, I Popa, M Domhan, A Gruber, and Jorg Wrachtrup. Observation of coherent oscillation of a single nuclear spin and realization of a two-qubit conditional quantum gate. *Physical Review Letters*, 93(13):130501, 2004.

[227] R Hanson, FM Mendoza, RJ Epstein, and DD Awschalom. Polarization and readout of coupled single spins in diamond. *Physical review letters*, 97(8):087601, 2006.

[228] Amanda S Barnard. Optimal vacancy concentrations to maximize the n–v yield in nanodiamonds. *Materials Horizons*, 1(2):286–291, 2014.

[229] G. Kresse and J. Hafner. Ab initio molecular-dynamics simulation of the liquid-metal–amorphous-semiconductor transition in germanium. *Physical Review B*, 49(20):14251, 1994.

[230] Peter E Blöchl. Projector augmented-wave method. *Physical Review B*, 50(24):17953, 1994.

[231] SJ. Breuer and PR. Briddon. Ab initio investigation of the native defects in diamond and self-diffusion. *Physical Review B*, 51(11):6984, 1995.

[232] J. Bernholc, TM. Antonelli, A .and Del Sole, Y. Bar-Yam, and ST. Pantelides. Mechanism of self-diffusion in diamond. *Physical review letters*, 61(23):2689, 1988.

List of Publications

1. Moloud Kaviani, Peter Deák, Bálint Aradi, Thomas Köhler, and Thomas Frauenheim. *How small nanodiamonds can be? MD study of the stability against graphitization.* Diamond and Related Materials 33 (2013): 78-84.

2. Peter Deák, Bálint Aradi, Moloud Kaviani, Thomas Frauenheim, and Adam Gali. *Formation of NV centers in diamond: A theoretical study based on calculated transitions and migration of nitrogen and vacancy related defects.* Physical Review B 89, no. 7 (2014): 075203.

3. Moloud Kaviani, Peter Deák, Bálint Aradi, Thomas Frauenheim, Jyh-Pin Chou, and Adam Gali. *Proper Surface Termination for Luminescent Near-Surface NV Centers in Diamond.* Nano letters 14, no. 8 (2014): 4772-4777.

4. Moloud Kaviani, Thomas Frauenheim and Peter Deák. *Formation of NV-centers in nanodiamonds: nano-size effects on point defect diffusion.* In preparation.

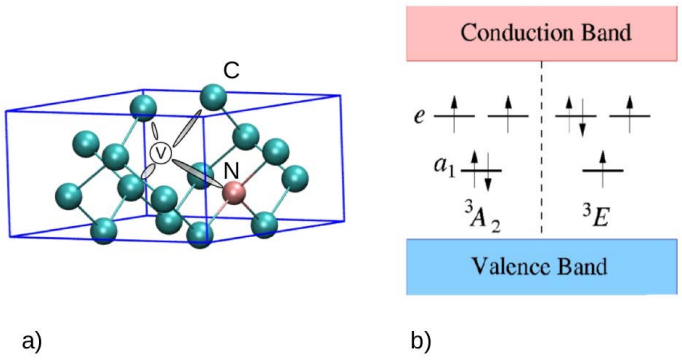

Figure 1.1: (a) Nitrogen-vacancy (NV) defect in diamond. (b) schematic diagram of the defect levels for the negatively charged NV defect; left panel: ground state, right panel: excited state [9]

enough to serve as a predictive tool for characterizing and identifying the defects. Among various *ab initio* techniques, density functional theory (DFT) has become widespread over the last two decades. In the present study, DFT has been used as the computational tool for studying various aspects of defects such as optical and electronic properties.

In the next two sections, the material and the defects for which some of their properties are going the be studied, are introduced. Their fabrication methods and their applications will be named.

1.2 Nitrogen-Vacancy center in diamond

Diamond is known for its excessive hardness and high thermal conductivity. Diamond is an electronic insulator with a wide bandgap of 5.48 eV [11] and is optically transparent in the visible regime. It can host a lot of different point defect centers, called color centers, that emit light. A particular defect which has acquired great importance lately is the NV (nitrogen-vacancy) center in diamond. In the NV-center a nitrogen atom substitutes a carbon atom next to a vacancy (see Fig. 1.1a) oriented along the (111) crystalline direction. The NV-centre can be found as an "in grown" product of the chemical vapour deposition (CVD) in diamond synthesis process [12] or as a product of radiation damage with energetic neutrons, electrons, or ions [13, 14] and annealing [15] or ion implantation and annealing [16] in bulk and nanocrystalline diamond [17].

possible, in order to be compatible with the size of typical biological molecules. This has been recently realized either by a milling process [15] or by a detonation method [69, 70]. It is important to note that detonation NDs were cleaned using strong oxidizing acids [51, 53, 71, 72] which remove the graphitic shells and produce more "active" fluorescent NV centers [53, 73]. Furthermore, according to an *ab initio* study, for nanodiamonds larger than 3 nm in diameter (d), surface reconstructed nanodiamonds are favorable over hydrogenated nanocrystallites even in the presence of hydrogen [74, 75].

Surface reconstruction will minimize the surface energy and reduce the number of dangling bonds of the carbon atoms on the surface. The carbon atoms on the unreconstructed surface have two dangling bonds. This surface can go through a 2×1 reconstruction after relaxation (see Fig. 1.3a) where neighboring atoms on the surface form π-bonded dimers. In the case of hydrogenated surface, π-bond between the dimers is replaced by a covalent bond to the hydrogen (see Fig. 1.3b) [76]. The hydroxyl groups also relax to a (100):2×1 reconstruction (see Fig. 1.3c) [77–79]. With terminating the surface, all of the surface carbon atoms get sp^3-bonded structure but sometimes some of these sp^3 bonds break under annealing and graphitization may occur. Studies have shown that the surface is stable around 1800°C in vacuum and around 800°C in presence of oxygen [80]. Above these temperatures surface goes through graphitization.

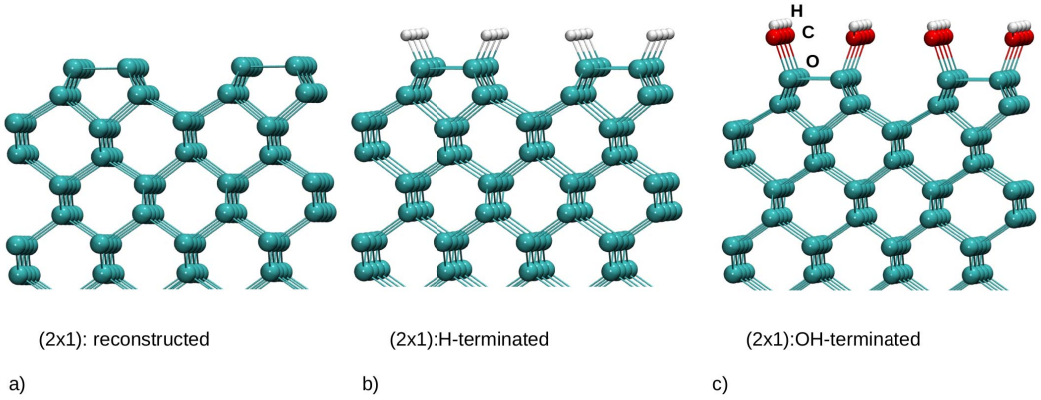

Figure 1.3: Optimized atomic geometries for the a) clean, b) hydrogenated, c) hydroxylated (001):2×1 reconstructed diamond surfaces.

Very recently it has been reported [53] that by careful chemical treatment of aggregated detonation nanodiamonds, one can realize isolated nanodiamonds with d<5 nm in colloid solution,

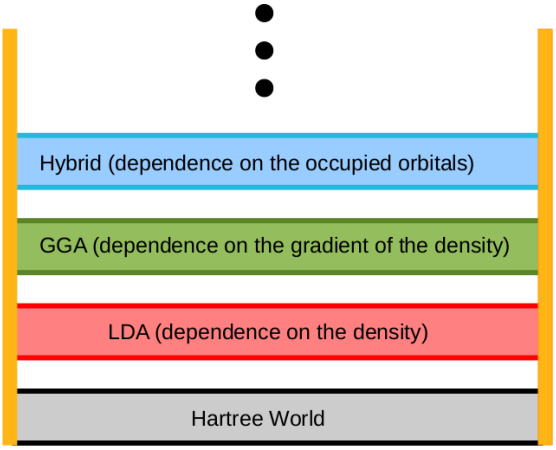

Figure 2.1: Jacob's ladder.

the exchange-correlation energy obtained from the uniform electron gas (UEG) for each of the densities. The total exchange-correlation energy of a spin-unpolarized system is:

$$E_{XC}^{LDA}[n] = \int n(r)\varepsilon_{XC}^{unif}(n(r))dr. \tag{2.17}$$

where ε_{XC}^{unif} is the exchange-correlation energy per particle of the interacting uniform electron gas with density n(r). For calculating the exchange-correlation energy the exchange and the correlation parts are calculated separately.

$$\varepsilon_{XC}^{unif} = \varepsilon_{X}^{unif} + \varepsilon_{C}^{unif} \tag{2.18}$$

The exchange energy for systems with inhomogeneous density is obtained by applying the UEG results pointwise

$$E_{X}^{LDA}[n] = -\frac{3}{4}(3\pi)^{1/3}\int n^{\frac{4}{3}}(r)dr. \tag{2.19}$$

The correlation part is complicated. It is generally obtained by fitting to the many-body results, as in the works of Gell-Mann and Brueckner and Ceperly and Alder [91, 92]. The LDA functionals which are used recently are getting much more simple. The difference between these functionals are only in how their correlation contributions have been fitted to the many-body free

arising structures. In the MD simulations, carried out under NVT condition with the canonical ensemble numerically realized by the Anderson thermostat, we applied the temperature program shown in Fig.3.1.

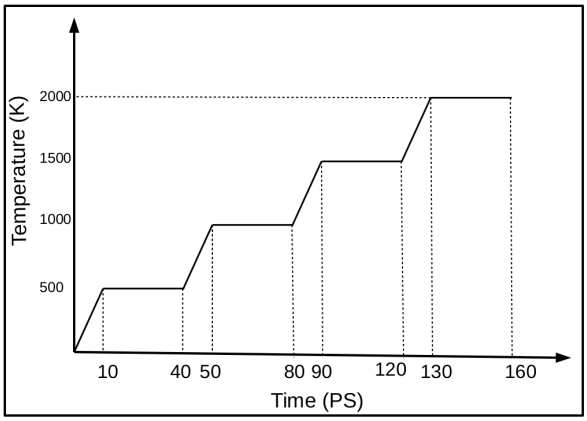

Figure 3.1: Temperature program of the annealing.

In a few cases, intermediate temperatures were also considered (always preceded and followed by 10 ps ramps). The time step for integrating the equations of motion was 2 fs. The clusters were put in a cubic vacuum box of the size l = 500 Å, to prevent interaction between periodically repeated images. The isothermal annealing time was chosen to be 30 ps, more by necessity than choice. Obviously, at low temperatures this is not sufficient to achieve thermal equilibration. However, tests at 1500 K up to 250 ps indicate that the results after 30 ps are already close to that. We have monitored the graphitization process by means of the percentage of purely sp^2, sp^3 and $sp^{(2+x)}$ bonded atoms with respect to the total number of carbon atoms. (These bonding configurations are defined here as follows: sp^2 means threefold coordinated, all of the atoms are in a plane with bond angles around 120 degree. sp^3 means fourfold coordinated in tetrahedral arrangement with bond angles around 109 degrees, and $sp^{(2+x)}$ means threefold coordinated but one of the neighbors is out of the plane.) The contribution of twofold and singly coordinated carbons will not be displayed. For the purpose of this work, we have considered the equality between the percentage of sp^2 and sp^3-bonded carbon as the "graphitization point", although the expression "amorphization point" could have been more appropriate. We note, that in the presence of oxygen, CO_x species are formed on the surface and they dissociate from it partly or

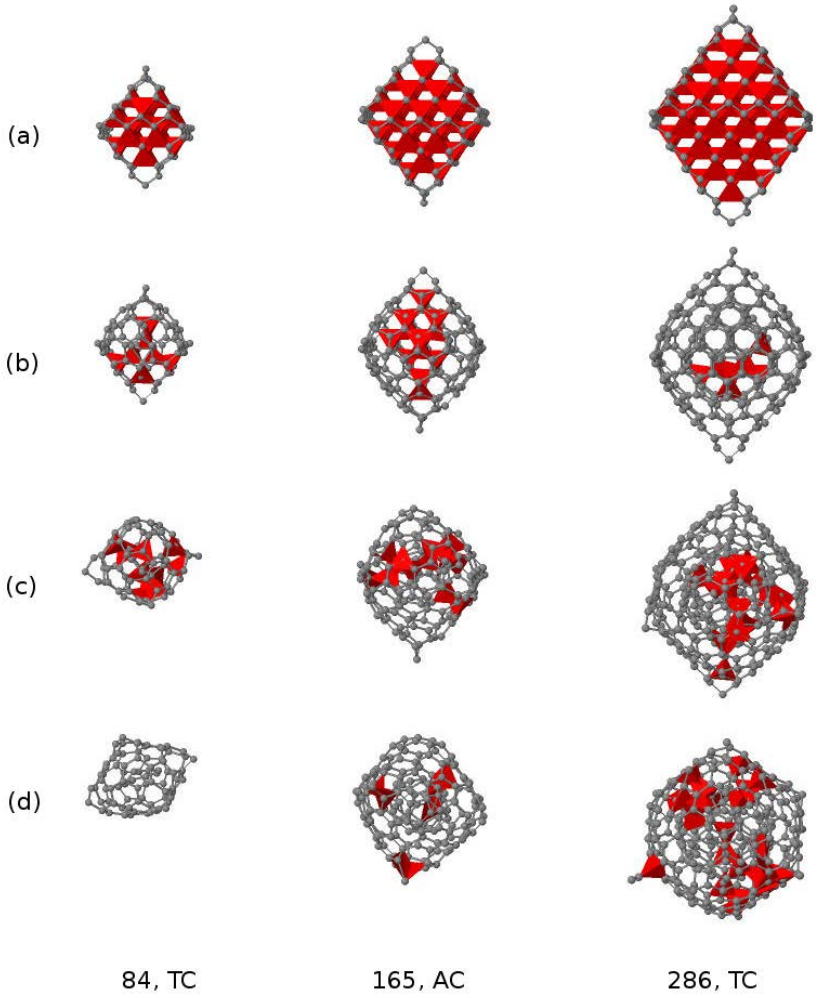

Figure 3.2: Structure of octahedral clusters. (a) unrelaxed (initial), (b) relaxed, (c) after annealing in vacuum up to 1500 K and (d) after 160 ps at 2000 K. The carbon atoms are illustrated with grey spheres, and atoms with sp^3 hybridization are shown as red polyhedra.

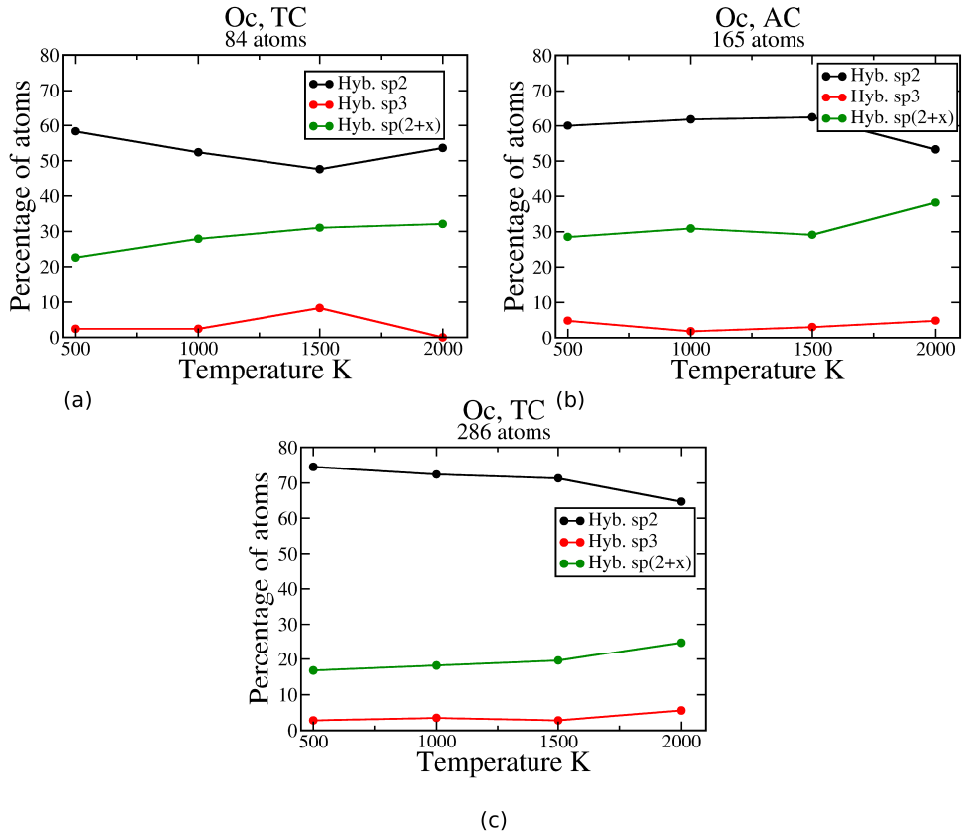

Figure 3.3: Structure evolution of the octahedral clusters upon vacuum annealing. (a) 84 atoms, (b) 165 atoms and (c) 286 atoms.

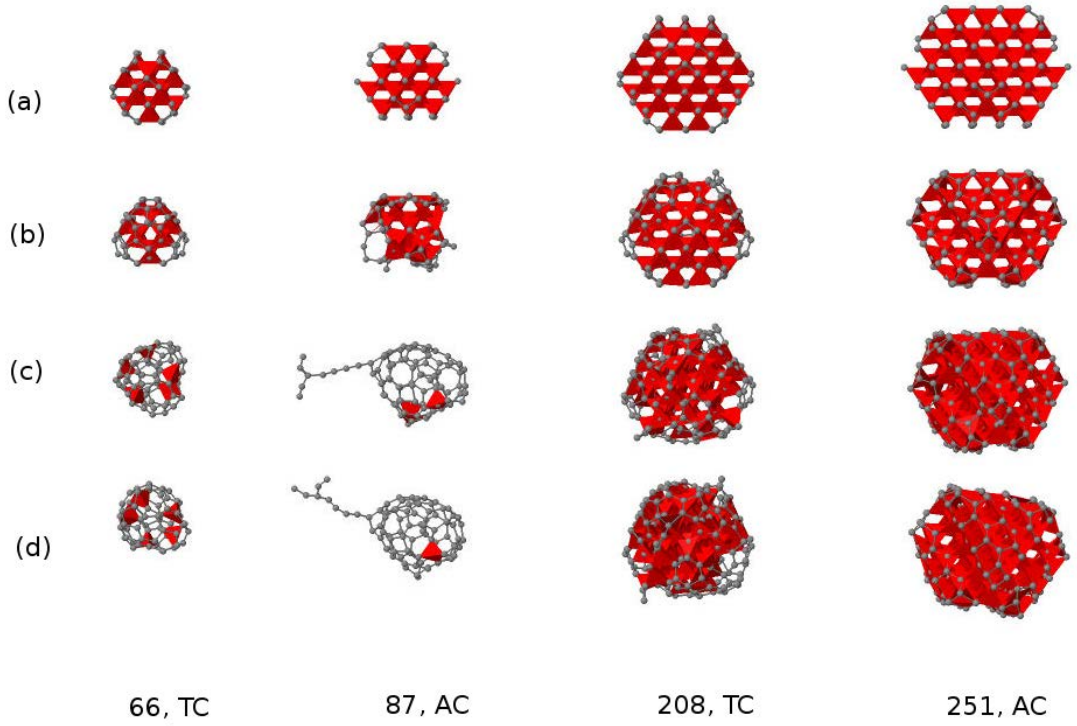

Figure 3.4: Structure of cuboctahedral clusters. (a) unrelaxed (initial), (b) relaxed, (c) after annealing in vacuum up to 1500 K and (d) after 160 ps in 2000 K.

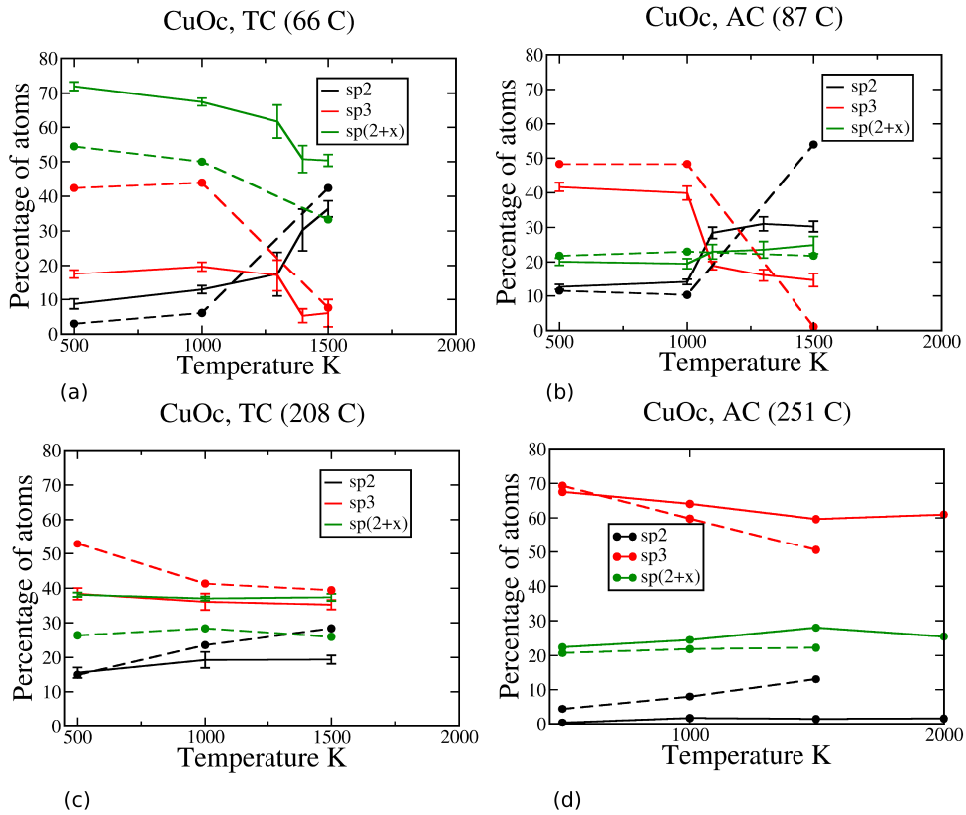

Figure 3.5: Structural evolution of the cuboctahedral clusters upon annealing in vacuum (solid lines) and in oxygen (dashed lines). (a) 66 atoms, (b) 87 atoms, (c) 208 atoms and (d) 251 atoms. Data points for the vacuum anneal represent the average of four independent annealing cycles, starting from the same ideal structure. Error bars depict the root mean square of the deviations from the average in the four runs.

in Fig. 3.6, larger clusters even above 1500 K.

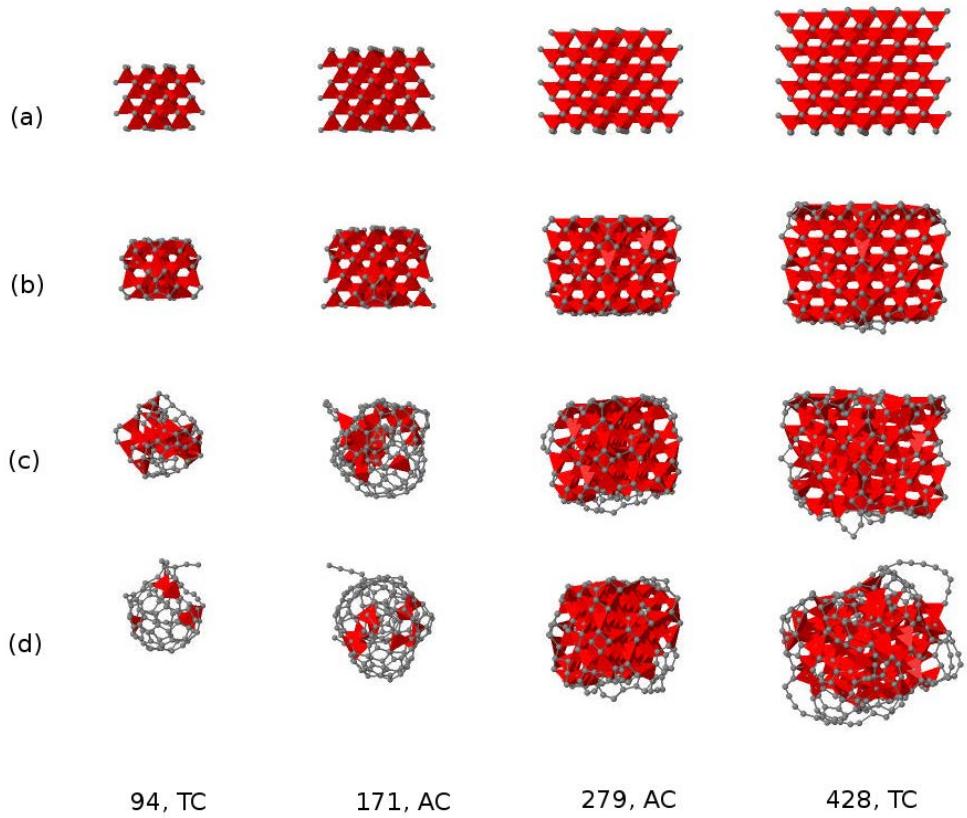

Figure 3.6: Structure of cube-shaped clusters. (a) unrelaxed (initial) structures, (b) relaxed structures, (c) after annealing in vacuum up to 1500 K and (d) after 160 ps in 2000 K.

Fig. 3.7 shows the structural evolution of the cube-shaped clusters with temperature. For clusters below 200 atoms the "graphitization temperature" is between 1400-1600 K (for short annealing times), significantly higher than for the cuboctahedral clusters. In larger clusters "graphitization" occurs only in short annals at very high temperatures (∼2500 K). We have continued the 1500 K anneal for the AC 279 cluster, up to 250 ps. As shown in Fig. 3.8, the 1500 K data point in Fig. 3.7 (at 30 ps) was already close to equilibration. Therefore, these clusters can survive realistic annealing times at 1500 K.

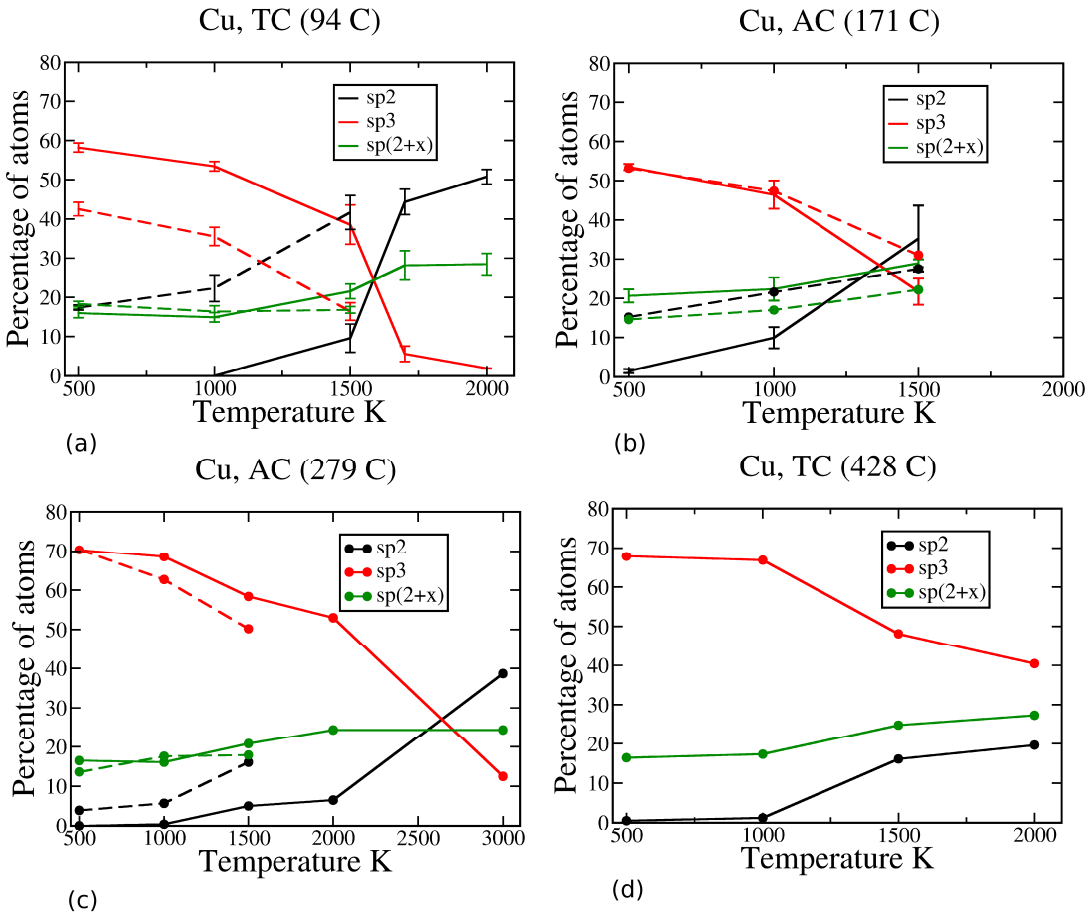

Figure 3.7: Structural evolution of the cube-shaped clusters upon annealing in vacuum (solid lines) and in oxygen (dashed lines). (a) 94 atoms, (b) 171 atoms, (c) 279 atoms and (d) 428 atoms. (N.B.: for small percentages the error bar is too small to be seen.

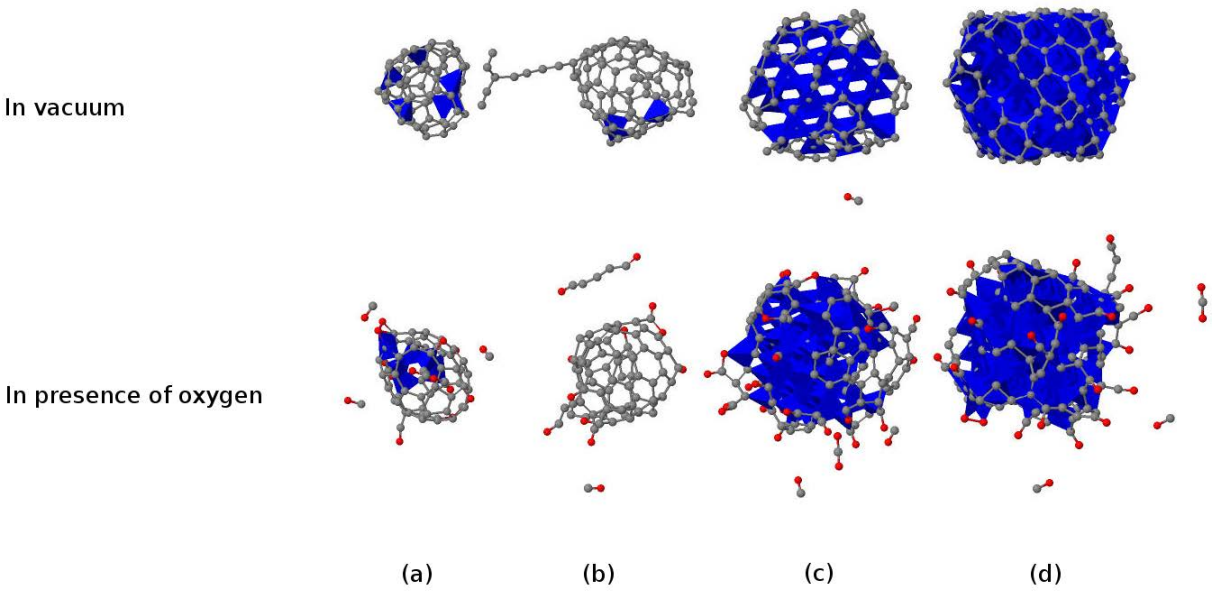

Figure 3.9: Structure of cuboctahedral clusters at 1500 K in vacuum and in presence of O_2. Clusters of (a) TC 66 (b) AC 87 (c) TC 208 and (d) AC 251 carbon atoms. Grey and red spheres represent carbon and oxygen atoms, respectively. Carbon atoms with sp^3 hybridization are shown as blue polyhedra.

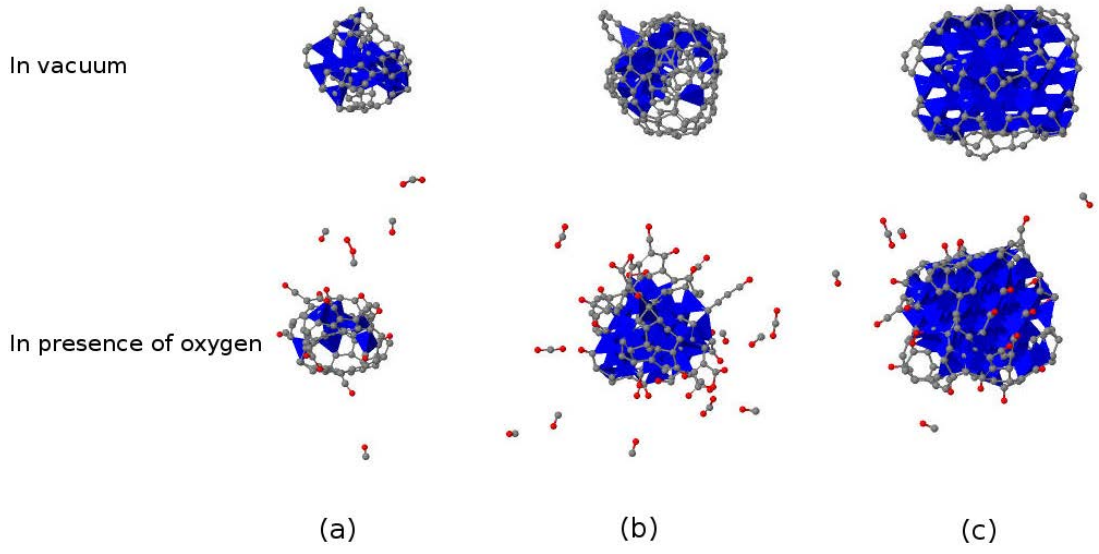

Figure 3.10: Structure of cube-shaped clusters at 1500 K in vacuum and in presence of O_2. Clusters of (a) TC 94 , (b) AC 171, and (c) AC 279 carbon atoms.

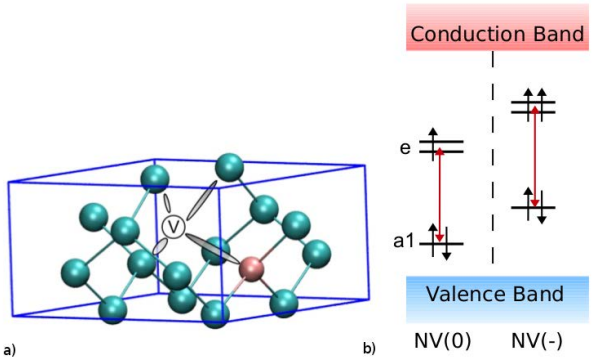

Figure 4.1: Nitrogen-vacancy (NV) defect in bulk diamond. a) Schematic picture of the geometry of the NV-defect. b) Levels of this defect in the band gap in the neutral and in the negatively charged state. The excitation (de-excitation) from (to) the $a1$ level to(from) the e level is responsible for the absorption(emission) of the neutral and negatively charged defects.

quantum optics protocols that can be applied to sense magnetic [35, 36] and electric fields [38], or temperature [39–41] at atomic scale. It has been recently proposed that NV(-) defects may realize a large-scale quantum simulator on the diamond surface operating at room temperature [163].

NV(-) can be routinely found in natural Type Ib diamonds, but generally, the concentration of NV natural or as-grown synthetic diamonds is very low for applications [164]. The concentration of NV can be substantially increased by creating vacancies in N-doped diamond by irradiation with energetic neutrons, electrons, or ions [13, 165], followed by annealing above ~ 600°C, where vacancies become mobile [20, 166]. According to the present consensus in the literature, mobile vacancies can get trapped by substitutional nitrogen (N_s) and form NV centers [167–170]. Understanding the formation of NV defects requires accurate knowledge about the formation energy of the isolated constituents, N_s and the vacancy (V), and about competing defect complexes (NV, N_2V, V_2, NVH). The mobility of the species and the energy of complex formation may depend on the charge states; thus, it is highly critical to determine the charge transition levels of these defects across the band gap. Since diamond is a wide gap material, it is extremely difficult (or sometimes impossible) to determine deep adiabatic (thermal) charge transition levels by traditional techniques such as deep-level transient spectroscopy (DLTS). The vertical ionization energies may be obtained by optical excitation of the samples, but it is not

and charge state of this defect is required. However, these depend on the concentration of other defects. Assuming equilibrium conditions, the calculated formation energies allow us to predict the relative concentrations in different charge states by solving the neutrality equation, considering all defects i, with charge q_i,

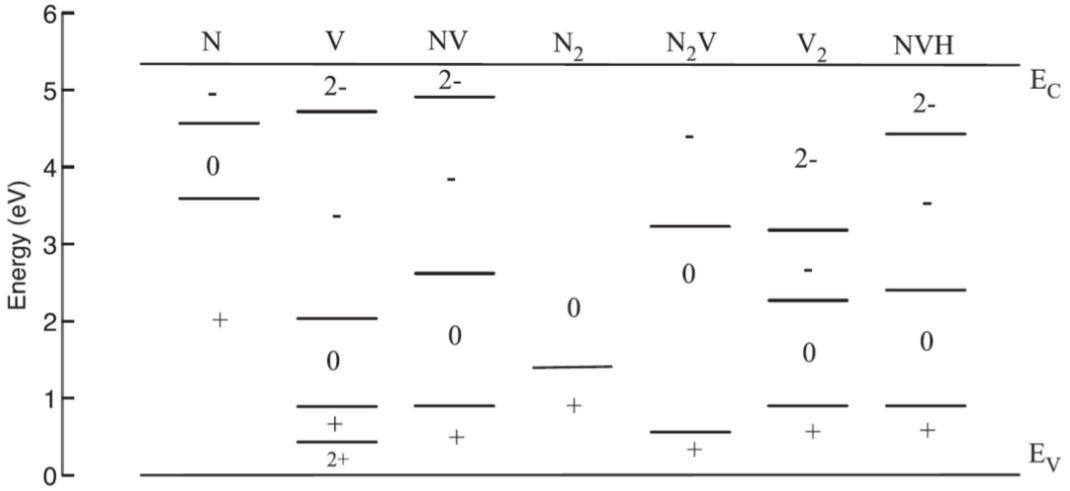

Figure 4.3: Comparison of the adiabatic charge transition levels.

$$\begin{aligned} &N_C exp[-\frac{E_C - E_F}{kT}] + \sum_i |q_i|(N_{Ai} - p_{Ai}) \\ &= N_V exp[-\frac{E_F - E_V}{kT}] + \sum_i |q_i|(N_{Di} - n_{Di}) \end{aligned} \tag{4.3}$$

where

$$N_C = 2(\frac{2m_e^* \pi kT}{h^2})^{3/2}; N_V = 2(\frac{2m_h^* \pi kT}{h^2})^{3/2} \tag{4.4}$$

are the effective (number) densities of states in the conduction and valence band of diamond, calculated from the density-ofstates mass of the electrons, $m_e^* = 0.57m_0$, and the holes, $m_h^* = 0.8m_0$, respectively. The remaining terms in Eq. 4.3 are the occupancies of the acceptor and donor levels, determined by the Fermi-Dirac distribution and the degeneracy factors g

$$\begin{aligned} p_{Ai} &= N_{Ai}[g_{Ai} exp(\frac{E_F - E_{Ai}}{kT}) + 1]^{-1}; \\ n_{Di} &= N_{Di}[g_{Di} exp(\frac{E_{Di} - E_F}{kT}) + 1]^{-1} \end{aligned} \tag{4.5}$$

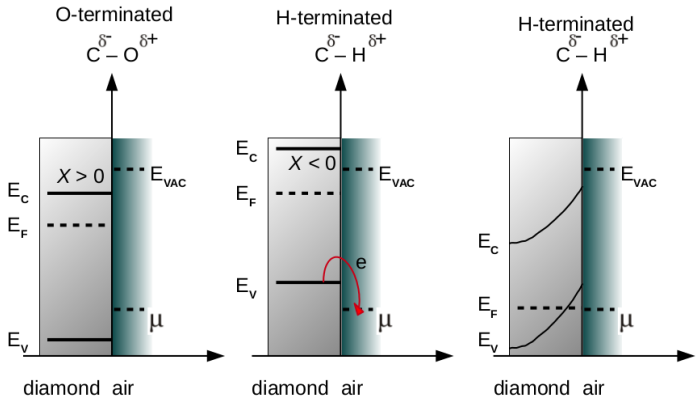

Figure 5.1: Energy-band scheme of diamond. (a) O-terminated diamond: The conduction band E_C lies below the vacuum level E_{VAC} (electron affinity $\chi > 0$ eV). The NV- level lies beneath the Fermi level E_F , where the position is mainly determined by the bulk concentration of nitrogen. (b) H-terminated diamond: The bands are shifted upward by the hydrogen termination ($\chi < 0$ eV). Electrons can transfer into acceptor states μ of an adsorbed water layer. Surface band-bending in H-terminated surfaces results in surface conductivity. [77, 196].

of the negative electron affinity (NEA), the conduction and valence bands of hydrogenated diamond bend upward at the surface at ambient conditions, so, except for heavy n-type doping, the Fermi-level will shift below the acceptor level of the NV-defect, and NV(0) will dominantly appear [72]. Oxidation removes this bending, and luminescent NV(-) defects also appear beside NV(0) [72, 81]. In fluorinated surface diamonds further enhancement of the luminescent NV(-) to NV(0) ratio was observed [27]. This band-bending model was applied to explain the enhanced NV(-) to NV(0) ratio in larger nanodiamonds after oxygenation [42], however, we note that it does not explain all the features of the NV center near the diamond surface. For instance, intermittency in fluorescence, i.e. blinking, was detected in nanodiamonds of 5 nm in diameter [53] where the concept of solid state bands is strictly not valid any more, so acceptor states should play a role in this process [211]. In a recent study, 30% of the NV($-$) centers engineered $5-2$ nm beneath the F-terminated diamond surface showed permanent bleaching. [212] Since F-termination of diamond leads to a PEA surface [210], a band-bending model cannot account for such a bleaching behavior of the NV(-) defects. Blinking or bleaching is detrimental for NV-based nanoscale sensing based on the intrinsic ODMR signal of the NV-defect, so it is of immediate and high interest to explore the properties of the diamond surfaces, in order to be

perpendicular to the surface is calculated. Next, The bulk-like occupied (VBM) and unoccupied (CBM) (see .5.3a) bands by plotting the charge density of the bands are identified. Finally, I obtained the electron-affinity of the system as the energy difference of the vacuum level and the calculated conduction band minimum. The electron affinity for the hydrogen terminated surface is calculated to be χ = -1.7 eV (see Fig. 5.3a), in fairly good agreement with the experimental value (-1.90 eV)[209]. By looking at the electronic structure I find that the hydrogen termination introduces deep, sub-bandgap states that are surface-related (see Fig. 5.3b and c).

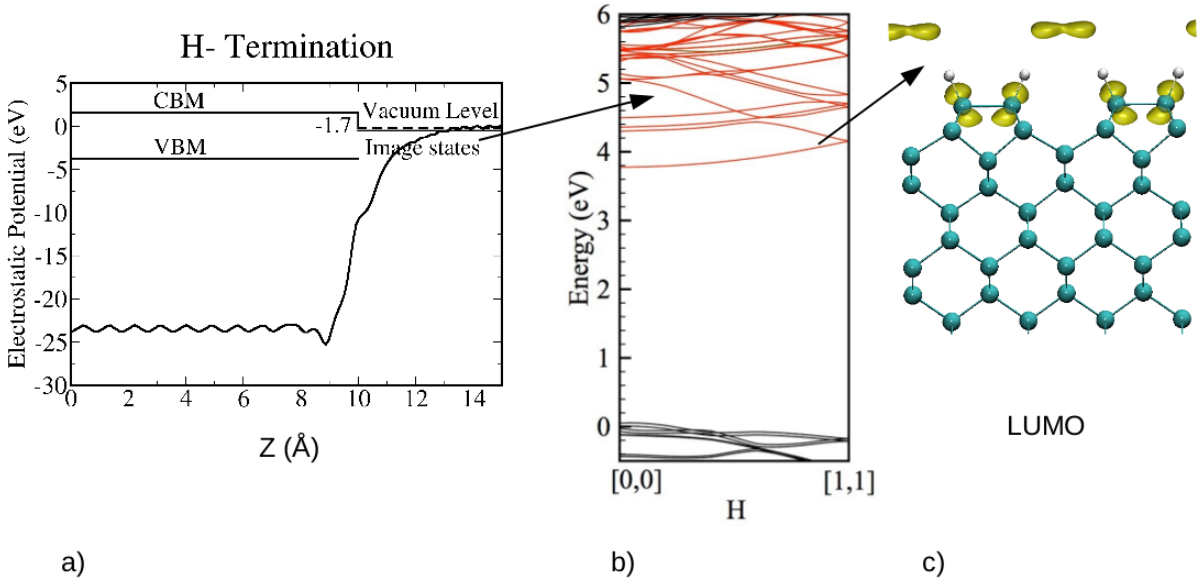

Figure 5.3: a) the calculated average potential vs. the z coordinate is plotted, where the z coordinate is the direction perpendicular to the surface. z=0.0$\mathring{A}$ corresponds to the middle of the slab. The electron-affinity is given in eV unit. b) The calculated HSE06 band structure of the (001) diamond H-terminationed surface along (110) direction in the Brillouin zone. The results are shown for slab supercells, thus band folding appears in the band structure. Red colour represents image states. c) The corresponding charge density isosurface of the surface related states are depicted on the structures. (The NV defect is located at the middle of each structure which is not shown in the figures). Charge density isosurface is depicted at isovalue of 0.0029 e/Å^3.

These so-called image states are delocalized along the surface and show strong dispersion. Image states are known at other insulator surfaces with NEA [217]. As mentioned earlier, NEA can make NV defects neutral due to band-bending, however, this does not necessarily happen above a certain level of n-type doping [207]. Thus, both NV(0) (see Fig. 5.4a) and NV(-)

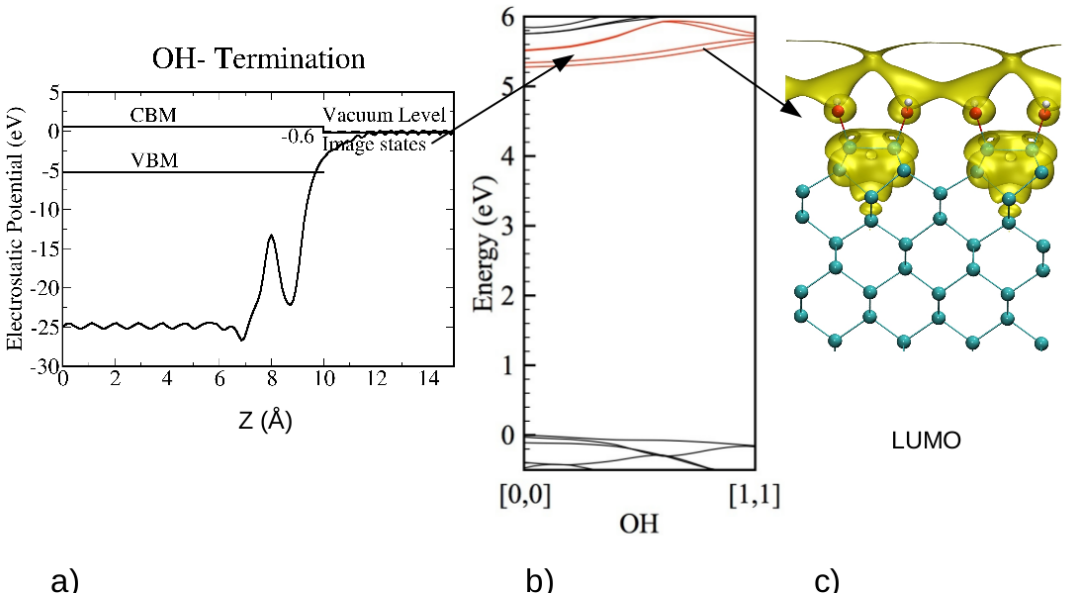

Figure 5.6: a) The calculated-electron affinity of the (001) diamond slab with HSE06 functional. The z coordinate is the direction perpendicular to the surface. $z = 0.0\mathring{A}$ corresponds to the middle of the slab. The electron-affinity is given in eV unit. b) The calculated HSE06 band structure of the (001) diamond OH-terminationed surface along (110) direction in the Brillouin zone. The results are shown for slab supercells, thus band folding appears in the band structure. Red colour represents image states. c) The corresponding charge density isosurface of the surface related states are depicted on the structures. (The NV defect is located at the middle of each structure which is not shown in the figures). Charge density isosurface is depicted at isovalue of 0.0014 e/Å^3.

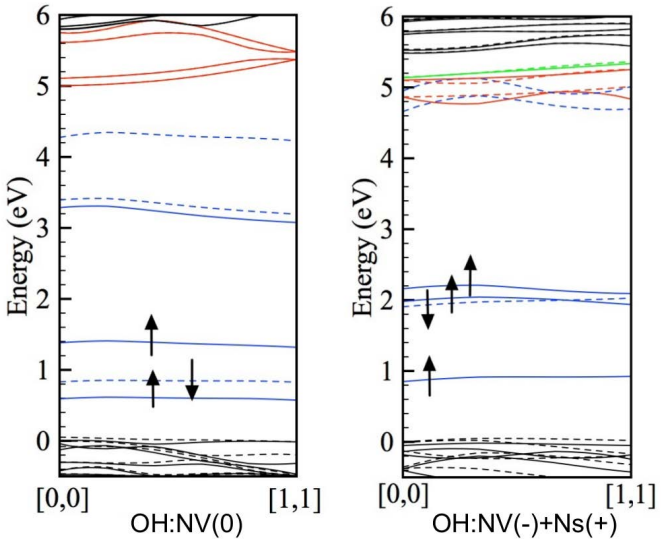

Figure 5.7: The calculated HSE06 band structure of the (001) diamond surface terminations along (110) direction in the Brillouin zone for a) NV(0) and b) NV(-)+ Ns (+). Color coding of the bands: black, blue, red and green lines correspond to bulk-like, NV, image and Ns states, respectively.

+2.40 eV, see Fig. 5.8, which is close to the value found experimentally after prolonged oxidation of the (001) diamond surface [219].

I emphasize that full termination with ether-like groups on an atomically smooth surface is not likely. Experiments show loss of periodicity and surface roughening after long-term oxidation [219]. However, the interaction between closely packed C-O-C units can be well studied in a two-dimensional periodic model with an atomically smooth surface. At such a high concentration of ether-units, surface related occupied bands appear above the valence band edge and unoccupied bands deep below the conduction band edge. The deep sub-bandgap occupied bands appear due to the interaction of the oxygen lone pairs. The steric repulsion of these states will push up the energies of these lone pair states see Fig. 5.9c. The nature of the sub-bandgap unoccupied bands can be understood by the nature of ether (C-O-C) bridges; the closely packed C-O-C units forces the surface carbon atoms toward the bulk diamond in order to arrive at the usual C-O-C angle characteristic for this ether configuration. Thus, the surface carbon atoms significantly move out from the ideal sp^3 bonding configuration, and p orbitals appear pointing perpendicular to the plane of the C-O-C unit. The interaction of these empty p orbitals form the deep unoccupied bands below the conduction band edge (see Fig. 5.9b).

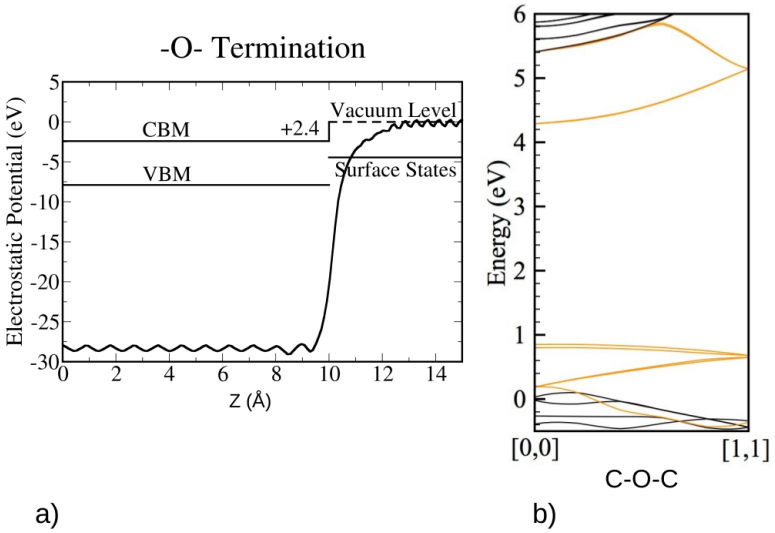

Figure 5.8: The calculated HSE06 band structure of the (001) diamond surface ether terminations along (110) direction in the Brillouin zone. The results are shown for slab supercells, thus band folding appears in the band structure. The surface related bands are colored. Orange represents localized states.

The empty defect states of NV(-) mix with these unoccupied surface states. So, even single photon absorption may lead to intermittency in the fluorescence of NV(-) in this case, because the excited electron may be trapped by the ether terminated surface. Because of the PEA, this surface is not an electron emitter, and direct photoionization may not occur. The surface bands act as shelving states, and the electron may travel back to the NV defect with some probability, giving rise to phosphorescence (see Fig. 5.13c). So, the presence of the surface bands can cause blinking when high-power laser excitation is applied in order to address single NV-centers beneath the diamond surface. In this case, two-photon absorption occurs which will again trap the high energy electron in the surface related bands. The probability of such a process is increasing with the excitation power. Indeed, such phenomena has been recently reported in relatively small oxygenated nanodiamonds [220].

5.3.4 H/O/OH termination

Based on what I have learned on the effect of full H, OH or ether terminations finally, I consider a novel arrangement with a mixed termination of the (001) diamond surface with -H and -OH

aforementioned process. The photoexcited electrons from the close-to-surface NV defects can scatter into the acceptor image state. In the case of a NEA diamond surface, this electron can leave the material with high probability (see Figure 5.13b) and can bleach NV(-). Thus, full hydroxyl termination is definitely not preferred for NV-based sensing.

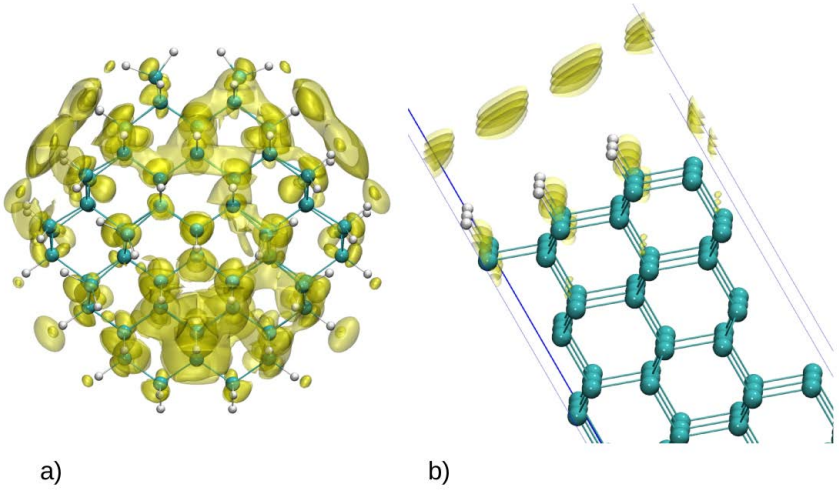

Figure 5.14: The lowest unoccupied states in small nanodiamonds of about 1.5 nm in diameter with H-terminations (charge density isovalues of 3×10^5) demonstrating that the quantum confinement does not remove the low-energy image states.

The analyse was in the slab but picture 5.14a and b propose the same things happen in the nanodiamonds. Therefore, the blinking and bleaching in nanodiamonds which could not be explained by the band bending, now can be explained by the direct interaction between surface states and defect states.

5.4 Conclusion of the luminescent study

Here we reported quantum mechanical simulations of different terminations of the (001) diamond surface, which is the dominant surface of small nanodiamonds [1] and a typical orientation to introduce NV-centers into bulk diamond. The applied method was able to reproduce the fundamental bandgap [9], as well as defect levels including charge transition levels [221] and excitation energies [9] in bulk diamond. we found that the hydrogen terminated diamond surface introduces deep, sub-bandgap states that are surface-related, delocalized image states. The

$C_{44}H_{42}$, $C_{106}H_{86}$ and $C_{208}H_{139}$, with approximately 0.6, 0.8 and 1.2 nm in diameter, respectively (see Fig. 6.1).

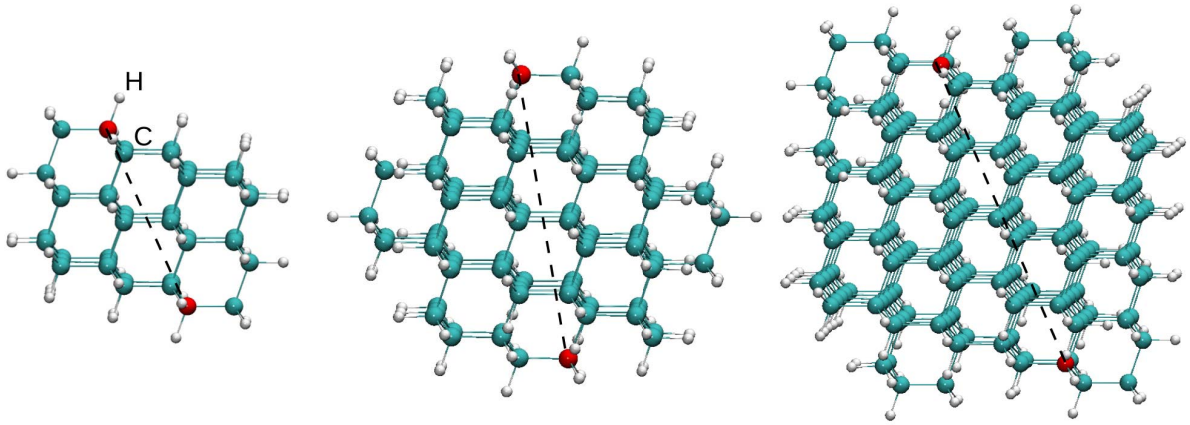

Figure 6.1: The clusters with a) 0.6 nm, b) 0.8 nm and c) 1.2 nm size. Carbon atoms are cyan and hydrogen atoms white. The size of the cluster was measured as the distance between the two farthermost carbon atoms shown in red.

Vacancy diffusion occurs through the jump of a neighboring lattice atom into the vacancy. In diamond, the saddle point of this motion is in the plane orthogonal to and halving the C-C bond, but off the bond center [232]. Therefore, clusters with increasing number of carbon shells around the bond-center site is built. The clusters were then truncated and terminated by hydrogen atoms in such a way that steric repulsion of the terminators be minimal. The perfect clusters have been fully relaxed and then a carbon atom has been removed from one side of the central bond, to create the vacancy.

In order to separate the QC effect from that of RF, two series of calculations have been performed. In the first one, the equilibrium state of the vacancy was determined by allowing all atoms to relax without constraint. The saddle point was then searched for by confining the moving carbon atom to the halving plane of the bond and minimizing the total energy. The energy difference between the saddle point and the ground state, *i.e.*, the DAE-Ea, for each cluster is shown in column 3 of table 6.1, and by large blue dots in Fig. 6.2.

In the second series, only the first neighbors of the two sites forming the central bond were allowed to relax, both in finding the equilibrium and the saddle point configuration. This way the RF is kept at the same level in all clusters and in the bulk supercell, so the change in